January 2016

Modeling of Shrinkage During Desiccation of Extruded Durum Semolina Pasta

Alex Ross Griessman
Purdue University

Graduate School Form
30 Updated 12/26/2015

PURDUE UNIVERSITY
GRADUATE SCHOOL
Thesis/Dissertation Acceptance

This is to certify that the thesis/dissertation prepared

By Alex Griessman

Entitled

Modeling of Shrinkage During Desiccation of Extruded Durum Semolina

For the degree of Master of Science

Is approved by the final examining committee:

Martin Okos
Chair

Ganesan Narsimhan

Osvaldo Campanella

To the best of my knowledge and as understood by the student in the Thesis/Dissertation Agreement, Publication Delay, and Certification Disclaimer (Graduate School Form 32), this thesis/dissertation adheres to the provisions of Purdue University's "Policy of Integrity in Research" and the use of copyright material.

Approved by Major Professor(s): Martin Okos

Approved by: Bernard Engel 1/28/2016

Head of the Departmental Graduate Program Date

MODELING OF SHRINKAGE DURING DESICCATION OF EXTRUDED DURUM SEMOLINA PASTA

A Thesis

Submitted to the Faculty

of

Purdue University

by

Alex R. Griessman

In Partial Fulfillment of the

Requirements for the Degree

of

Master of Science

May 2016

Purdue University

West Lafayette, Indiana

ACKNOWLEDGMENTS

I would like to thank Dr. Martin Okos for his support and guidance this research project. The other members of my research committee, Dr. Osvaldo Campanella and Dr. Ganesan Narsimhan, were also provided many valuable suggestions. I'm thankful for my parents' support throughout my graduate career, and for assisting in the proofreading of this document. Finally, I'd especially like to thank my fiancée, Vanessa Riggs, for her encouragement and patience.

TABLE OF CONTENTS

Page

Page

Page

Page

LIST OF TABLES

LIST OF FIGURES

SYMBOLS

α	Linear thermal expansion coefficient
β	Linear hygroscopic shrinkage coefficient
ϵ	Infinitesimal strain tensor
λ	Relaxation time
ν	Poisson ratio
ϕ	Porosity
ϕ_i	Finite element shape functions
ψ	Moisture potential
ρ	Density
ρ_A	Apparent density
σ	Cauchy stress tensor
τ	Retardation time
a_M	Moisture shift factor
a_P	Pressure shift factor
a_T	Temperature shift factor
a_w	Water activity
Bi	Biot number
c	Mass concentration
c_a	Ambient mass concentration
C_p	Heat capacity
D	Effective diffusivity
E_b	Water binding energy
$G(t)$	Viscoelastic relaxation function
$J(t)$	Viscoelastic creep compliance

K	Bulk modulus
k	Thermal conductivity
k_0	Oswin isotherm parameter []
k_1	Oswin isotherm parameter [1/°C]
k_c	Convective mass transfer coefficient
L	Slab half thickness
n_0	Oswin isotherm parameter []
n_1	Oswin isotherm parameter [1/°C]
N_w	Water flux
P_c	Capillary pressure
R	Universal gas constant
T	Temperature
t	Time
T_g	Glass transition temperature
u	Displacement vector
V_A	Apparent volume
V_m	Molar volume of water
X_{db}	Dry basis moisture content
X_w	Wet basis moisture content
X_m	Monolayer moisture content (dry basis)

ABSTRACT

Griessman, Alex R. MS, Purdue University, May 2016. Modeling of Shrinkage During Desiccation of Extruded Durum Semolina Pasta. Major Professor: Martin Okos.

Extruded durum semolina pasta was dried over saturated salt solutions, and the change in both volume and moisture content were recorded for each sample. Drying temperatures were between 40 °C to 80 °C, and relative humidities were between 0.09 and 0.96. The resulting data was analyzed using multilinear regression to determine the key parameters required to predict shrinkage during drying. It was determine that both drying temperature and change in moisture content were statistically significant predictors of volume change, with drying temperature having less impact than change in moisture content. It was found that shrinkage had a quadratic relationship with both predictors, and the final equation for predicting the change in thickness of the dried samples was: $\frac{L}{L_0} = 0.8839 + 0.004264T + (-3.726 \times 10^{-5})T^2 + 0.3704(X_i - X_f) + 0.3149(X_f - X_i)^2$. The nonlinear relationship between moisture content change and linear shrinkage is evidence of the glass transition impacting the final material dimensions.

The material properties of extruded durum semolina pasta were researched in literature, and moisture sorption isotherms, effective diffusivity, and stress relaxation curves were employed to calculate deformation during drying. Shrinkage was assumed to be caused solely by capillary pressure that occurred during drying. Mass transfer was described using the advection-diffusion equation in Lagrangian coordinates, and strain was calculated using the generalized Kelvin-Voigt model for viscoelasticity. The resulting system of partial differential equations was solved numerically using finite element method, and the results were compared to experimental data for validation. The deviation from experimental results was 10% to 20% at higher equilibrium mois-

ture contents and increased as the ambient moisture content was decreased. This error was assumed to be a result of the capillary pressure model used. If a better model were determined experimentally, it would likely improve the accuracy of the model.

1. INTRODUCTION

Dehydration of food is an important method for preserving agricultural products. Pasta, in particular, is stored primarily as a dried product in order to maintain the shape of the noodles and to retard the growth of microbes. The drying process is one of the most energy-intensive and time-consuming steps in pasta manufacturing, and optimizing has been extensively studied.

The objective of pasta drying is to produce a product with a water activity low enough to prevent microbial growth. Additionally, the product must be hard enough to retain its shape. The process should minimize porosity and cracking, while optimizing energy consumption and drying time. The final product should have a moisture content of 12%. Traditionally, pasta was dried slowly over the course of a day to a day and a half at temperatures around 50 °C; however, modern drying processes operate at much higher temperatures (around 100 °C) and have drying times as low as five hours (Field, 2009).

In order to further reduce this time, it is important to have an understanding of the mass transfer mechanisms, generated stresses, and material properties that impact the quality of the final product. Previous research focused primarily on describing the drying stresses and predicting fracture. In these studies, the amount of shrinkage was factored in using empirically-obtained coefficients which were a function of drying conditions. It is expected that the glass transition temperature of the material is a key factor in determining the porosity of the final product.

The objectives of this study are to:

- Conduct a literature review of identified drying mechanisms for pasta.
- Identify existing pasta shrinkage models.

- Obtain material properties (effective diffusivity, creep compliance, etc.) for extruded durum semolina pasta.
- Develop a model to predict drying shrinkage using capillary pressure to calculate strain.
- Measure shrinkage experimentally at a conditions both above and below the glass transition temperature.
- Validate the numerical model by comparison with the experimental data and data from literature.

2. LITERATURE REVIEW

2.1 Moisture Sorption Isotherms

Water sorption isotherms relate the water activity (or relative vapor pressure of water) to the moisture content of the solid. Because the water adsorbs onto the surface of a food product and binds to it, the equilibrium moisture content of the food varies as a function of the ambient relative humidity as well as temperature. Several isotherm models exist to relate the water activity to the sample's moisture content, depending on the isotherm type. For pasta, water binding is best described by a Type II, or sigmoidal isotherm. This can be modeled using the GAB model, the Oswin model, or the Henderson model.

2.1.1 Bound Water Properties

Bound water, or vicinal water, is the water that has adsorbed onto the surface of the porous media. This water is unavailable for most chemical reactions and is effectively treated as a separate phase for modeling purposes (Takhar et al., 2003b). At low water activities, microbial growth ceases. The exact range of water activities that each bacteria/fungus can survive in varies, but below a water activity of 0.6, nearly no microbes can grow.

Due to the change in molecular structure, the material properties of vicinal water differ significantly from the properties of water in the bulk phase. For vicinal water in silica gel, density is about 3% lower than bulk water density. Etzler and Fagundus (1987) found that the density of water in the vicinal phase was related to the pore size of the surrounding solid matrix by the empirical relation $\rho = A\left(\frac{1}{h^{1/2}}\right) + B$, where h is pore radius, and A and B are temperature-dependent constants.

Additionally, the change in heat capacity as water binds during adsorption can be as large as a 25% increase relative to the bulk phase. The heat capacity of vicinal water is highest near the surface and decays exponentially to the bulk value as the distance from the solid matrix increases. As with the density, the range over which the elevated heat capacity is observed is limited to 5 nm to 6 nm from the adsorbing surface (Etzler and White, 1987).

2.1.2 Langmuir Isotherm

Langmuir isotherms (Type I) assume that the substrate has a fixed amount of binding sites and that the fluid or gas binds in a single layer (Liu, 2006). Type II and III isotherms more closely model the water adsorption/desorption behavior of food products. Type III isotherms are typically used to describe the sorption behavior of foods with soluble components, such as sugar, while Type II isotherms are used for foods without soluble sugars. Type IV and V isotherm models describe sorption of porous materials with a limited adsorption capacity. For these materials, the maximum adsorption happens below the vapor pressure of the gas (Al-Muhtaseb et al., 2002).

2.1.3 BET Isotherm

The BET isotherm is a semi-empirical model that relates water activity to moisture content using two temperature-dependent parameters. This equation can be derived by extending the Langmuir isotherm model to multilayer adsorption.

$$\frac{X_{db}}{X_m} = \frac{Ca_w}{(1-a_w)(1-a_w+Ca_w)} \tag{2.1}$$

Here, the X_m constant represents the moisture content of the material when a single layer of molecules has adsorbed onto the surface at the desired temperature, and the

C constant is related to the heat of adsorption of the first layer, and the heat of liquefaction. The equation to determine this constant is as follows:

$$C = \frac{a_1 g}{b_1} \mathrm{e}^{\frac{E_1 - E_L}{RT}}$$

where a_1, b_1, and g are constants, E_1 is the heat of adsorption associated with the first layer, and E_L is the heat of liquefaction, which is equal to the heat of adsorption for the second and subsequent layers. This equation can be simplified to the following form:

$$C = C_0 \mathrm{e}^{\frac{\Delta H_C}{RT}}$$

The monolayer moisture content, X_m has a similar form:

$$X_m = X_{m,0} \mathrm{e}^{\frac{\Delta H_m}{RT}}$$

This model fits experimental data best when the water activity is low, less than 0.45 to 0.5 (Heldman et al., 2006).

2.1.4 GAB Isotherm

The GAB model is an extension of the BET model that adds a correction factor (Andrieu et al., 1985), K, to accurately model water activities up to 0.94 (Heldman et al., 2006).

$$\frac{X_{db}}{X_m} = \frac{C_g K a_w}{(1 - K a_w)(1 - K a_w + C_g K a_w)} \tag{2.2a}$$

$$X_m = X_{m,0} \mathrm{e}^{\frac{\Delta H_m}{RT}} \tag{2.2b}$$

$$C_g = C_{g,0} \mathrm{e}^{\frac{\Delta H_c}{RT}} \tag{2.2c}$$

$$K = K_0 \mathrm{e}^{\frac{\Delta H_k}{RT}} \tag{2.2d}$$

When $K = 1$, the GAB model is equivalent to the BET equation. As with C_g and X_m, K is temperature-dependent, and this dependence can be described by an Arrhenius relationship. The six constants required to describe the temperature dependence of

the isotherm can be calculated by fitting the GAB equation to experimental data at multiple temperatures and then performing regression on each of the constants.

In order to calculate water activity from the equilibrium moisture content using the GAB equation, the equation first must be converted into a quadratic form as demonstrated in Samaniego-Esguerra et al. (1991). The equations they derived are shown in Eq. 2.3.

$$\frac{a_w}{X} = \alpha a_w^2 + \beta a_w + \gamma \tag{2.3a}$$

$$\alpha = \frac{K}{X_m}\left(\frac{1}{C_g} - 1\right) \tag{2.3b}$$

$$\beta = \frac{1}{X_m}\left(1 - \frac{2}{C_g}\right) \tag{2.3c}$$

$$\gamma = \frac{1}{X_m C_g K} \tag{2.3d}$$

Once the isotherm model is expressed in this form, solving for water activity is trival using the quadratic formula. This was done in Eq. 2.4.

$$a_w = \frac{\pm C_g K \sqrt{\frac{C_g X^2 - 2C_g X X_m + C_g X_m^2 + 4XX_m}{C_g K^2}} + C_g X - C_g X_m - 2X}{2(G-1)KX} \tag{2.4}$$

2.1.5 Oswin Isotherm

The Oswin equation is an empirical isotherm model that relates moisture content to water activity at different temperatures using a set of four constants. The equation is:

$$X_{db} = (k_0 + k_1 T)\left(\frac{a_w}{1 - a_w}\right)^{(n_0 + n_1 T)} \tag{2.5}$$

where X_{db} is the dry basis moisture content and T is the temperature in degrees Celsius. The Oswin model does not provide any mechanistic insight into the structure of the bound water, which the GAB equation does through the monolayer moisture content parameter; however, it can provide a better fit for some materials (Bressani, 2014; Xiong et al., 1992).

In order to calculate water activity, given the moisture content, Eq. 2.6 can be used. This was derived from Eq. 2.5 by solving for water activity.

$$a_w = \frac{\left(\frac{X}{k_0+k_1T}\right)^{\frac{1}{n_0+n_1T}}}{\left(\frac{X}{k_0+k_1T}\right)^{\frac{1}{n_0+n_1T}}+1} \tag{2.6}$$

2.1.6 Henderson Isotherm

The Henderson isotherm uses four parameters to predict water activity and is purely empirical (Litchfield and Okos, 1992).

$$a_w = 1 - \exp\left(-A(T-B)^C\right) X^D \tag{2.7}$$

2.1.7 Durum Semolina Isotherm Data

For extruded durum semolina, the sorption isotherm is well-described by either the Oswin or GAB isotherm models. The model of choice depends on the temperature being examined. Bressani compared the Oswin and GAB isotherms at temperatures ranging from 25 °C to 90 °C, and her results are presented in Table 2.1 (Bressani, 2014). Parameters for the Oswin model can be found in Table 2.4, GAB parameters in Table 2.3, and Henderson parameters in Table 2.2.

Table 2.1.
Preferred isotherm model (Bressani, 2014).

Temperature °C	Model
25	GAB
30	Oswin
35	Oswin
40	Oswin
50	Oswin
60	Oswin
70	GAB
75	GAB
80	Oswin
85	Oswin
90	Oswin

Table 2.2.
Henderson isotherm parameters for durum semolina (Litchfield and Okos, 1992).

Constant	Value
A	1.3638×10^{-11}
B	2.5728×10^{2}
C	4.1686
D	2.9060

Table 2.3.
Summary of GAB isotherm parameters for extruded durum semolina.

Source	$X_{m,0}$	ΔH_m	$C_{g,0}$	ΔH_c	K_0	ΔH_k
Bressani (2014)	3.80×10^{-4}	1.61×10^{3}	4.19×10^{-4}	3.51×10^{3}	1.00	-65.3
Erbas et al. (2005)	1.38×10^{-5}	2.64×10^{3}	1.27×10^{12}	-7.86×10^{3}	2.51	-349
Andrieu et al. (1985)	1.7×10^{-3}	1.13×10^{3}	2.83×10^{-8}	6.54×10^{3}	1.83	-238
Waananen (1989)	4.40×10^{-3}	841	2.86×10^{-9}	7.38×10^{3}	0.1313	605

Table 2.4.
Summary of Oswin isotherm parameters for extruded durum semolina.

Source	k_0	k_1	n_0	n_1	Range	Temp Range
Andrieu et al. (1985)	0.154	-1.22×10^{-3}	0.078	-7.32×10^{-3}	$0.1 < a_w < 0.9$	40 °C to 90 °C
Xiong (1989) (refitted)	0.171	-1.61×10^{-3}	0.0882	8.49×10^{-3}	-	
Xiong et al. (1992)	0.176	-1.748×10^{-3}	0.182	6.946×10^{-3}	$0.14 < a_w < 0.85$	35 °C to 50 °C
Bressani (2014)	0.1571	-1.2×10^{-3}	0.2076	4.3×10^{-3}	-	

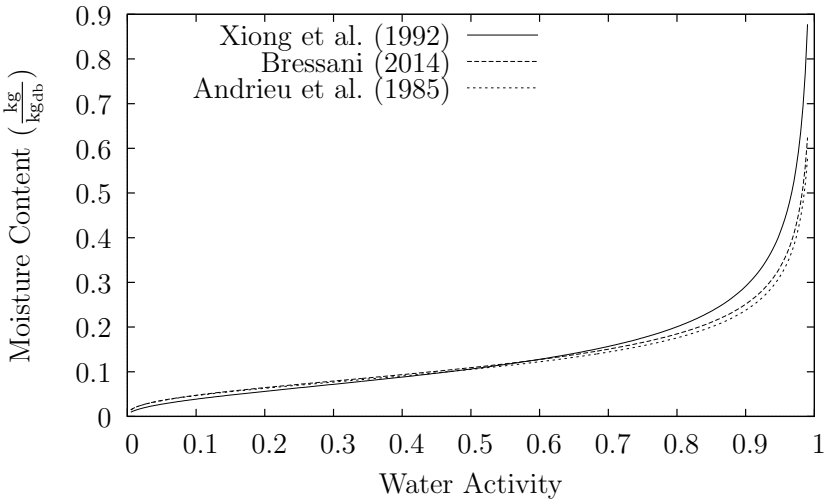

Fig. 2.1. Comparison of Oswin isotherm models at 40 °C. The parameters used are from Table 2.4.

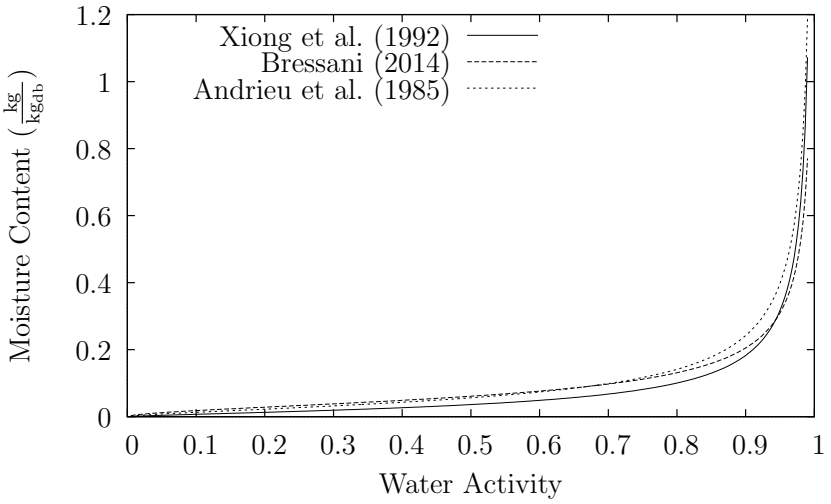

Fig. 2.2. Comparison of Oswin isotherm models at 80 °C. The parameters used are from Table 2.4.

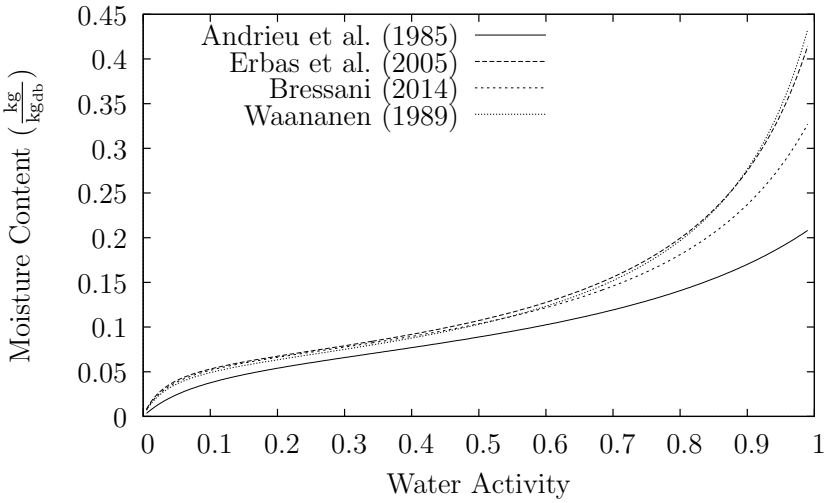

Fig. 2.3. Comparison of GAB isotherm models at 40 °C. The parameters used are from Table 2.3.

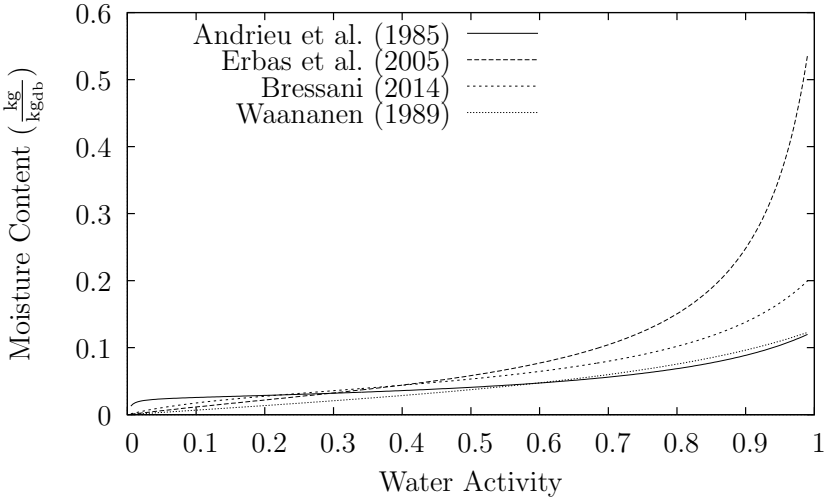

Fig. 2.4. Comparison of GAB isotherm models at 80 °C. The parameters used are from Table 2.3.

2.2 Shrinkage Models

2.2.1 Empirical Models

Multiple models exist to describe the deformation of drying materials empirically. Linear models are adequate for cases where the porosity of the solid being dried does not change with time (Mayor and Sereno, 2004). For cases where porosity increases towards the end of the drying process, an exponential model is more appropriate (Mulet et al., 1997).

Some of the simpler shrinkage models assume that as the product dries, the solid matrix collapses completely, and the resulting final porosity is effectively zero. This approach works from the assumption that the remaining pores in the material will be still filled with water at the end of the drying period. This approach is valid for the case of low drying temperatures and a small decrease in moisture content (Katekawa and Silva, 2006). For cases where the porosity of the material does change during the drying process, several semi-empirical models exist, such as the one presented in Rahman et al. (1996). Rahman's model relates moisture content to shrinkage at constant porosity using Eq. 2.8.

$$\xi = \frac{V_A}{V_{A0}} = \frac{\rho_{A0}}{\rho_A}\left[\frac{1 - X_{w0}}{1 - X_w}\right] \tag{2.8}$$

One method for estimating the shrinkage coefficient of drying pasta is to assume that pores collapse completely as the moisture leaves so that the volume fraction of air is effectively zero. Using this approximation, the shrinkage coefficient is equal to the ratio of the density of the dry solid (at zero porosity) to water density (Temmerman et al., 2007).

In order to quantify the relationship between moisture loss and shrinkage, Cummings (1981) used a hygroscopic expansion coefficient (analogous to the thermal expansion coefficient).

$$\frac{\Delta L}{L} = \beta \Delta M + \alpha \Delta T \tag{2.9}$$

He found that the value of β to be equal to $0.34\frac{1}{M(db)}$ and α to be equal to $-0.033 \times 10^{-3}\frac{1}{^{\circ}\mathrm{C}}$. Only the moisture effect was considered statistically significant (Cummings, 1981).

Cummings et al. (1993) determined the value of β to be $0.30\frac{1}{M(db)}$ for extruded pasta. For comparison the value of the thermal expansion coefficient for the same material to be $1.3 \times 10^{-3}\frac{1}{^{\circ}\mathrm{C}}$, which was small enough to be neglected. Other papers have used a similar method to characterize shrinkage. Both Andrieu et al. (1989) and Migliori et al. (2005) used a value of 0.42 for the hygroscopic expansion coefficient.

Kowalski and Mielniczuk (2006) measured the shrinkage of macaroni dough and calculated stress during drying. They considered the material both as an elastic and as a viscoelastic solid, with the same shrinkage coefficient for each model. The elastic model for stress is:

$$\sigma_{xx} = \sigma_{yy} = 3K\kappa\frac{2M}{2M+A}\left(\frac{1}{2H}\int_{-H}^{H}\theta dz + \frac{3}{2H^3}z\int_{-H}^{H}\theta z dz - \theta\right) \tag{2.10a}$$

$$3K = 2M + 3A \tag{2.10b}$$

where M and A are Lamé's parameters, κ is the shrinkage coefficient, H is the half-thickness of the slab, and θ is the moisture content. For the viscoelastic model, the equation for stress is:

$$\sigma_{ij}^{(v)}(r,t) = \sigma_{ij}^{(e)}(r,t) - \frac{1}{t_R}\int_0^t \exp\left(\frac{\xi - t}{t_R}\right)\sigma_{ij}^{(e)}(r,\xi)d\xi \tag{2.11}$$

where t_R is the relaxation time. The value for κ for both models was determined to be 0.28.

Mercier et al. (2011) developed a semi-empirical model that relates the volume of water that diffuses out of the slab with the volume of air that diffuses in. The fraction of water replaced by air is considered to be constant throughout the drying process. The volumetric strain for the pasta at any moisture content can be calculated using Eq. 2.12, and the porosity of the sample can be determined from Eq. 2.14.

$$\chi_T(t) = \frac{V_F - V_0}{V_0} = \frac{(1-\eta)(X_0 - X)}{\rho_w/\rho_{app0}(1+X_0} \tag{2.12}$$

$$\rho_{app} = \frac{\rho_{app0}(1+X)}{(1+X_0)(1-\chi_T)} \tag{2.13}$$

$$\epsilon_s = 1 - \frac{\rho_{app}}{1+X}\frac{1}{\rho_s} \tag{2.14}$$

The fraction of air replaced, η, assumes a value of 0.28 at 40°C and 0.15 at 80°C for extruded durum semolina (Mercier et al., 2011). The pasta was dried at a relative humidity of 65% and the air velocity over the surface was kept to between one and two meters per second. Samples were dried for twenty hours. This model can be converted to a shrinkage coefficient of the same form as Eq. 2.9, where the value for β is given by (Mercier et al., 2013):

$$\beta = \frac{1-\eta}{\rho_w/\rho_{app,0}(1+M_0)} \tag{2.15}$$

For any model using a volumetric shrinkage coefficient, changes in dimension can be related to the moisture content by

$$\partial x = (1+\epsilon X)\partial\xi \tag{2.16}$$

For both of these, x is the Eulerian coordinate, ξ is the Lagrangian coordinate, and ϵ is the shrinkage coefficient. Because the change in dimension affects diffusion, when written in Lagrangian coordinates, the diffusion equation must be modified to account for this (Temmerman et al., 2008).

$$\frac{\partial X}{\partial t} = \frac{\partial}{\partial \xi}\left(\left(\frac{D}{1+\epsilon X}\xi\right)\frac{\partial X}{\partial \xi}\right) \tag{2.17}$$

2.2.2 Poroelasticity

In order to describe the mechanical behavior of a porous material containing water that is undergoing some sort of deformation, Biot's theory of poroelasticity is frequently employed (Biot, 1941). This theory was developed to model soil mechanics and deformation as pressure was applied or as water was added to the soil. For this model, fluid flows through the porous media according to Darcy's Law, and the deformations of the solid matrix are assumed to be small enough as to be linear

and elastic. The constitutive equations for the basic theory can be expressed as follows (Schanz and Cheng, 2001):

$$\sigma_{ij} = 2G\epsilon_{ij} + \left(K - \frac{2}{3}G\right)\epsilon_{kk}\delta_{ij} - \alpha\delta_{ij}p$$

$$\zeta = \alpha\epsilon_{kk} + \frac{\phi^2}{R}p$$

Here, σ, ϵ, and ζ represent the stress, strain, and variation in fluid content, respectively. The elastic moduli are G, and K, and p is the pore pressure exerted by the fluid. The remaining variables are material parameters that can be found experimentally (Detournay and Cheng, 1993).

This model has been widely applied in soil science to describe the coupling between fluid flow and soil deformation (Schanz and Cheng, 2000). Additionally it has been applied in food science to model the flow of liquid through a partially frozen porous media (Carcione et al., 2007).

2.2.3 Correspondence Principle

Poroelastictiy has been expanded to model porous viscoelastic solids with large deformations (Biot, 1973), as well as for small deformations of viscoelastic materials (Schanz and Cheng, 2001). The primary method by which this theory is adapted to the viscoelastic case is through the correspondence principle (Christensen, 2003), which allows the replacement of elastic moduli and material parameters with their corresponding Laplace-transformed viscoelastic counterparts. The equation can then be solved and inverse transformed to obtain the deformation of the solid as a function of time. This approach works well when the viscoelastic parameters do not depend on material properties that vary with time, such as temperature or moisture content, since these dependencies cause the equations to not transform to be the same form as their elastic equivalents (Christensen, 2003). Two special cases exist, however, where temperature dependent properties can be considered. The first is where the temper-

ature is uniform, but varies with time, and the second is where the temperature is non-uniform, but constant (steady-state) (Morland and Lee, 1960; Schapery, 1967).

Schanz and Cheng modeled the change in pressure of a viscoelastic column of soil filled with water as a result of a step-change in applied pressure at one of the boundary conditions. He used Biot's poroelasticity model (Biot, 1941) and the correspondence principle to describe the viscoelastic behavior of the porous material, and calculate the velocity of waves propagating through the material. The equations solved for stress and strain were:

$$\hat{\sigma}_{ij} = 2\hat{G}\hat{\epsilon}_{ij} + \left(\hat{K} - \frac{2}{3}\hat{G}\right)\hat{\epsilon}_{kk}\delta_{ij} - \hat{\alpha}\delta_{ij}\hat{p}$$

$$\hat{\zeta} = \hat{\alpha}\hat{\epsilon}_{kk} + \frac{\phi^2}{\hat{R}}\hat{p}$$

$$\hat{\alpha} = 1 - \frac{\hat{K}}{\hat{K}_s}$$

$$\hat{R} = \frac{\phi^2 K_f \hat{K}_s^2}{K_f(\hat{K}_s - \hat{K}) + \phi\hat{K}_s(\hat{K}_s - K_f)}$$

where variables denoted with a $(\hat{\cdot})$ are functions of s and in the Laplace domain. The solid material was modeled as a Kelvin-Voigt material, but the approach work for other rheologica models, such as the Maxwell or Burgers model. The fluid was considered to be Newtonian, and flow was calculated using Darcy's Law

$$\hat{q}_i = -\kappa\left(\hat{p}_{,i} + s^2\rho_f\hat{u}_i + \frac{\rho_a + \phi\rho_f}{\phi}s^2\hat{v}_i\right)$$

These equations were combined with the solutions for the elastic case of this problem from a previous paper (Schanz and Cheng, 2000) and the resulting equations were inverse transformed numerically to arrive at a solution in the time domain.

Another model for flow and deformation of a porous media was derived for shrinking concrete pastes by Leung (2009). This model used Fick's Law to account for moisture transport and utilized a modified version of the poroelasticity model (Bentz et al., 1998), which was adapted for viscoelastic materials to calculate shrinkage.

The driving force for shrinkage was the pore pressure exerted by the fluid inside the concrete paste, and this was calculated using the Kelvin-Laplace equation

$$p = -\frac{\ln(RH/100)RT}{V_m}$$

where p is the pore pressure, RH is the relative humidity, R is the ideal gas constant, T is absolute temperature, and V_m is the molar volume of water. The amount of shrinkage was calculated from

$$\epsilon = \int_0^t \frac{S\partial p}{3\partial t}\left(B(t-t') - \frac{1}{K_{solid}}\right)dt'$$

where ϵ is the strain, p is the pore stress, S is the saturation factor, B is the viscoelastic bulk compliance, and K_{solid} is the bulk modulus of the solid itself. In order to solve this equation for the amount of strain resulting from moisture loss, it was transformed into the Laplace domain, and several approximations were applied to simplify the problem.

2.2.4 Thermodynamic Shrinkage

Eichler et al. (1997) determined that there were three main forces for the driving force for shrinkage in a polymer gel. They are:

1. Relaxation of network pressure
2. Change in solvent quality during drying
3. Capillary forces

Willis (2001) analyzed the shrinkage of pasta in terms of the mixing properties between the polymer network and the water present in the dough. She examined the free energy change associated with mixing the adding water to the polymer matrix in the pasta. She then calculated the entropy change associated with the polymer matrix in the dough undergoing a change from the unstressed, unswollen state to the deformed, swollen state (presented in Eq. 2.18).

$$\Delta S_{d,s} = -kn\ln\left(\frac{n}{n+Zv}\right) - kv\beta^2\lambda^2\left[\frac{1}{3}\left(\frac{n+Zv}{Zv}\right)\left(\alpha^2+\frac{2}{\alpha}\right)-1\right] \qquad (2.18)$$

Here, n represents the number of solvent molecules, Z is the number of polymer units per chain, and α is the ratio of the swollen length to the dry length.

$$f' = \left(\frac{RT\rho A_0'}{M_c}\right)\left(\alpha - \frac{1}{\alpha^2}\right) \tag{2.19}$$

Willis used Eq. 2.18 to obtain the retractive force, shown in Eq. 2.19, that arises during solvent removal. Here, A_0' is the cross sectional area of the swollen polymer in it's undeformed configuration, an M_c is the average molecular weight of the polymer chain. The shrinkage modeled by this force is limited by the presence of starch granules within the polymer network, and by the glass transition temperature of the material. Once either of these limit the collapse of the solid matrix, the drying becomes unsaturated, and the air phase must be taken into account.

2.2.5 Capillary Pressure

According to Mayor and Sereno (2004), the primary driving force for shrinkage due to dessication is the pressure difference between the wetting phase and the non-wetting phase created by surface tension in the pores of the solid matrix (Mayor and Sereno, 2004).

$$P_c = P_{non-wettingphase} - P_{wettingphase}$$

This capillary pressure (or pore pressure) is directly related to surface tension at the liquid-vapor interface and the radius of curvature of the meniscus. The Young-Laplace equation describes this relationship in a capillary tube as follows:

$$\Delta P = \frac{2\gamma\cos\theta}{r} \tag{2.20}$$

where ΔP is the pressure difference across the interface, γ is the surface tension, θ is the contact angle, and r is the mean radius of curvature of the surface (Miranda and Silva, 2005).

When the surface of a liquid-vapor interface is curved due to a meniscus, the equilibrium vapor pressure of the liquid is reduced. The degree of reduction is primarily a

function of the radius of curvature of the surface. The relationship is described using the Kelvin equation:

$$\ln \frac{P}{P_0} = -\frac{2\gamma \overline{V} \cos\theta}{rRT} \tag{2.21}$$

where $\frac{P}{P_0}$ is the reduced vapor pressure over normal vapor pressure, $\overline{V}$ is the molar volume of the liquid, R is the gas constant, and T is temperature (Miranda and Silva, 2005). This equation is based on macroscopic thermodynamics, and can become less accurate as the mean radius of curvature decreases, and this deviation can be even larger when examining capillaries. Fisher and Israelachvili (1981b) examined the accuracy of the Kelvin equation when describing vapor pressure change during capillary condensation of cyclohexane on mica cylinders. They found that when the mean radius of curvature was above 4 nm, the experimental deviation from the predicted results was less than 6%; however, they also noted that the presence of soluble contaminates significantly affected the accuracy of the Kelvin equation. For water, the radius of curvature must be slightly larger 5 nm for the Eq. 2.21 to apply (Fisher and Israelachvili, 1981a). Christenson later examined the force required to separate two mica surfaces and found that the Kelvin equation was accurate for relative vapor pressures in the range of 0.7 to 1 for both hexane and water, corresponding to a radius of curvature of approximately 1.5 nm (Christenson, 1988). Additionally, in porous media, the degree of saturation must be such that bulk liquid water is present in the pores for capillary pressure to have an effect. This means that the saturation must be above the upper limit of the hygroscopic region (Gawin et al., 2002). For relative vapor pressures below 0.7, but above the upper limit of saturation, the capillary pressure should be measured experimentally.

2.2.6 Disjoining Pressure

Disjoining pressure is a attractive interaction caused by Van der Waals, electrostatic, and other forces acting between pore walls. The disjoining pressure can be defined as:

$$\Pi_D = -\frac{1}{A}\left(\frac{\partial G}{\partial x}\right)_{T,V,A}$$

where A is the area over which the forces are acting, G is the Gibbs free energy of the two surfaces, x is the distance between the surfaces, and Π_D is the disjoining pressure. This is a significant contribution to shrinkage only at relatively high moisture contents, where the relative humidity is greater than 50% (Han and Lytton, 1995). For porous media, the volume change due to disjoining pressure can be expressed using the following equation:

$$\left[\frac{\Delta V}{V}\right]_d = \beta f(W_a)\frac{RT}{MV_m}\ln h \tag{2.22}$$

where β is the coefficient of compressibility, W_a is the amount of adsorbed water, V_w is the volume of water, and $f(W_a)$ is the area ratio over which the pressure is active (Han and Lytton, 1995).

2.2.7 Moisture Potential

By combining Eq. 2.20 and Eq. 2.21, an equation for capillary pressure found in terms of water activity.

$$P_c = \psi\rho_w = \frac{RT}{V_m}\ln a_w \tag{2.23}$$

Here, ψ is equal to the moisture potential, which is equal to capillary pressure at high levels of saturation. At lower moisture contents, where capillary pressure is not defined, Eq. 2.23 is still valid because water activity is affected by other factors. Because of this, moisture potential is capable of describing the shrinkage forces at all moisture contents due to factors such as capillary pressure, disjoining pressure, and osmotic forces (Brinker and Scherer, 1990). The value of ψ has units of Joules per gram, and is the partial specific Gibbs free energy of the liquid.

2.2.8 Effective Stress

In order to determine the amount of strain exhibited by the pasta slab as it loses moisture, the stress on the solid matrix must first be calculated. This is a composite of externally applied forces and the change in internal stress generated by the changing moisture content. Effective stress can be calculated using this equation: (Garg and Nur, 1973)

$$\langle \sigma_{ij} \rangle = \sigma_{ij} - \zeta P_c \delta_{ij} \tag{2.24}$$

where σ_{ij} is the externally applied force, P_c is the capillary moisture potential, and δ_{ij} is the Kronecker delta.

In Equation 2.24, ζ represents the boundary porosity or Bishop's parameter (Narasimhan and Witherspoon, 1977). This parameter can take several values depending on the model used for effective stress. Terzaghi let ζ be equal to the porosity so that when the material has no void space, the effective stress on the material is equal to the externally applied stress (Terzaghi, 1923). Other models include:

$$\zeta = 1 - \frac{K}{K_s} \tag{2.25}$$

$$\zeta = 1 - n\frac{K}{K_s} \tag{2.26}$$

where K is the bulk modulus of the porous medium, K_s is the bulk modulus of the solid matrix at zero porosity, and n is the solid fraction (Garg and Nur, 1973). Additionally, Narasimhan and Witherspoon report that ζ is a nonlinear function of saturation that must be determined experimentally when the porous medium is only partially saturated (Narasimhan and Witherspoon, 1977).

2.3 Freeze Drying

Freeze drying was also investigated as a method for drying pasta entirely below the glass transition temperature. This is in contrast to convective drying where the sample changes from a rubbery to a glassy state part of the way through the drying process.

Freeze drying consists of two separate stages. First, the product is frozen, and then the ice is sublimated off. This process is normally carried out below the glass transition temperature to minimize shrinkage. Below the glass transition temperature of the material, there is little to no observed shrinkage (Krokida et al., 1998; Lewicki and Pawlak, 2003). For conditions above the glass transition temperature, the final porosity of the product can be directly related to the complex viscosity of the solid matrix (Krokida et al., 1998).

2.4 Material Composition

Cummings et al. (1993) identified the composition of the extruded durum semolina pasta. This composition can be used to calculate the material properties of the pasta as a function of temperature and moisture content using the Choi-Okos equations (Choi and Okos, 1986).

The porosity of the pasta samples varies based on the moisture content and processing parameters. For regular pasta, the porosity is around 6.12% (Xiong et al., 1992). Mercier et al. found that temperature had a strong effect on porosity. For samples dried at 40°C, the observed porosity was 6%, and for samples dried at 80°C, the porosity was 11% (Mercier et al., 2011).

Table 2.5.
Composition of durum semolina pasta. Wet composition from Cummings et al. (1993).

Component	Wet Composition	Dry Composition
Fat	2.0%	2.39%
Protein	13.9%	16.6%
Ash	0.69%	0.824%
Fiber	1.5%	1.79%
Water	16.3%	0.0%
Carbohydrate	65.5%	78.4%

2.5 Viscoelasticity

Materials that exhibit a time-dependent response to stress or strain are considered viscoelastic, and they exhibit two phenomena not common to either viscous fluids or to elastic solids. The first is stress relaxation, where the stress resulting from a fixed strain decreases with time. The second is creep, where the strain experienced by the material increases due to an imposed stress.

When calculating the stress or strain on a sample, a common assumption to make when the degree of deformation is small is that the strain tensor is approximately linear. This is referred to as infinitesimal strain theory. In this case, the Lagrangian and Eulerian strain tensors are approximately equal, and the strain tensor is defined by:

$$\underline{\underline{\epsilon}} = \frac{1}{2}\left((\nabla \underline{u})^T + \nabla \underline{u}\right) \tag{2.27}$$

2.5.1 Maxwell Model

For a viscoelastic solid undergoing stress relaxation where the maximum deformation is small enough to be considered infinitesimal, the generalized Maxwell model (Eqs. 2.28 and 2.29) is effective in describing the stress response as a function of time due to the imposed strain. This model consists of a single elastic element (a spring) in parallel with a number of Maxwell elements (a spring in series with a dashpot).

$$\sigma(t) = \int_{\tau_0}^{t} E(t-\tau)\dot{\epsilon}(\tau)\,\mathrm{d}\tau \tag{2.28}$$

$$E(t) = E_a + \sum_{i=0}^{N} E_i \exp(-t/\lambda_i) \tag{2.29}$$

This model can also be written as a set of differential equations. For the infinitesimal strain regime, the generalized Maxwell model can be written as:

$$\sigma = E_a\epsilon + \sum_{i=0}^{N} E_i q^{(i)} \tag{2.30a}$$

$$\frac{\partial}{\partial t}\epsilon = \frac{\partial}{\partial t}q^{(i)} + \frac{1}{\lambda_i}q^{(i)} \tag{2.30b}$$

2.5.2 Kelvin-Voigt Model

A Kelvin-Voigt element is a spring and a dashpot in parallel. As with the Maxwell element, several of these can be combined in order to describe complex viscoelastic behaviour. The generalized Kelvin model combines several Kelvin-Voigt elements in series in order to describe creep compliance. The creep compliance function is written similarly to the stress relaxation function for the Maxwell model (Steffe, 1996).

$$J(t) = J_a + \sum_{i=0}^{N} J_i \left(1 - \exp\left(\frac{-t}{\lambda_i}\right)\right) \tag{2.31}$$

$$\epsilon(t) = \int_0^t J(t-\tau)\frac{d\sigma}{d\tau}d\tau + \epsilon_0(t) \tag{2.32}$$

This equation can also be written as a set of differential equations of the form:

$$\epsilon = J_a\epsilon + \sum_{i=0}^{N} J_i r^{(i)} \tag{2.33a}$$

$$\sigma = \frac{\partial}{\partial t}r^{(i)} + \frac{1}{\tau_i}r^{(i)} \tag{2.33b}$$

The $r^{(i)}$ variables represent the partial stresses experienced by the individual Kelvin elements, and τ_i is the retardation time of the i^{th} element.

2.5.3 Burger's Model

Burgers Model (Steffe, 1996) Creep Function

$$J = J_0 + \sum_i J_i \left(1 - e^{-\frac{t}{\lambda_{ret,i}}}\right) + \frac{t}{\mu_0} \tag{2.34}$$

2.5.4 Temperature and Moisture Effects

The stiffness of viscoelastic materials is strongly dependent on the material's temperature and moisture content, and even a small change in one of these parameters can drastically affect the material's response to stress. Several methods exist to characterize this change in viscoelasticity, depending on the temperature and moisture content range being observed.

For thermorheologically simple materials, the effect of changing temperature can be characterized by temperature shift factor ($a_T(T)$) which is used to superimpose the viscoelastic moduli at different temperatures. This is done by replacing the time with a reduced time such that Eq. 2.28 becomes

$$\sigma(\xi) = \int_{\xi_0}^{\xi} E(\xi - \xi')\dot{\epsilon}(\xi')\,\mathrm{d}\xi' \tag{2.35}$$

and $\xi \equiv ta_T(T)$. For temperatures above the glass transition temperature, the temperature shift factor can be characterized using the WLF model (Eq. 2.61) (Williams et al., 1955). Another equation for temperature shift which was used by Cummings et al. (1993) is:

$$\ln a_T = C_1(T - T_0) \tag{2.36}$$

The effects of moisture can also be described by a shift factor for hygro-rheologically simple materials. Cummings used an equation of the same form as Eq. 2.36 to describe the moisture effects on the viscoelasticity parameters (Cummings et al., 1993).

$$\ln a_M = C_1(M - M_0) \tag{2.37}$$

Viscoelastic material parameters can also be a function of applied pressure. As with temperature and moisture content, this effect can be characterized by a pressure-dependent shift factor. The O'Reilly model accounts for this using an exponential relation of the same form as Eq. 2.36 (Emri, 2005).

$$\ln a_P = C_1(P - P_0) \tag{2.38}$$

An alternate method to time-temperature superposition to accounting for the change in viscoelastic parameters with temperature is to write an empirical equation for each parameter individually. The Fermi equation describes change in mechanical parameters with respect to changing values for temperature, water activity or moisture content near the glass transition temperature (Peleg, 1994).

$$Y(T) = \frac{Y_s}{1 + exp\left\{\frac{T - T_c}{a}\right\}} \tag{2.39}$$

Here, $Y(T)$ is any viscoelastic material parameter, Y_s is the value of that parameter below the glass transition temperature, and both T_c and a are constants. This same equation can be applied to moisture effects as well, and the equations for temperature and moisture effects can be combined as in Rozzi (2002).

2.5.5 Poisson Ratio

The Poisson ratio is used to quantify the amount of strain in a material that arises from a transverse strain, and it ranges from -1 to 0.5, with 0.5 representing a material that is completely incompressible. This quantity is useful in converting from one elastic modulus to another. Poisson ratio can be a function of temperature, moisture content, and, for viscoelastic materials, a function of time. It is usually difficult to measure the change in Poisson ratio with time in viscoelastic materials, so instead it is usually assumed that either the Poisson ratio or bulk modulus remain constant (Williams, 1980). In general, for polymers below their glass transition, the Poisson ratio is between 0.35 and 0.40 (Williams, 1980).

For pasta, specifically, several values for Poisson ratio are cited in literature. Cummings et al. used a value of 0.35 for moisture contents above 0.175 $\frac{\text{kg}}{\text{kg}_{\text{db}}}$, while the material was below the glass transition temperature. For moisture contents below 0.175, a value of 0.01 was used (Cummings and Okos, 1981). Kowalski and Mielniczuk (2006) measured a value of 0.38 for drying macaroni dough. Both Kowalski and Mielniczuk, and Zhu et al. (2011) used a value of 0.45 for swelling pasta.

2.5.6 Measurement

Stress Relaxation Data

Cummings et al. (1993) collected stress relaxation data on extruded durum semolina and fitted it to a four element generalized Maxwell model (Eq. 2.29 with $N = 4$). To account for the variation in the viscoelastic parameters both temperature and

Table 2.6.
Maxwell model parameters from Cummings et al. (1993)

Parameter	Value
E_a	$0\,\frac{\mathrm{N}}{\mathrm{m}^2}$
E_1	$6.6 \times 10^5\,\frac{\mathrm{N}}{\mathrm{m}^2}$
E_2	$1.8 \times 10^6\,\frac{\mathrm{N}}{\mathrm{m}^2}$
E_3	$2.5 \times 10^6\,\frac{\mathrm{N}}{\mathrm{m}^2}$
E_4	$1.33 \times 10^7\,\frac{\mathrm{N}}{\mathrm{m}^2}$
λ_1	$4.608 \times 10^8\,\mathrm{s}$
λ_2	$5.579 \times 10^7\,\mathrm{s}$
λ_3	$1.316 \times 10^6\,\mathrm{s}$
λ_4	$1.563 \times 10^5\,\mathrm{s}$

moisture shift factors were calculated. These were used to define a reduced time such that the integral equation for determine stress (Eq. 2.28) becomes

$$\sigma(\xi) = \int_{\xi_0}^{\xi} E(\xi - \xi')\dot{\epsilon}(\xi')\,\mathrm{d}\xi' \tag{2.40}$$

where:

$$\xi = t a_T(T) a_M(M) \tag{2.41}$$

The equations that Cummings determined for the temperature and moisture shift factors are:

$$\ln a_M = -73(M - M_0) \tag{2.42}$$

$$\ln a_T = -0.013(T - T_0) \tag{2.43}$$

The reference conditions are $T = 298\,\mathrm{K}$ and $M_0 = 0.14\,\frac{\mathrm{kg}}{\mathrm{kg_{db}}}$.

Rozzi (2002) also determined the temperature and moisture dependence of the viscoelastic material parameters for durum semolina. She used a two-term generalized Maxwell model (Eq. 2.29 with $N = 2$). She calculated the temperature and

moisture dependence of each of the parameters independently. Relaxation times were determined to be independent of temperature and moisture content, but E_2 was a function of moisture content, and E_a and E_1 were functions of both temperature and moisture. The equations for these parameters are as follows:

$$E_a(M,T) = 68.18\left(\left(1+\exp\left\{\frac{M-250.92\exp(-0.0091T)}{2.19}\right\}\right)^{-1}+0.078\right) \quad (2.44a)$$

$$E_1(M,T) = 20.26\exp\left\{-0.0802(M+0.0474T-14.283)\right\} \quad (2.44b)$$

$$E_2(M) = 2.484+\frac{6.576}{1+\exp\{\frac{M-19.36}{0.848}\}} \quad (2.44c)$$

$$\lambda_1 = 7(s) \quad (2.44d)$$

$$\lambda_2 = 110(s) \quad (2.44e)$$

The data used to fit these parameters was taken at 25 °C, 50 °C, and 80 °C, with moisture contents ranging from 7.5% to 29.6% dry basis. For these equations, temperatures are given in Kelvins, and moisture content is in percent wet basis. The E_i moduli have units of MPa.

Creep Compliance Data

Bressani (2014) collected creep compliance data for extruded durum semolina pasta at four different moisture contents, and three levels of applied pressure, and fitted the data to the Burgers equation for creep compliance. She found that creep compliance depended strongly on both moisture content and pressure, with higher pressure resulting in lower creep compliance, and higher moisture content leading to higher creep compliance. There was no observed correlation between either of these parameters and the retardation times in the model.

$$J = J_0+\sum_i J_i\left(1-e^{-\frac{t}{\lambda_{ret,i}}}\right)+\frac{t}{\mu_0} \quad (2.45)$$

Table 2.7.
Burger's material parameters at varying applied stresses and material moisture contents (Bressani, 2014).

X_{db}	σ	σ	J_0	J_1	J_2	λ_1	λ_2	μ_0
$\frac{\text{kg}}{\text{kg}_{\text{db}}}$	kPa	Pa	$\frac{1}{\text{Pa}}$	$\frac{1}{\text{Pa}}$	$\frac{1}{\text{Pa}}$	s	s	Pa s
0.385	20	20 000	5.88×10^{-6}	1.13×10^{-6}	1.02×10^{-6}	2.237	27.485	2.96×10^{8}
0.385	100	100 000	1.87×10^{-6}	1.19×10^{-7}	2.16×10^{-7}	2.058	24.425	1.20×10^{9}
0.385	200	200 000	1.16×10^{-6}	7.75×10^{-8}	1.21×10^{-7}	3.324	30.179	1.45×10^{9}
0.261	20	20 000	4.50×10^{-6}	1.14×10^{-6}	7.67×10^{-7}	1.705	26.527	3.45×10^{8}
0.261	100	100 000	1.63×10^{-6}	1.45×10^{-7}	1.56×10^{-7}	2.282	25.78	1.42×10^{9}
0.261	200	200 000	9.75×10^{-7}	6.66×10^{-8}	6.08×10^{-8}	2.348	29.458	4.16×10^{9}
0.147	20	20 000	4.08×10^{-6}	1.52×10^{-6}	8.57×10^{-7}	1.737	26.658	4.67×10^{8}
0.147	100	100 000	1.28×10^{-6}	1.40×10^{-7}	8.86×10^{-8}	2.304	27.707	3.28×10^{9}
0.147	200	200 000	7.42×10^{-7}	5.73×10^{-8}	5.03×10^{-8}	2.466	27.656	5.25×10^{9}
0.089	200	200 000	5.29×10^{-7}	4.86×10^{-8}	2.57×10^{-8}	2.397	27.039	1.46×10^{10}

Table 2.8.
Bulk modulus parameters for durum semolina (Sozer and Dalgic, 2007).

K_i (Pa)	τ_i (s)
6.709×10^5	0.03
5.312×10^5	0.422
3.694×10^5	3.9
3.216×10^5	98
2.613×10^5	2000
1.1322×10^6	299 990

2.5.7 Bulk Modulus Data

Zhu et al. (2011) took a set of Maxwell model parameters from Sozer and Dalgic (2007) for the Young's modulus of pasta and converted it into a set of bulk modulus parameters using a constant Poisson ratio of 0.45. Her parameters are presented in Table 2.8, and the moisture shift factor is given by Eq. 2.46.

$$\ln a_M = 9.7577(M - 1.8638) \tag{2.46}$$

In order to convert the model from bulk modulus to bulk compliance, they used a formula from Takhar et al. (2003a):

$$B(t) = B_c \sum_{i=1}^{n_k} K_i \exp(-t a_M/\tau_i) \tag{2.47}$$

where B_c is a constant with a value of 8.2×10^{-14} (Takhar et al., 2004). Using this formula takes the place of performing an inverse Laplace transform to obtain bulk compliance.

2.5.8 Conversion Between Models

Between Stress Relaxation and Creep Compliance

It is possible to directly convert Eq. 2.29 into a creep compliance function, $J(t)$. The two equations are related by

$$\int_0^t J(\tau)G(t-\tau)d\tau = t \tag{2.48}$$

The convolution integral can also be Laplace transformed to yield:

$$\hat{J}(s)\hat{G}(s) = \frac{1}{s^2} \tag{2.49}$$

This equation can be solved for the desired function and the inverse transformed to yield either the relaxation modulus or creep compliance function in the time domain. The creep compliance function for a single element Maxwell solid (Eq. 2.29 with $E_a \neq 0$ and $N = 1$) is:

$$J(t) = \frac{1}{E_a}\left(1 - \frac{E_1}{E_1 + E_a}\mathrm{e}^{-\frac{E_a\, t}{\eta_1\,(E_1+E_a)}}\right) \tag{2.50}$$

For relaxation moduli with more than two Maxwell elements, a numerical solution, such as the one presented in Knoff and Hopkins (1972) is best. An alternate solution method to this problem involves an optimized fitting of the relaxation modulus parameters to a generalized Kelvin-Voigt model as described in Mead (1994).

Between Creep Compliance and Bulk Modulus

For elastic materials, it is possible to determine any elastic material parameter given two others. For example, in order to determine the elastic bulk modulus, given Young's modulus and Poisson ratio for that material, the following equation can be used:

$$K = \frac{E}{3(1-2\nu)} \tag{2.51}$$

Additionally, shear modulus can be determined from the same two parameters using this equation:

$$G = \frac{E}{2(1+\nu)} \tag{2.52}$$

Because of the viscoelastic correspondence principle, these relationships can also be applied to viscoelastic materials. In order to do this, the viscoelastic equations are Laplace transformed with respect to time in order to render them in an equivalent form to an elastic equation. Once this is done, all of the elastic equations and solutions can then be applied to the viscoelastic problem, including Eqs. 2.51 and 2.52. Using these two equations, it is possible to separate the viscoelastic creep function, which is the inverse of Young's modulus, into volumetric and deviatoric creep. The general relation between these functions is given in Eq. 2.53 (Bažant, 1975).

$$\nu(t,\tau)J(t,\tau) = \frac{1}{6}J_D(t,\tau) - \frac{1}{9}J_V(t,\tau) \tag{2.53}$$

For the case of constant Poisson ratio, Eq. 2.53 can be simplified and split apart to directly calculate the volumetric creep, or inverse of the viscoelastic bulk modulus (Bažant, 1975).

$$J_V(t,\tau) = 6\left(\frac{1}{2} - \nu\right)J(t,\tau) \tag{2.54}$$

$$J_D(t,\tau) = 2(1+\nu)J(t,\tau) \tag{2.55}$$

2.5.9 Effect of Porosity on Material Parameters

For porous materials undergoing a volumetric change, the void fraction of the solid matrix will change as a function of the current strain. This affects all of the viscoelastic material functions. For elastic moduli, the relationship between porosity and other material properties can be theoretically calculated for certain geometries (Arnold et al., 1996). For the case of low porosity and spherical pores, bulk modulus can be expressed as:

$$K(\phi) = K_0\frac{2(1-2\nu_0)(3-5\phi)(1-\phi)}{2(3-5\phi)(1-2\nu_0) + 3\phi(1+\nu_0)} \tag{2.56}$$

For high porosity, the relation is:

$$K(\phi) = K_0 \frac{2(1-2\nu_0)(1-\phi)}{3(1-\nu_0)} \tag{2.57}$$

The variation in Poisson ratio as a function of pore size can be expressed as:

$$\nu(\phi) = 0.5 - \frac{(1-\phi^{2/3})^{1.21}[2(3-5\phi)(1-2\nu_0)+3\phi(1+\nu_0)]}{4(3-5\phi)(1-\phi)} \tag{2.58}$$

For all of these equations, ϕ is the porosity, and ν_0 is the Poisson ratio when the porosity is equal to zero. Other mechanical properties besides Poisson ratio, such as elastic modulus, also vary with porosity (Wang, 1984).

2.6 Glass Transition Temperature

2.6.1 Gordon-Taylor Model

The Gordon-Taylor model for glass transition temperature relates the T_g or a mixture of two components to its composition and the glass transition temperatures of each pure component.

$$T_g = \frac{w_1 T_{g1} + k_{G-T} w_2 T_{g2}}{w_1 + k_{G-T} w_2} \tag{2.59}$$

w_1 is the mass fraction of dry solids, w_2 is the mass fraction of water, T_{g1} is the glass transition temperature of the bone-dry solid, T_{g2} is the glass transition temperature for glassy water, and k_{G-T} is a material-specific constant that quantifies the plasticizing effect of water on the solid material (Cuq and Icard-Verniere, 2001).

2.6.2 Kwei Model

The Gordon-Taylor equation can be improved by adding a parameter to quantify the amount of deviation from the theoretical plasticizing effect of water on the solid is exhibited.

$$T_g = \frac{w_1 T_{g1} + k_{G-T} w_2 T_{g2}}{w_1 + k_{G-T} w_2} + q w_1 w_2 \tag{2.60}$$

The q parameter is purely empirical (Cuq and Icard-Verniere, 2001).

Table 2.9.
Gordon-Taylor parameters for durum semolina (Cuq and Icard-Verniere, 2001).

Process	T_g (water) K	T_g (flour) K	k_{G-T}
Cooling	138	435	3.4
Heating	138	449	4.2
Re-heating	138	498	5.5

Table 2.10.
Kwei parameters for durum semolina (Cuq and Icard-Verniere, 2001).

Process	T_g (water) K	T_g (flour) K	k_{G-T}	q
Cooling	138	546	9.5	346
Heating	138	518	9.6	277
Re-heating	138	589	12.1	304

2.6.3 Williams-Landel-Ferry Model

In order to quantify the change in viscosity near the glass transition temperature, the empirical WLF equation can be used (Adam and Gibbs, 1965).

$$\ln a_T = \frac{-C_1(T - T_s)}{C_2 + (T - T_s)} \tag{2.61}$$

Here C_1 and C_2 are material-specific constants, and T_s is the reference temperature. This equation describes the temperature shift factor of the material viscosity or other viscoelastic material parameters (such as Maxwell relaxation function), and provides a good in the temperature range of T_g to $T_g + 100K$. For temperatures outside of this range, an Arrhenius relation is likely to be a better fit (Heldman et al., 2006).

The C_1 and C_2 constants are dependent on the moisture content of the sample via the glass transition temperature. The values of the constants at new moisture contents can be estimated using the old values and the following equations:

$$C_1' = C_2 + T_g - T_g' \tag{2.62a}$$

$$C_2' = \frac{C_1 C_2}{C_2 + T_g - T_g'} \tag{2.62b}$$

where $(\cdot)'$ indicates the value at the new moisture content (Yildiz and Kokini, 2001). The new value of the glass transition temperature can be calculated using either Eq. 2.59 or Eq. 2.60.

2.6.4 Literature Glass Transition Values

The Gordon Taylor and WLF models for glass transition temperature only report a single temperature for a given moisture content. In a real system, the glass transition temperature is a range, since various components of the material could go through the glass transition at different moisture contents. For durum semolina flour, the glass transition region is detailed in Table 2.11 (Rozzi, 2002).

Table 2.11.
Glass transition region for durum semolina (Rozzi, 2002; Sterling, 2000).

Moisture Content $\frac{\text{kg}}{\text{kg}_{\text{wb}}}$	T_g Onset °C	T_g Midpoint °C	T_g Endpoint °C	Source
8.7	44.2	72.1	112.6	Sterling (2000)
9.3	42.6	67.2	99.7	Sterling (2000)
12.2	29.7	52.6	90.2	Sterling (2000)
13.5	24.2	46.9	75.8	Sterling (2000)
15.8	22.6	39.5	56.1	Sterling (2000)
19.2	20.4	30.4	39.3	Sterling (2000)
25.3	19.7	27.4	55.3	Rozzi (2002)
29.6	1.2	25.4	52.1	Rozzi (2002)

Fig. 2.5. Glass transition region for durum semolina (Rozzi, 2002; Sterling, 2000).

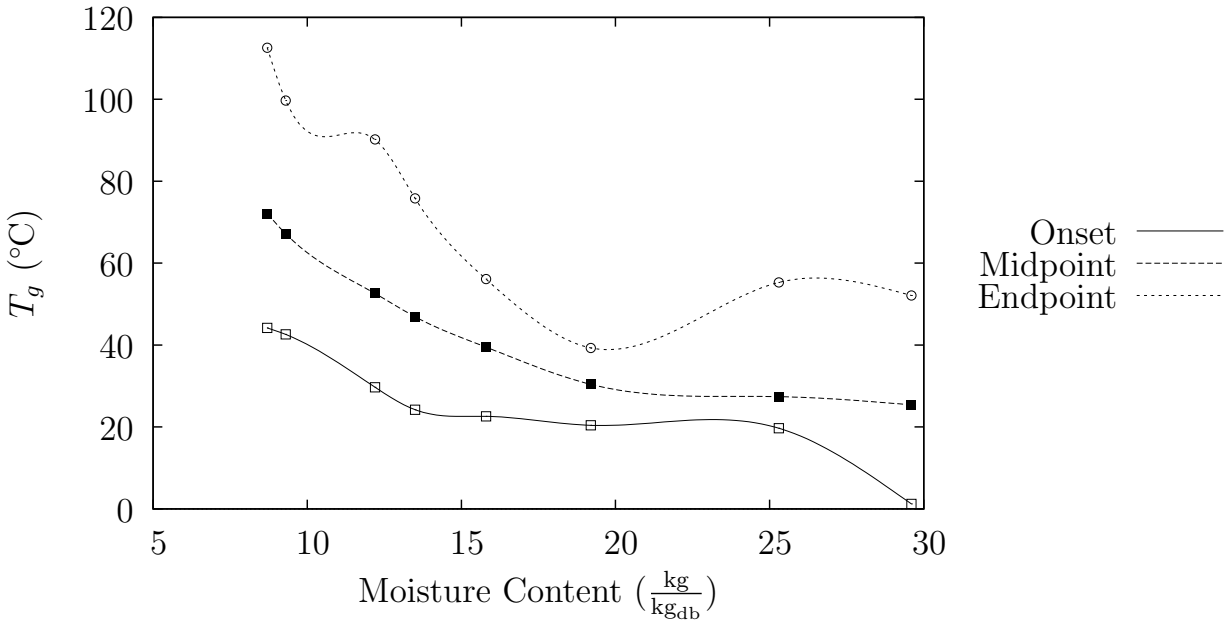

2.6.5 Case Hardening

At low moisture contents, the effective diffusivity of the pasta samples decreases dramatically. Additionally, the solid matrix goes through a glass transition and becomes more elastic and less viscous. During a drying process, if a sharp moisture gradient occurs near the surface of the sample, then a diffusion barrier can form which limits the rate of drying. Litchfield and Okos (1992) dried pasta and examined the moisture profiles by freezing and sectioning the samples. They found that the moisture profiles were flatter than expected, indicating that there was likely case hardening in a thin layer on the surface. This was validated by Hills et al. (1997) who used NMR to measure the moisture profiles. The moisture profiles they observed displayed the steep surface gradient as expected.

2.7 Moisture Transport

Multiple models are available to describe the flow of fluid through a porous media. However, when considering shrinkage, the velocity of the media through which the fluid is flowing is also important. In order to factor this in, the following equation is used (Thiffeault, 2003):

$$\frac{\partial c}{\partial t} + \underline{v} \cdot \nabla c = \frac{1}{\rho} \nabla \cdot (\rho D \cdot \nabla c)$$

where $\underline{v}$ is the solid-phase velocity, c is the mass concentration, and ρ is the density of the mixture.

2.7.1 Fick's Law

Fick's Law of diffusion relates the concentration gradient of a fluid to its flux. For unsteady state problems, this law can be stated as:

$$\frac{\partial c}{\partial t} = \nabla \cdot (D \nabla c)$$

For constant diffusion coefficient and a one-dimensional geometry, the equation can be simplified to:

$$\frac{\partial c}{\partial t} = D\frac{\partial^2 c}{\partial x^2} \tag{2.63}$$

Applying Fick's Law to mass transport in drying assumes that the material is homogeneous, and the factors that effect rate of moisture transport are lumped into a single effective diffusivity coefficient that is a function of both temperature and moisture content. This coefficient accounts for porosity, pressure, and moisture binding (Waananen and Okos, 1996), as well as the effects of shrinkage (Frias et al., 2002). In order to determine pore formation with Fick's law, an additional balance equation is required to determine the amount of air/vapor in the product as it dries (Katekawa and Silva, 2006).

If the diffusivity and dimensions of the drying sample remain constant throughout the process, then Eq. 2.63 has an exact series solution. For the case of a flat sheet starting at a uniform initial concentration with equal surface concentrations, the moisture content during drying can be expresses as

$$\frac{c - c_0}{c_1 - c_0} = 1 - \frac{4}{\pi}\sum_{n=0}^{\infty}\frac{(-1)^n}{2n+1}\exp\left\{\frac{-D(2n+1)^2\pi^2 t}{4l^2}\right\}\cos\frac{(2n+1)\pi x}{2l} \tag{2.64}$$

where c is the moisture content at point x along the thickness of the slab, c_0 is the initial moisture content, and c_1 is the moisture content at the boundary of the slab (Crank, 1956). To obtain the moisture content of the whole slab as a function of time under the same conditions, the solution is (Bressani, 2014)

$$\frac{X_{db} - X_e}{X_0 - X_e} = \sum_{n=0}^{\infty}\frac{8}{(2n+1)^2\pi^2}\exp\left\{\frac{D(2n+1)^2\pi^2 t}{L^2}\right\} \tag{2.65}$$

The quantity $k_F = \frac{\pi^2 D}{L^2}$ can be isolated from this equation. This serves as a sort of diffusive constant that incorporates both length and diffusivity into one value. If all but the first term of Eq. 2.65 can be neglected to give a long-time solution that is useful for analyzing drying curves to determine diffusivity.

$$\frac{X_{db} - X_e}{X_0 - X_e} = \exp\{-k_F t\} \tag{2.66}$$

Additionally, this equation can be used to determine the equilibrium moisture content of the sample without waiting for the sample to completely equilibrate. (Waananen, 1989)

2.7.2 Darcy's Law

Darcy's law describes pressure driven flows in porous media. The equation relates fluid flux to pressure gradient as follows:

$$v_0 = \frac{\kappa}{\mu}(\nabla P - \rho \underline{g})$$

where v_0 is the superficial velocity, κ is the permeability of the medium, μ is the fluid viscosity, and $\rho \underline{g}$ is the effect of gravity on the fluid (Bird et al., 2007). Darcy's Law commonly replaces Fick's Law for moisture transport in unsaturated systems, and for isothermal drying conditions, it, in fact, becomes equivalent to Fick's first law. This approach offers several advantages to using a Fick's Law model in that it correctly describes the system as heterogeneous (Achanta et al., 1997), and it allows for modeling of pore formation during drying. As with Fick's law, in order to account for the difference in water lost and shrinkage observed during drying, an additional balance equation is added to account for air in the pores (Katekawa and Silva, 2006; Zhu et al., 2011).

Permeability

Permeability for porous media is commonly written as the product of an intrinsic permeability and a relative permeability ($\kappa = \kappa_i \kappa_r$). Intrinsic permeability represents the permeability of the porous medium when it is completely saturated, and is purely a function of the pore structure:

$$\kappa_i = \frac{1}{8\tau} \sum_i \Delta\beta_i r_i^2$$

where τ is tortuosity, and $\Delta\beta_i$ is the volume fraction of pores with radius r_i (Datta, 2006). Relative permeability is a value between zero and one that describes how

Table 2.12.
Several models for relative permeability for both liquid water and water vapor

Source	κ_v	κ_l
Lipinski (1980)	$1 - 1.1S$	S^3
Saez & Carbonell (1985)	$(1 - S)^{4.8}$	$\left(\frac{S-S_r}{1-S_r}\right)^{2.43}$
Schulenberg & Muller (1984)	$\left(1 - \frac{S-S_r}{1-S_r}\right)^3$	S^3

the total fluid permeability decreases as the porous media becomes less saturated, and it is assumed to be independent of pressure gradient, total flow rate, and fluid properties (Bear et al., 1991). Relative permeability is at a maximum when the material is saturated and is zero when the fluid saturation drops below the irreducible saturation for that material.

Irreducible saturation is the point below which the fluid in the porous media will no longer flow under normal circumstances. This is due to some of the water being retained in the network of pores by capillary forces. The amount of water retained can be determined experimentally using either a drainage column for particles with a diameter of 2 mm or larger, and a pressure membrane for smaller particles (Morrow, 1970).

Darcy's Law Modifications

Achanta et al. (1994) developed a modified version of both Fick's law and Darcy's law to account for the interaction potential present in multiphase systems, particularly during swelling or drying of hydrophilic, porous materials. The models were derived for a three-phase system using hybrid mixture theory. In addition to the interaction potential, an important consequence of this model is that it is able to predict the

correct exponential trend for relating pore width with swelling pressure in a clay-water system.

2.8 Effective Diffusivity Models

2.8.1 Purely Empirical Models

Andrieu and Stamatopoulos (1986) found that the effective diffusivity had three distinct regions depending on the moisture content of the sample, and that the diffusivity was constant within those regions (Andrieu and Stamatopoulos, 1986). Diffusivity was highest when the sample was in the high moisture plastic-type zone, and lowest in the low moisture elastic zone. Temperature dependence was best modeled using an Arrhenius-type equation, with activation energy being nearly constant for all moisture contents ($E_a = 22.5(50)\,\frac{\text{kJ}}{\text{mol}}$). The values they calculated for effective diffusivity are presented in Table 2.13.

Villeneuve and Gélinas modeled diffusivity of both bran-rich and bran-free pasta using an Arrhenius-type equation. For bran-rich pasta, they modeled diffusivity using Eq. 2.68 and Eq. 2.69, and for bran-free, they used Eq. 2.67 and Eq. 2.69 (Villeneuve and Gélinas, 2007).

$$\ln D_{eff0} = -0.0221 a_w - 8.635 \tag{2.67}$$

Table 2.13.
Effective diffusivity as a function of moisture content and geometry at T=60 °C (Andrieu and Stamatopoulos, 1986).

Moisture Content $\frac{\text{kg}}{\text{kg}_{\text{db}}}$	Cylinder (spaghetti) $\frac{\text{m}^2}{\text{s}}$	Slab (disc) $\frac{\text{m}^2}{\text{s}}$
$X > 0.27$	0.41×10^{-10}	0.41×10^{-10}
$0.18 < X < 0.27$	0.24×10^{-10}	2.4×10^{-10}
$0.136 < X < 0.18$	0.15×10^{-10}	0.16×10^{-10}

$$\ln D_{eff0} = -0.0358 a_w - 7.604 \tag{2.68}$$

$$\ln D_{eff} = \frac{-E_a}{R(T + 273.15} + \ln D_{eff0} \tag{2.69}$$

De Temmerman et al. used a similar model to describe diffusivity of semolina pasta. Their model had the form:

$$D = a \exp(-d/T) \exp(bX) \tag{2.70}$$

where T and X are the temperature in Kelvins, and the dry-basis moisture content, respectively. The values for the constants are $a = 1.2 \times 10^{-7}$, $b = 6.46$, and $d = 3036.95$ (Temmerman et al., 2007).

Litchfield and Okos calculated the effective diffusivity for slabs of extruded durum semolina pasta from experimental data, and fitted the data to an empirical model of the form:

$$D' = (1 \times 10^{-12}) A \exp(-B/T)[(1 - \exp(-CM^D)) + M^E] \tag{2.71a}$$

$$A = 2.3920 \times 10^5 \tag{2.71b}$$

$$B = 3.1563 \times 10^3 \tag{2.71c}$$

$$C = 7.9082 \times 10^{14} \tag{2.71d}$$

$$D = 15.706 \tag{2.71e}$$

$$E = 0.685\,89 \tag{2.71f}$$

where A, B, C, D, and E are constants determined from nonlinear regression analysis (Litchfield and Okos, 1992). The empirical model predicts diffusivity between 40 °C and 85 °C and moisture contents between 1.5 and 26% dry basis. However, the model did not accurately predict the drying rate at high temperature and low moisture content.

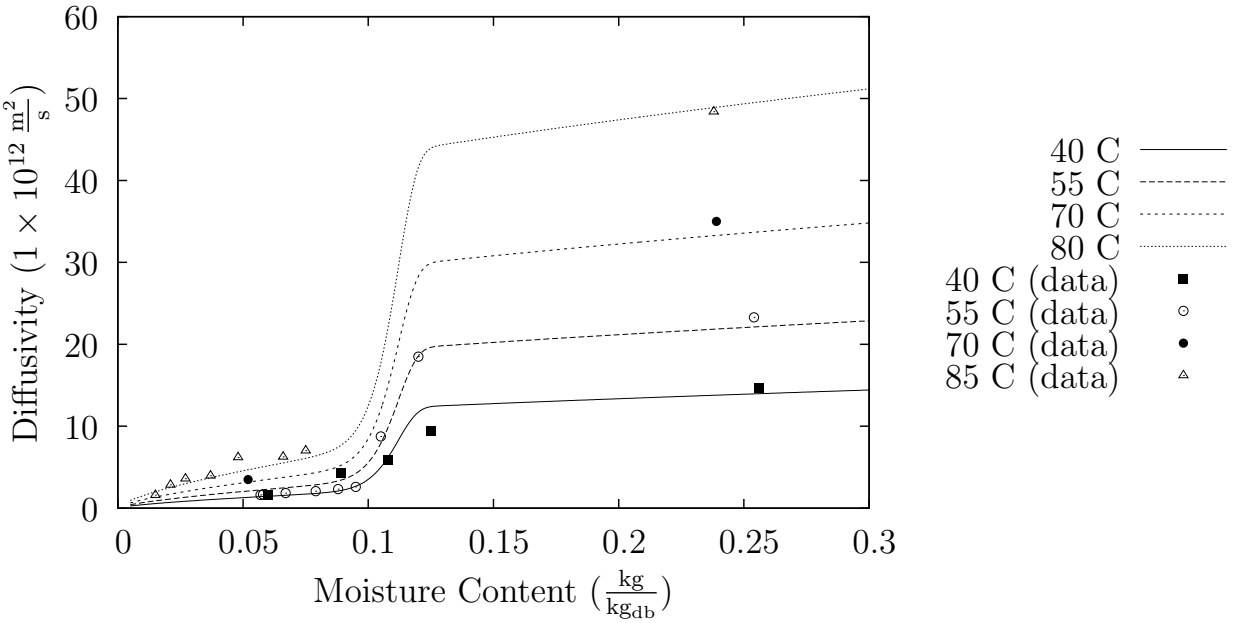

Fig. 2.6. Eq. 2.71 compared to the data from Litchfield and Okos (1992).

2.8.2 Semi-Empirical Models

Xiong et al. developed a semi-empirical model for predicting both liquid and vapor diffusivity in porous media based on the binding energy of the liquid phase to the solid matrix. Binding energy was calculated using the Clausius-Clapeyron equation,

$$-\frac{E_b}{T^2} = R\left[\frac{\partial \ln a_w}{\partial T}\right]_{P,w} \tag{2.72}$$

and then diffusivity was calculated using an Arrhenius style equation (Xiong et al., 1992). Water activity was calculated using the Oswin model (Eq. 2.5).

$$\frac{D}{D_0} = \mathrm{e}^{-E_a/RT}\frac{K\mathrm{e}^{-E_b/RT}}{1+K\mathrm{e}^{-E_b/RT}} \tag{2.73}$$

$$K = 1032.558 \tag{2.74a}$$

$$E_a = 5.20\,\frac{\text{kcal}}{\text{mol}} \tag{2.74b}$$

$$D_0 = 6.3910\times10^{-8}\,\frac{\text{m}^2}{\text{s}}\text{(for liquid water) (Heldman et al., 2006)} \tag{2.74c}$$

$$D_0 = 2\times10^{-5}\,\frac{\text{m}^2}{\text{s}}\text{(for water vapor)} \tag{2.74d}$$

This approach successfully predicted the liquid diffusivity for both puffed durum semolina pasta (porosity of 26.86%) and regular durum semolina pasta (porosity of 6.12%).

To better account for the effect of porosity and pressure on effective diffusivity, Waananen and Okos (1996) developed a model that incorporated both sample porosity and drying pressure as well as temperature and moisture content. The semi-empirical model that they derived is presented in Eq. 2.75.

$$D_{eff}^{total} = \left(C'_{10}+\epsilon\frac{C'_{20}}{P_T}\right)\exp\left(-\frac{6.0\exp(-20X)+E_a}{RT}\right) \tag{2.75}$$

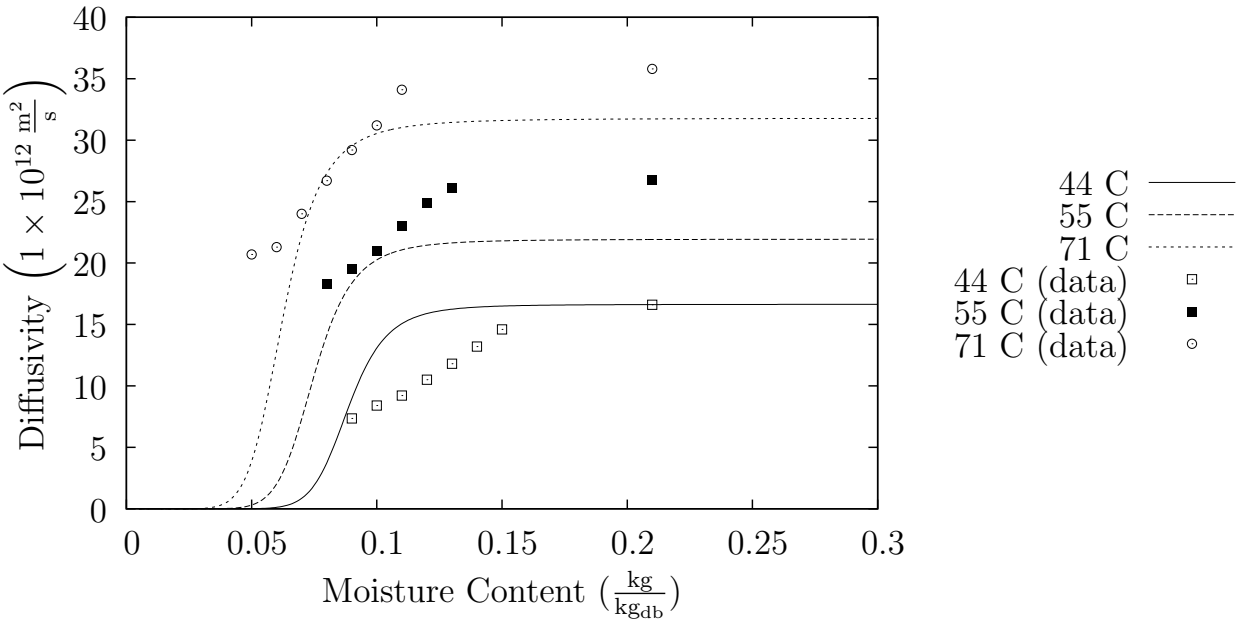

Fig. 2.7. Eq. 2.73 compared with the data from Xiong et al. (1992) for regular pasta.

$$C'_{10} = 1.2 \times 10^{-7}\,\frac{\mathrm{m}^2}{\mathrm{s}} \tag{2.76a}$$

$$C'_{20} = 8.0 \times 10^{-5}\,\frac{\mathrm{m}^2}{\mathrm{s}} \tag{2.76b}$$

$$E_a = 22.6\,\frac{\mathrm{kJ}}{\mathrm{mol\,K}} \tag{2.76c}$$

2.8.3 Theoretical Models

Achanta (1993) developed a model for effective diffusivity based on Darcy's law, which he used to model drying of both puffed and regular pasta. The Darcy's law equation used to derive the diffusivity model was modified to include a wettability potential term, which accounts for capillary interactions. The driving force for flow was taken to be chemical potential (Achanta, 1993).

$$D_{eff}^{total} = \frac{\underline{\underline{K}}\rho_w}{\eta_w(1-\epsilon)\rho^s}(\rho^w RT)\frac{\partial \ln a_w}{\partial X} + \frac{< \rho^v >^v D^*_{eff}\frac{\partial}{\partial X}\left[\frac{<\rho_w^v>^v}{<\rho^v>^v}\right]}{\rho^w\left(1 - \frac{<\rho_w^v>^v}{<\rho^v>^v}\right)} \tag{2.77}$$

$$< \rho^v >^v = \frac{353.4P_0}{T} - 0.611 < \rho_w^v >^v \tag{2.78}$$

$$< \rho_w^v >^v = \frac{p_v^0 a_w}{R_w T} \tag{2.79}$$

Here, K represents the permeability of the porous media, η_w is the viscosity of water, p_v^0 is the vapor pressure of water, and P_0 is the total pressure of the vapor phase. The variable $< \rho^v >^v$ is the volume averaged density of the vapor phase, and $< \rho_w^v >^v$ is the volume averaged density of water in the vapor phase. Vapor diffusivity is given by D^*_{eff}.

This model is very sensitive to the shape of the isotherm used to predict water activity, and small changes can lead to large deviations from experimental diffusivity results (Achanta, 1993).

Vapor phase diffusivity at low pressures can be calculated from kinetic theory of gasses. At atmospheric pressure, the deviation from experimental results is approximately 6-8%.

$$\frac{pD_{ab}}{(p_{cA}p_{cB})^{1/3}(T_{cA}T_{cB})^{5/12}(1/M_A + 1/M_B)^{1/2}} = a\left(\frac{T}{\sqrt{T_{cA}T_{cB}}}\right)^b \tag{2.80}$$

Here, diffusivity is given in $\frac{\text{cm}^2}{\text{s}}$, pressure is in atm, and temperatures are in units of Kelvin. For water vapor in air, $a = 3.640 \times 10^{-4}$ and $b = 2.334$ (Bird et al., 2007).

2.8.4 Tortuosity

Two factors that can significantly impact effective diffusivity in porous media are porosity and tortuosity (Mittal, 1999).

$$D_e = \frac{\phi}{\tau} D_v \tag{2.81}$$

Porosity can be measured using a technique such as mercury intrusion porosimetry, but tortuosity is more difficult to measure (Matyka and Koza, 2012). It can be estimated either from the vorticity field of the fluid flowing through the solid skeleton (Matyka and Koza, 2012), or by using a model, such as those presented in Table 2.14.

Table 2.14.
Tortuosity models for various pore geometries (Shen and Chen, 2007).

Relationship	Usage
$\tau^2 = (3-\phi)/2$	Ordered Packing
$\tau^2 = (3-\phi)/2$	Random homogeneous isotropic sphere packing
$\tau^2 = 2-\phi$	A hyperbolic revolution
$\tau^2 = \phi^{-1/2}$	Not for monosized spheres
$\tau^2 = \phi^{-1/3}$	Partly saturated homogeneous isotropic monodispherse sphere packing
$\tau^2 = 1-\ln\frac{\phi}{2}$	Overlapping spheres
$\tau^2 = 1-\ln\phi$	Random arrays of freely overlapping cylinders
$\tau^2 = \frac{\phi}{1-(1-\phi)^{1/3}}$	Heterogeneous catalyst
$\tau^2 = \left(\frac{2-\phi}{\phi}\right)^2$	Cation-exchange resin membrane

2.9 Heat Transfer

Heat transfer is handled by applying Fourier's law of heat conduction.

$$\rho C_p \frac{\partial T}{\partial t} = \nabla \cdot (k \nabla T) \tag{2.82}$$

For the case of constant density, heat capacity, and thermal conductivity, this equation can be simplified to:

$$\frac{\partial T}{\partial t} = \alpha \nabla^2 T \tag{2.83}$$

where α is the thermal diffusivity. Both moisture flow and material shrinkage can affect the rate of heat flow. To account for the effect of shrinkage on the rate of heat transfer, an approach similar to Eq. 2.17 can be employed. Chemkhi et al. (2004) does this for drying potato by modifying Fourier's law to include a shrinkage coefficient which was also used to determine the amount of drying-induced strain. Alternatively, Perré and Passard (2004) used an enthalpy balance instead of Fourier's law to account for the effect of moisture flux on heat flow during drying of timber. This also accounted for the energy required to vaporize the water in the drying medium. If the amount of shrinkage is a state variable in the system, then it also needs to be accounted for in the mass transport equations (Katekawa and Silva, 2006).

For most cases, heat transfer occurs at a much faster rate than mass transfer. Because of this, the drying process can be modelled as isothermal, neglecting heat transfer entirely.

3. MATERIALS AND METHODS

3.1 Dough Preparation

The pasta dough was prepared for extrusion by mixing Bob's Red Mill durum semolina flour with distilled water and sodium propionate (mold inhibitor) at room temperature. Sodium propionate was mixed directly with the flour (approximately 1 g per 300 g_{flour}). The flour was assumed to have an initial moisture content of 0.15 $\frac{kg}{kg_{db}}$, and the mass of water required to increase the moisture content to 0.53 $\frac{kg}{kg_{db}}$ was calculated. The flour was mixed in a KitchenAid Professional 6 stand mixer on the lowest speed setting using the whisk attachment. Water was added using a spray bottle in a fine mist to ensure even distribution throughout the flour. The total mixing time was kept to between 60 s to 120 s to prevent complete formation of the gluten network within the dough to ensure it was suitable for extrusion. The dough was then left to equilibrate for approximately 24 h at room temperature to ensure even distribution of moisture. The exact processing parameters for each dough batch are presented in Table 3.1

Table 3.1.
Dough processing parameters

Batch	Flour	Water	Inhibitor	Mixing Time	Equilibration Time
	g	g	g	s	h
1	346.1	116.4	1.1	124	17.5
2	348.6	116.0	1.1	91	39.95
3	340.1	114.8	1.0	80	21.5
4	356.7	120.5	1.0	84	43.88

3.2 Extrusion

Pasta samples were prepared using a single screw Brabender extruder (Type 2523) with a coat hanger die (shown in Fig. 3.1). The die slit dimensions were 1.5 mm by 100 mm. The pasta dough was extruded at 40 RPM, and the temperature of the barrel was controlled. The first three zones of the barrel (from the feed section) were set to 40 °C, 53 °C and 57 °C. The die temperature was also set to 57 °C. While the product was extruding, it was allowed to hang freely from the die, perpendicular to the extruder barrel. The sheet emerging from the die was cut free and stored after approximately 20 cm had emerged. After extrusion, the pasta sheet was cut and stored in plastic wrap to prevent it from drying out.

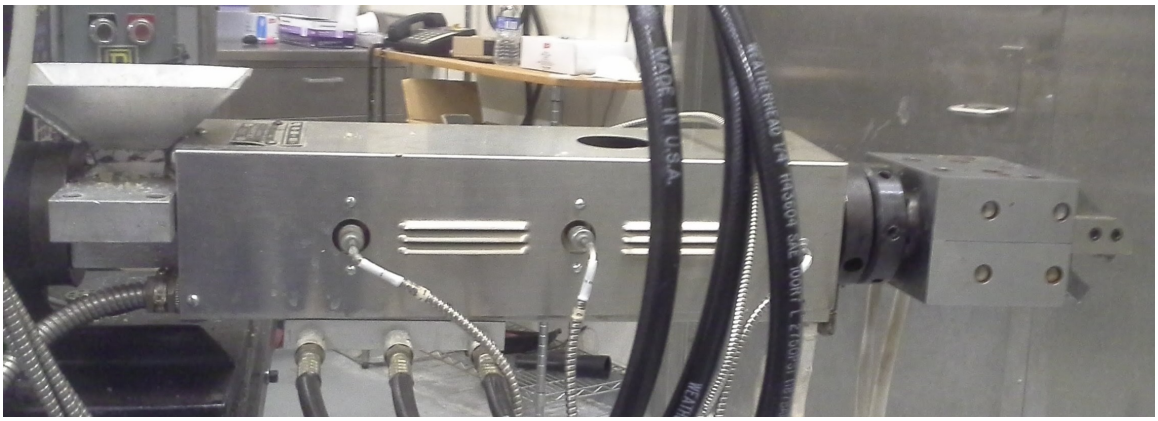

Fig. 3.1. Brabender extruder barrel

3.3 Drying

3.3.1 Humidity Controlled Chambers

In order to control the humidity and temperature of the pasta samples while they dry, multiple drying chambers were built using one quart mason jars. A metal pole was suspended from the lid, and this rod held a screen. A 40 mm CPU case fan was also suspended from the lid of the jars to improve air circulation within the jar and to increase the mass transfer coefficient. The fans were all attached to a single HP Harrison 6205B Dual DC power supply. A saturated salt solution was prepared and placed in the bottom of the jar below the sample screen. Each jar was then placed in one of two Blue M temperature controlled ovens (Model: OV-490A-2). The drying setup is shown in Fig. 3.3.1, and a diagram of the jars that were used to house each sample is presented in Fig. 3.3.

The relative humidity over the salt solutions was determined from the regression equations presented in Greenspan (1977), which are reproduced in Table 3.2. The

(a) Blue M drying oven (b) Jar setup inside drying oven

Fig. 3.2. Drying setup for salt solution-controlled trials. The oven, jars, and power supply are shown.

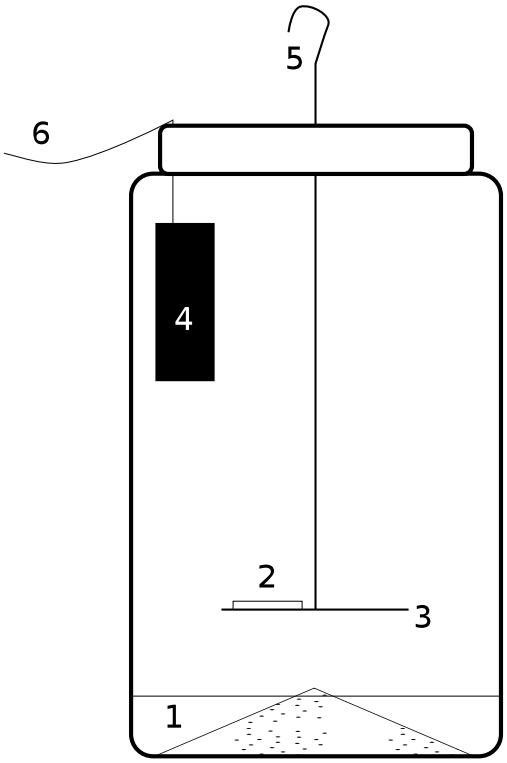

1. Saturated salt solution
2. Sample
3. Mesh platform
4. Fan
5. Scale attachment point
6. Fan power cable

Fig. 3.3. Diagram of drying apparatus.

water activities of the salt solutions used in these trials at the chosen temperatures are presented in Table 3.3. The relative humidity at which the glass transition temperature occurs in each case is presented for comparison. The moisture content at which the glass transition temperature occurs for each temperature was calculated using the Gordon-Taylor equation (Eq. 2.59) using data from Cuq and Icard-Verniere (2001). The corresponding water activity was determined using the Oswin isotherm model (Eq. 2.5) and data from Xiong et al. (1992).

Table 3.2.
Regression equations for water activity of salt solutions as a function of temperature (°C) (Greenspan, 1977).

Salt	Equation	Range
$LiCl$	$a_w = 11.2323 - 0.00824245T - 0.214890 \times 10^{-3}T^2$	0 °C to 100 °C
K_2CO_3	$a_w = 43.1315 - 0.00147523T$	0 °C to 80 °C
$NaCl$	$a_w = 75.5164 + 0.0398321T - 0.265459 \times 10^{-2}T^2 + 0.2848 \times 10^{-4}T^3$	0 °C to 80 °C
KNO_3	$a_w = 96.3361 + 0.0112371T - 0.484514 \times 10^{-2}T^2$	0.6 °C to 48.1 °C
K_2SO_4	$a_w = 98.7792 - 0.0590502T$	0.5 °C to 52.3 °C

Table 3.3.
Water activities over selected salt solutions and temperatures (Cuq and Icard-Verniere, 2001; Greenspan, 1977; Xiong et al., 1992)

Salt	40 °C	60 °C	80 °C
$LiCl$	0.1056	0.099 64	0.091 98
K_2CO_3	0.4307	0.4304	0.4301
$NaCl$	0.7469	0.7450	0.7630
KNO_3	0.8903	0.7957	0.6623
K_2SO_4	0.9642	0.9523	0.9406
T_g	0.8398	0.7802	0.7497

(a) AES drying chamber

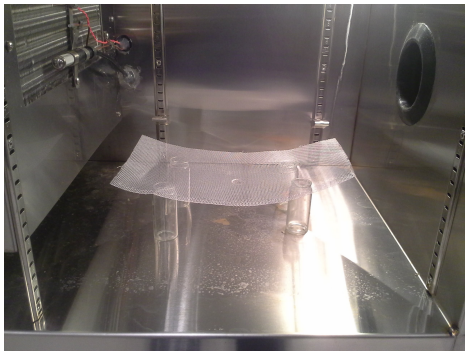

(b) Mesh platform used to hold samples during drying

Pasta slabs measuring approximately 15 mm by 15 mm were placed in the drying chambers and dried until they their mass reached the expected equilibrium value. The samples were weighed before adding them to the jars and after removal. The masses were also recorded periodically during the drying period.

3.3.2 AES Drying Chamber

In addition to the one quart mason jars, samples were dried in an Associated Environmental Systems model BHD-402 chamber, shown in Fig. 3.3.2. Samples were cut to the same size as those dried in the mason jars, and they were placed on an aluminum screen of the same material as the ones used in the drying jars. The temperature and humidity were monitored using the installed Watlow F4 controller.

3.3.3 Freeze Drying

Several samples were also dried using a freeze dryer to try to minimize shrinkage. The freeze dryer used the recipe listed in Table 3.4 to ensure that the temperature was below the glass transition temperature of the samples and that all the moisture was driven off. The samples were cut into approximately 15 mm by 15 mm slabs, their area and mass were recorded, and they were placed in individual metal pans. The

Table 3.4.

Freeze dryer recipe

	Step #	Temperature (°C)	Vacuum (mTorr)	Time (min)
Thermal	1	-40	330	240
	1	-25	300	300
	2	-20	300	300
	3	-15	300	300
	4	-10	300	300
Drying	5	-5	300	300
	6	0	300	300
	7	5	300	300
	8	10	300	300
	9	20	300	300
Post Heat	1	30	300	120

first batch was placed directly into the freeze dryer, and the second batch was frozen to a temperature of $-12\,^{\circ}\mathrm{C}$ before it was freeze dried. Once the freeze drying cycle was complete, the samples were removed and characterized.

3.4 Shrinkage Measurement

In order to determine the volume change of the samples as a result of the loss of moisture, the area of each sample was determined optically. This was accomplished by taking a picture of each sample next to a grid of known spacing and counting the number of pixels representing the sample. By comparing this to the reference for each picture, the area of each sample can be calculated to a high degree of precision. The reference used was a ruler with a 0.1 in. grid, and an area of $0.1\,\mathrm{in.}^2$ was selected from

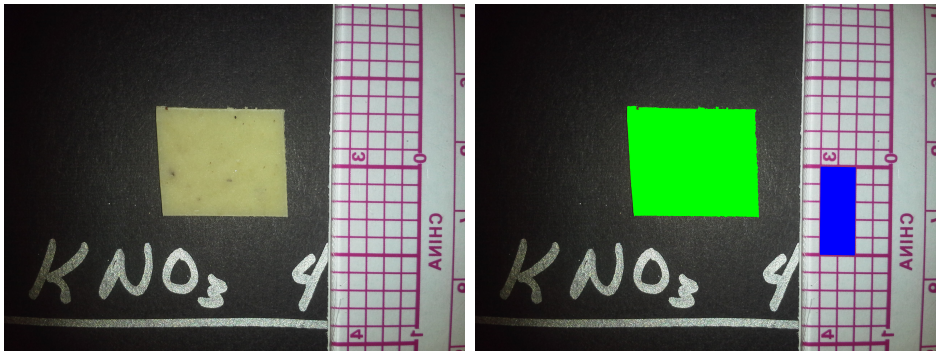

(c) Pre-analysis image (d) Post-analysis image

Fig. 3.4. Area measurement example. Sample area is highlighted in green, and the reference area is highlighted in blue.

each image to serve as the reference area. This analysis was carried out using GIMP version 2.8.14 (`http://www.gimp.org/`), and an example is provided in Fig. 3.4.

This method was chosen over mechanically measuring the thickness of the samples with a caliper to eliminate error due to the samples deforming under the pressure of the caliper tips, as well as deforming while drying. Especially when the samples were soft, the force applied by the caliper was sufficient to deform the samples. Then, as the slabs of pasta dried, they warped, which made the surface uneven and thickness measurements difficult. Visually determining the area of the samples eliminates the first source of error, and minimizes the effect of the second.

3.5 Moisture Content Determination

Once the samples had been dried over the salt solutions and characterized, they were placed in an American Scientific Products oven (Model: DN-81) for further drying at 90 °C for 48 hours in order to drive off all remaining water. The area of the samples was again measured and compared to the initial area to determine the amount of shrinkage for this period.

3.6 Mass Transfer Coefficient

In order to determine the effect of convection on the drying process, the convective mass transfer coefficient for each of the mason jars was estimated as a function of temperature and relative humidity. This was done by placing a pair of vials filled with water in the jar above the salt solution and then placing the jars in an oven at the desired temperature. The change in mass of the water in the vials was then recorded periodically, and this was used to estimate the mass transfer coefficient using Eq. 3.1.

$$N_w = k_c(c - c_a) \tag{3.1}$$

The vials used had a mouth with an inner diameter of 8.04 mm, and the inner diameter of the rest of the vial was 12.57 mm.

4. RESULTS AND DISCUSSION

4.1 Mass Transfer Coefficient

The calculated mass transfer coefficients for the air inside the drying jars, shown in Table 4.2, are on the order of $\mathcal{O}(1)$, and the largest possible effective diffusivity on the order of 10^{-9}. It can be concluded that the mass transfer Biot number for this system is large ($Bi > 100$), and the surface of the drying slab can be assumed to reach the equilibrium moisture content instantaneously. This means the nearly all the resistance to mass transfer is internal and a result solely of the effective diffusivity.

Table 4.1.
Rate of evaporation (fitted equations)

Salt	Temperature	Slope	95% CI	Intercept	95% CI	R^2
K_2CO_3	40 °C	9.77×10^{-6}	$\pm 5.06 \times 10^{-7}$	0.0602	±0.0297	0.9919
$NaCl$	40 °C	5.64×10^{-6}	$\pm 1.96 \times 10^{-6}$	0.0540	±0.1147	0.7320
K_2CO_3	60 °C	1.83×10^{-5}	$\pm 4.01 \times 10^{-6}$	0.5184	±0.7732	0.9119
$NaCl$	60 °C	1.07×10^{-5}	$\pm 9.60 \times 10^{-7}$	0.136	±0.185	0.984

Table 4.2.
Calculated mass transfer coefficient ($\frac{\mathrm{m}}{\mathrm{s}}$)

Salt	60°C
K_2CO_3	3.765
$NaCl$	4.503

4.2 Drying Results

4.2.1 Drying Rate

Drying curves were collected for some of the temperatures examined. Due to the high convective mass transfer coefficient, the pasta samples reached equilibrium relatively quickly during the drying process in all cases (within 6 h). The drying curves for 40 °C are presented in Figure 4.1

In order to attempt to study the rate of shrinkage vs. rate of drying, the AES humidity control chamber was set to 60 °C and 43% relative humidity. Fifteen pasta samples were loaded, and then they were removed periodically during the drying process, three at a time. The change in area with time is plotted in Fig. 4.2.

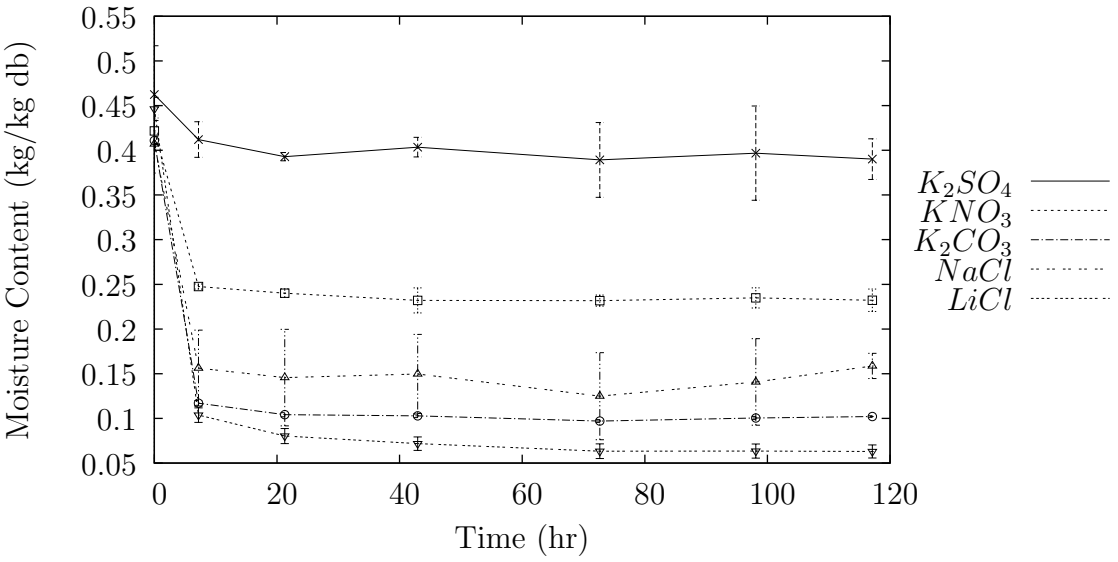

Fig. 4.1. Drying curves for samples at 40 °C. Error bars represent a 95% confidence interval

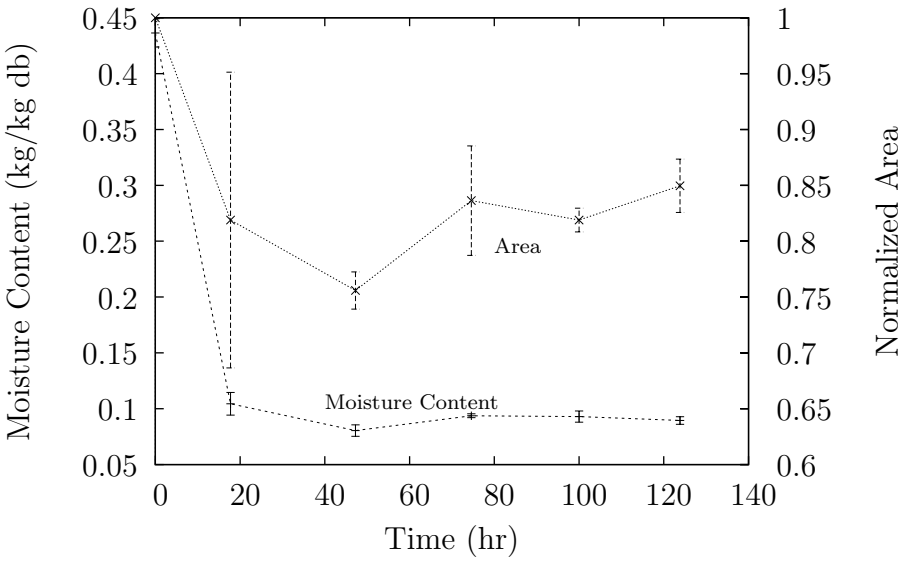

Fig. 4.2. Change in moisture content and area with time at 60 °C and 43% RH.

4.2.2 Linear Shrinkage

Several factors were found to impact the amount of shrinkage observed in the pasta samples as they were dried. The following parameters were investigated as potential explanatory variables for shrinkage: temperature, initial moisture content, final moisture content, time between measuring the mass and area of the sample and loading it into the drying chamber, and time taken to measure samples after removal from the oven. Additionally, quadratic terms for each of these parameters were considered to determine if their effects were significant. The full model (Eq. 4.1) has an R^2 value of 0.8887, and the parameters are presented in Table 4.3.

This regression analysis considered only those samples where the salt solution was still saturated when the jars were removed from the oven, and any samples that showed signs of mold growth were rejected. Outliers were determined by analysing the studentized residuals. Any residual value above 2.0 was considered to be a indicative of an outlier, and the point was rejected. In total, three points were rejected for being outliers, nine were rejected due to the salt solution drying out, five were eliminated because all of the salt dissolved, and five were eliminated for visible mold growth. Overall, 55 data points were used to construct the regression models.

$$\frac{A_f}{A_i} = \beta_0 + \beta_1 T + \beta_2 T^2 + \beta_3 X_i + \beta_4 X_i^2 + \beta_5 X_f + \beta_6 X_f^2 + \beta_7 t_i + \beta_8 t_i^2 + \beta_9 t_f + \beta_{10} t_f^2 \quad (4.1)$$

The terms where the p-values were larger than value of $\alpha = .05$ were eliminated from the regression model, and a model investigating the effects of the remaining parameters was created. Additionally, the initial and final moisture contents were combined to form a single change in moisture content parameter. This reduced model (Eq. 4.2) has an R^2 value of 0.8781. For this model

$$\sqrt{\frac{A_f}{A_i}} = \frac{L}{L_0} = \beta_0 + \beta_1 T + \beta_2 T^2 + \beta_3 (X_i - X_f) + \beta_4 (X_f - X_i)^2 + \beta_5 t_f \quad (4.2)$$

This model shows that both temperature and change in moisture content have a quadratic relationship with change in length over the intervals investigated. It was

Table 4.3.
Parameters for the full regression model for salt drying experiments. (Eq 4.1)

Parameter	β_i	95% CI		p-value
Constant	0.7233	-0.2444	1.691	0.1391
T	0.01039	0.0004731	0.02031	0.04044
T^2	-8.816×10^{-5}	-0.0001663	-1.001×10^{-5}	0.02793
X_i	-0.5452	-3.823	2.733	0.7391
X_i^2	0.2927	-3.431	4.016	0.8748
X_f	-0.002518	-0.322	0.3169	0.9874
X_f^2	1.008	0.291	1.724	0.006919
t_i	6.722×10^{-6}	-1.964×10^{-5}	3.308×10^{-5}	0.6098
t_i^2	-2.688×10^{-9}	-7.88×10^{-9}	2.505×10^{-9}	0.3025
t_f	-5.202×10^{-5}	-9.367×10^{-5}	-1.038×10^{-5}	0.01554
t_f^2	1.418×10^{-8}	-4.579×10^{-9}	3.293×10^{-8}	0.1348

Table 4.4.
Parameters for the reduced regression model for salt drying experiments. (Eq. 4.2)

Parameter	β_i	95% CI		p-value
Constant	0.8839	0.8000	0.9677	2.558×10^{-26}
T	0.004264	0.001465	0.007063	0.003568
T^2	-3.726×10^{-5}	-5.981×10^{-5}	-1.471×10^{-5}	0.001703
$X_f - X_i$	0.3704	0.2593	0.4816	1.941×10^{-7}
$(X_f - X_i)^2$	0.3149	0.07581	0.5540	0.01090
t_f	-1.001×10^{-5}	-1.501×10^{-5}	-5.020×10^{-6}	1.938×10^{-4}

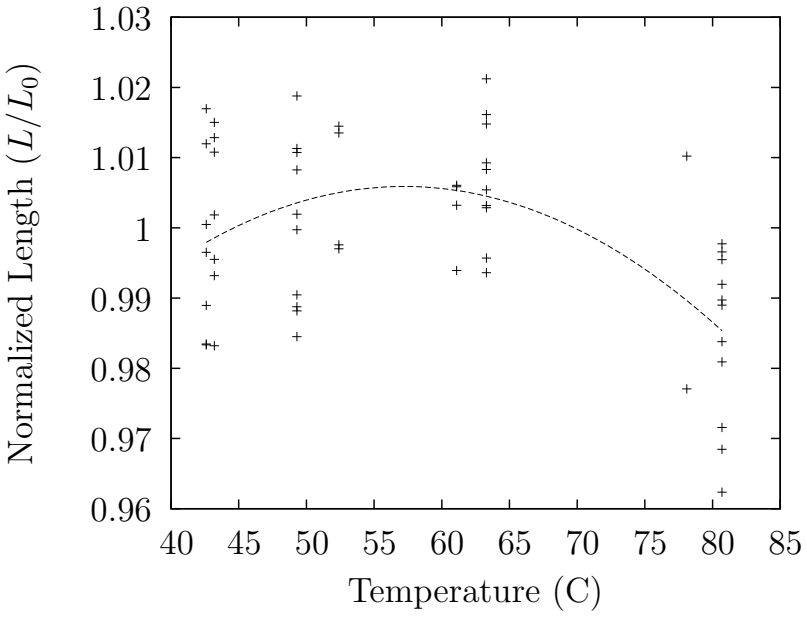

Fig. 4.3. Plot of shrinkage as a function of temperature. (T vs. $\frac{L}{L_0} - \beta_3(X_f - Xi) - \beta_4(X_f - X_i)^2 - \beta_5 t_f$)

also found that the samples quickly changed their moisture content and area when removed from a controlled environment. This is evidenced by the significance of the effect of the duration between removal of the samples from the oven and when the mass and area of the samples were measured. The effects of these parameters are detailed in Figs. 4.3, 4.4, and 4.5.

The model can be further reduced by assuming that shrinkage has only a linear relationship with temperature. Removing this term results in the p-value quadratic term for change in moisture content to rise above the cutoff of $\alpha = 0.05$, causing it to also be removed from the model. The resulting model has an R^2 value to 0.841 818. The regression model and calculated coefficients are presented in Eq. 4.3 and Table 4.5.

$$\sqrt{\frac{A_f}{A_i}} = \frac{L}{L_0} = \beta_0 + \beta_1 T + \beta_2(X_i - X_f) + \beta_3 t_f \tag{4.3}$$

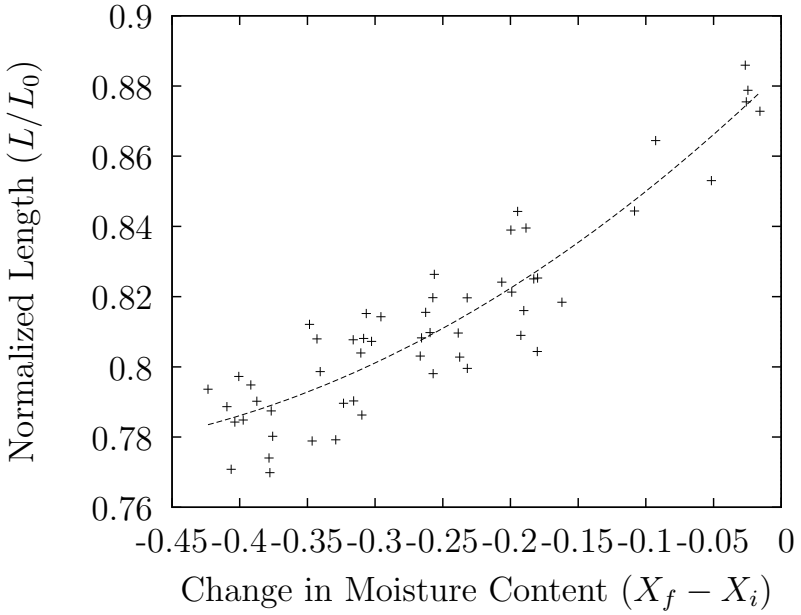

Fig. 4.4. Plot of shrinkage as a function of change in moisture content. ($X_f - X_i$ vs. $\frac{L}{L_0} - \beta_1 T - \beta_2 T^2 - \beta_5 t_f$)

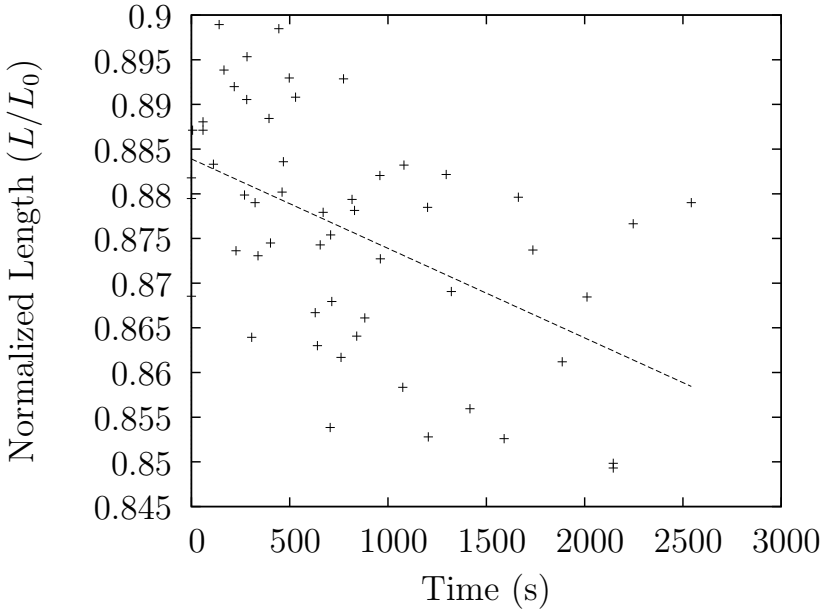

Fig. 4.5. Plot of shrinkage as a function of time between sample removal and measurement. (t_f vs. $\frac{L}{L_0} - \beta_1 T - \beta_2 T^2 - \beta_3 (X_f - X_i) - \beta_4 (X_f - X_i)^2$)

Table 4.5.
Parameters for the regression model for salt drying experiments with linear terms only. (Eq. 4.2)

Parameter	β_i	95% CI		p-value
Constant	1.011	9725	0.9910	7.526×10^{-77}
T	-3.727×10^{-4}	-0.008451	-0.001302	0.00847118
$X_f - X_i$	0.2407	0.2079	0.02734	4.965×10^{-20}
t_f	-1.080×10^{-5}	-0.01063	-0.003501	0.0002227

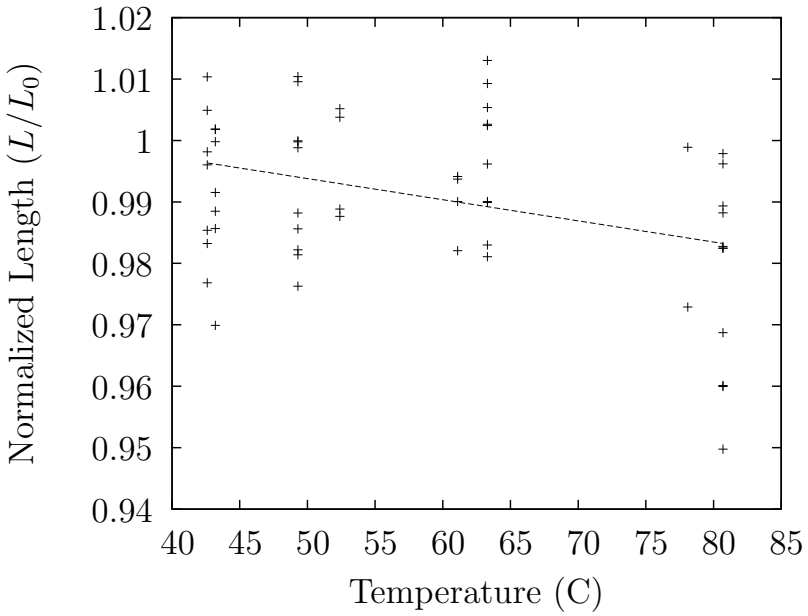

Fig. 4.6. Plot of shrinkage as a function of temperature for the linear regression model. (T vs. $\frac{L}{L_0} - \beta_2(X_f - Xi) - \beta_3 t_f$)

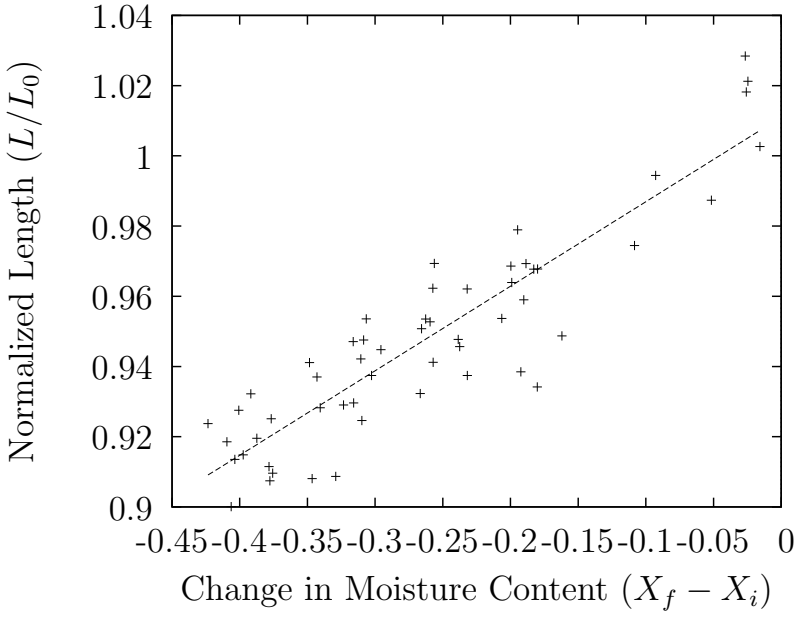

Fig. 4.7. Plot of shrinkage as a function of change in moisture content for the linear regression model. ($X_f - X_i$ vs. $\frac{L}{L_0} - \beta_1 T - \beta_3 t_f$)

For comparison, Cummings (1981) performed similar drying experiments, where he dried pasta over a salt solution and measured the initial and final volumes of the samples. The data for his experiments is presented in Table H.1. He fitted his shrinkage data to Eq. 4.4 to determine the linear shrinkage coefficients for the samples.

$$\frac{V}{V_0} = 1 + 3\beta(X_f - X_i) + 3\alpha(T - T_0) \tag{4.4}$$

He found the value of β to be 0.34 (p-value: $<$0.0001), and α to be -3.3×10^{-5} (p-value: 0.86) (Cummings, 1981). The range of temperatures he used was 42 °C to 58 °C, and the range of final moisture contents was 0.1230 $\frac{\text{kg}}{\text{kg}_{\text{db}}}$ to 0.2650 $\frac{\text{kg}}{\text{kg}_{\text{db}}}$.

4.2.3 Volumetric Shrinkage

The decrease in volume of the pasta samples can be related to the decrease in the volume of water of the samples. The decrease in the volume of the sample can be calculated directly based on the change in the measured area and the initial thickness of the slab. Assuming that shrinkage is isotropic, the following equation can be used to calculate the volume of the sample:

$$V = Ah\sqrt{\frac{A}{A_0}} \tag{4.5}$$

where A is the current area of one of the large faces of the sample, h is the initial thickness (assumed to be 1.3 mm for all samples), and A_0 is the initial area.

The current volume of water contained in the dough can be approximated from the measured mass of water in the sample and the bulk density of water at the desired temperature. Water density is calculated using the Choi-Okos equations (Choi and Okos, 1986). This method does not account for the difference in density between bulk and vicinal water, but this difference (approximately 3%) is insignificant (Etzler and Fagundus, 1987). Because water density is a function of temperature, this regression model combines both temperature and moisture effects into a single term, water volume. This causes the temperature effects to be statisticially insignificant predictors of shrinkage at a significance level of $\alpha = 0.05$.

Table 4.6.
Parameters for the volumetric shrinkage regression model for salt drying experiments. (Eq. 4.6)

Parameter	β_i	95% CI		p-value
Constant	0.1479	-0.0227	0.3186	0.0878
V_{water}	0.8017	0.6837	0.9197	1.197×10^{-18}
V_{water}^2	0.08387	0.005334	0.1624	0.036 83
t_f	-0.0002872	-0.0004349	-0.0001394	0.0002806

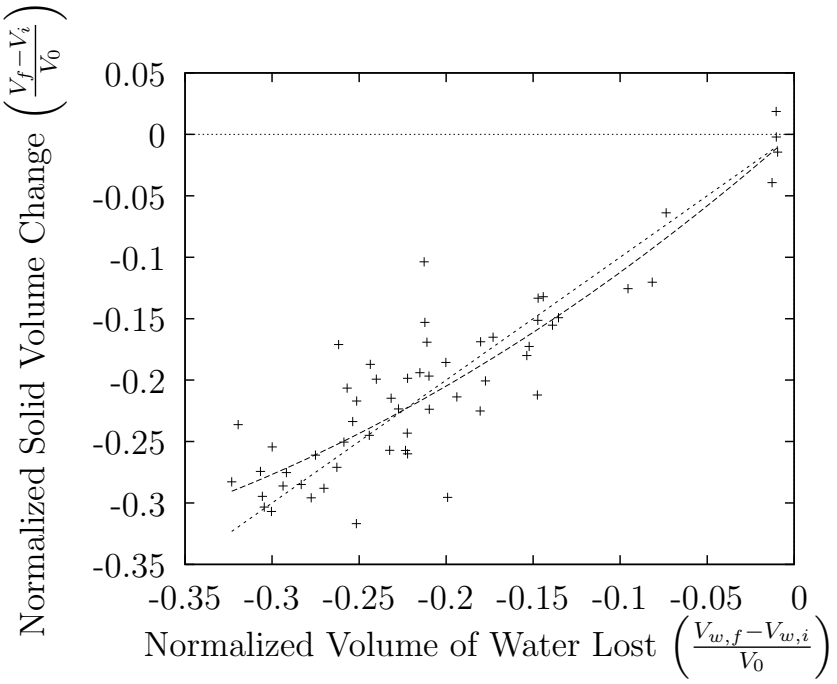

Fig. 4.8. Change in solid volume as a function of change in volume water for all temperatures. (40 °C, 50 °C, 60 °C and 80 °C)

The volume change of the sample expressed as a function of the volume change in water is represented using Eq. 4.6.

$$\frac{V_s}{V_{s0}} = \beta_0 + \beta_1 T^2 + \beta_2 \Delta V_w + \beta_3 \left(\Delta V_w\right)^2 + \beta_4 t_f \tag{4.6}$$

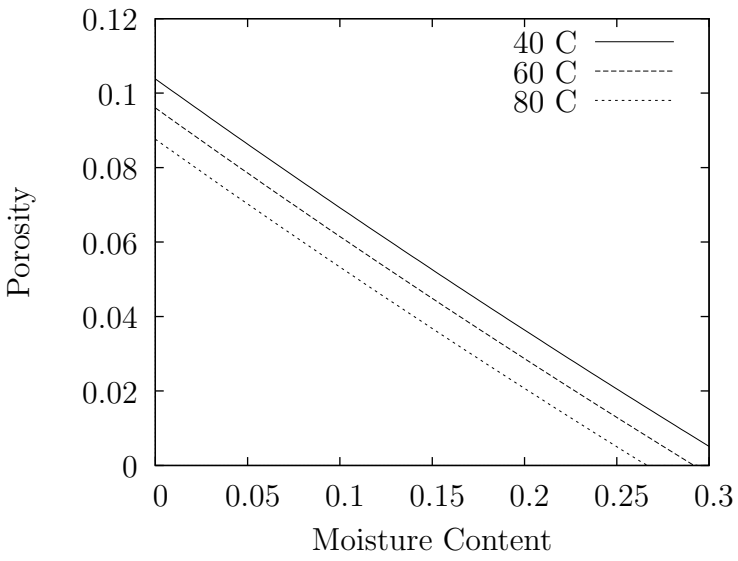

Fig. 4.9. Porosity estimated from experimental data at selected temperatures. The regression model for strain used only linear terms for temperature and change in moisture content. Initial moisture content was taken to be 0.33 $\frac{\text{kg}}{\text{kg}_{\text{db}}}$.

4.2.4 Porosity

The porosity of the samples was not measured, but it can be predicted based on the initial moisture content, final moisture content, temperature, and strain using the following equation:

$$\phi = \frac{X_0 \frac{\rho_w}{\rho_s}(\epsilon + 1) + \epsilon - X \frac{\rho_w}{\rho_s}}{X_0 \frac{\rho_w}{\rho_s}(\epsilon + 1) + \epsilon + 1}$$

The derivation for this is presented in Appendix G. The predicted porosity as a function of temperature and moisture content is presented in Fig. 4.9.

By setting porosity equal to zero and calculating the strain for that moisture content, the maximum amount of strain (without compressing the solid phase) can be calculated. This value, L_∞, was used to determine how closely the observed

Table 4.7.
Parameters for the porosity shrinkage regression model for salt drying experiments. (Eq. 4.7)

Parameter	β_i	95% CI		p-value
Constant	1.02	0.7622	1.277	1.745×10^{-10}
T	-0.003003	-0.006755	0.0007484	0.1142
X_f	-0.8138	-1.354	-0.2737	3.892×10^{-3}
t_f	-0.0001091	-0.0001898	-2.835e-05	0.009072

shrinkage was to the maximum value. A regression model was constructed as shown in Eq. 4.7.

$$\frac{L - L_\infty}{L_0 - L_\infty} = \beta_0 + \beta_1 T + \beta_2 X_f + \beta_3 t_f \tag{4.7}$$

The fitted parameters for this model are shown in Table 4.7. The p-value for temperature was found to be insignificant at a level of $\alpha = 0.05$; however, it was left in the model anyway. The overall R^2 value is rather low (0.24), but the p-value for final moisture content is significant, indicating that the samples shrunk less and had higher porosity at lower final moistures. A plot of these results is presented in Fig. 4.10.

4.2.5 Isotherm Calculation

The pressure required to obtain the experimentally determined strain curve was determined by calculating the elastic modulus of the material at equilibrium $\left(\lim_{t\to\infty} J(t)\right)$. This was used with the equation below to obtain a value for effective stress.

$$E = \frac{1}{J} = \frac{\sigma}{\epsilon}$$

The water activity corresponding to this effective stress was then calculated using Eqs. 2.24 and 5.8, with the value of ζ in Eq. 2.24 being set to 0.0612 (Xiong et al., 1992). The calculated pressure curve is shown in Figure 4.12 plotted against an set an Oswin isotherm model from Andrieu et al. (1985).

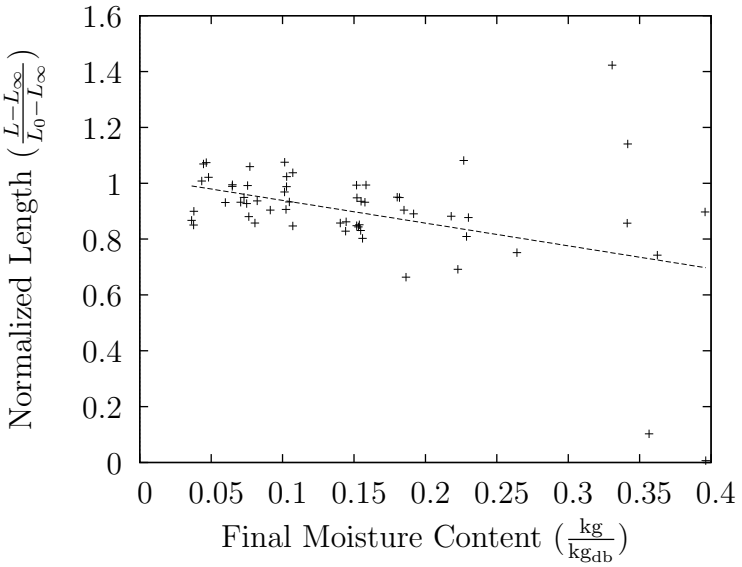

Fig. 4.10. Plot of final moisture content vs normalized change in thickness (X_f vs $\frac{L-L_\infty}{L_0-L_\infty} - \beta_1 T - \beta_3 t_f$).

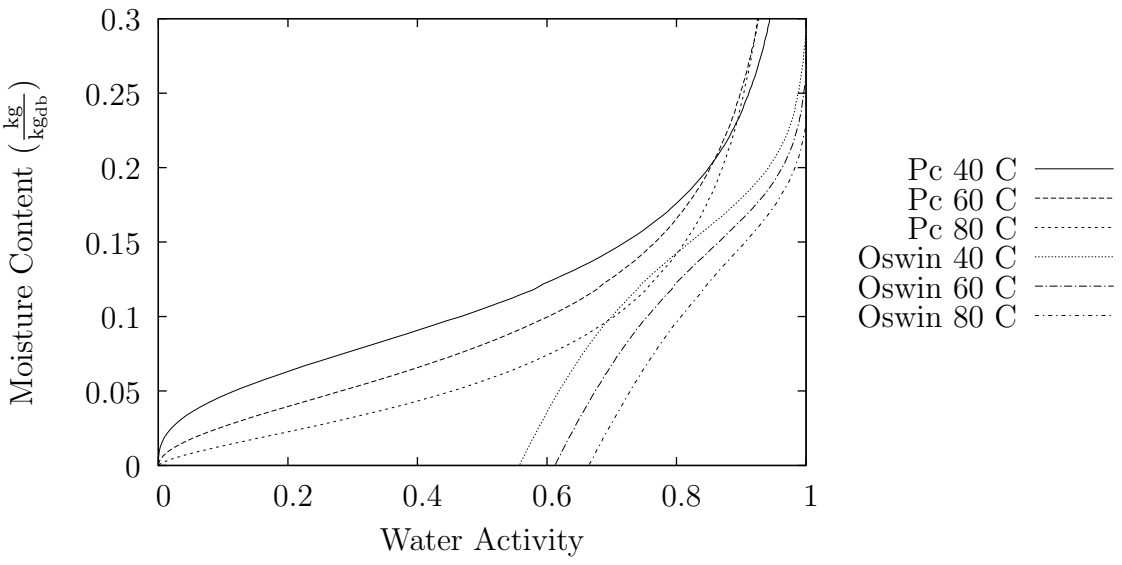

Fig. 4.11. Isotherm calculated from experimental strain measurements compared against an Oswin isotherm model from Andrieu et al. (1985).

A correction to the capillary pressure model to allow for better agreement between the water activity calculations and the model from literature. The proposed correction is shown in Eq. 4.8a, and the literature water activity model modified using this method is plotted in Fig. 4.11. The values for α and β were calculated by fitting the two isotherm models shown in Fig. 4.12 at 40 °C, 60 °C and 80 °C, and averaging each parameter.

$$P_c = \frac{RT}{V_m} \ln\left(\alpha a_w + \beta\right) \tag{4.8a}$$

$$\alpha = 0.4470 \tag{4.8b}$$

$$\beta = 0.5558 \tag{4.8c}$$

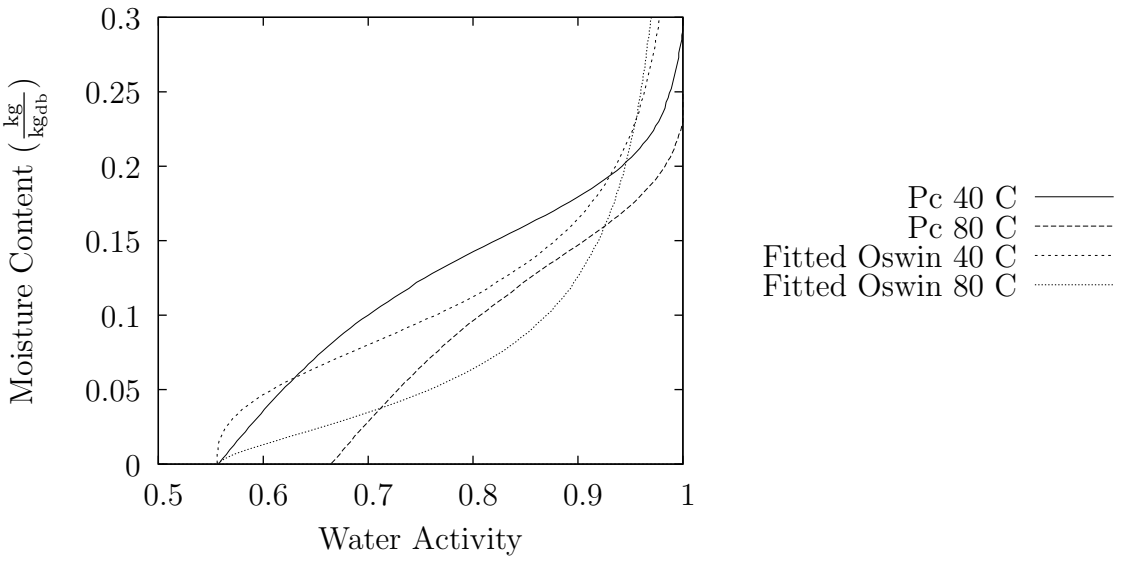

Fig. 4.12. Isotherm calculated from experimental strain measurements compared against an Oswin isotherm model from Andrieu et al. (1985) that has been modified using Eq. 4.8a.

4.3 Freeze Drying

No statistical difference was observed between the shrinkage of the pre-frozen group and the non-prefrozen group (p-value of 0.87), so they were combined for analysis purposes. The confidence interval on the average for volumetric shrinkage (V/V_0) was 0.745 30(1120). The full set of freeze drying data is presented in Table B.4.

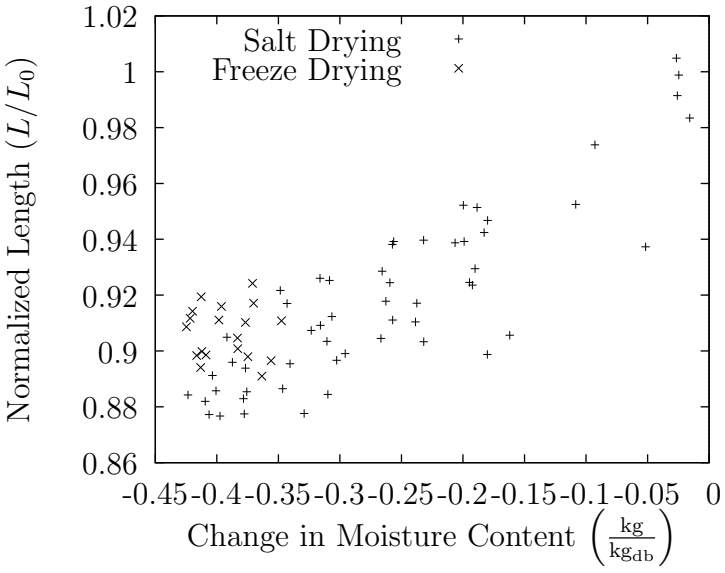

Fig. 4.13. Comparison between freeze drying and convection drying. The difference in shrinkage between the two techniques cannot be distinguished using a t-test for the same range of moisture contents.

4.4 Sources of Error

One of the primary sources of experimental error is the tendency for the pasta samples to dry between when they were removed from the oven, and when the samples were finally measured. This error was at least partially quantified in the t_f coefficient presented in tables 4.4 and 4.6. The time between when the samples were first measured and when they were loaded into the ovens was also measured, but it was determined to be statistically insignificant.

The samples did not spend the entire time between when they were loaded into and unloaded from the oven at constant drying conditions. Notably, the drying jars were removed from the oven several times during the course of the experiment to measure the mass of the samples in order to obtain drying curves. This process took approximately 20 min to 30 min each time, and the samples were massed nearly once every 24 h. Due to the time required to reestablish equilibrium for both temperature and humidity once the samples were put back into the ovens, up to 5% of the drying time could have been at conditions other than those that were prescribed.

The ovens did not maintain a constant temperature throughout the entire week that the samples were drying. There was a temperature variation of approximately 1 °C to 2 °C per day. The average drying temperature was calculated based on repeated measurements, and this is the temperature that is reported for each sample. However, this temperature variation could be responsible for some of the experimental error. Additionally, The exact location of the jars within the ovens was not recorded, and no attempt was made to ensure the jars were placed back in the same location after each measurement. It is possible that the ovens did not maintain a uniform temperature throughout the interior, and if this is the case, there could have been variation in the drying temperature for the jars within the same oven.

Finally, the fans used to increase the rate of convective mass transfer inside the drying jars were all the same model and were attached to the same power supply, but the individual motors likely did not run at the same speeds, and variations in

the voltage from the power supply would also change the fan speed. This should not have a significant impact on drying because the rate was limited primarily by internal mass transfer resistance.

The amount of shrinkage was measured by optically determining the area of the sample with a camera. This method has two minor problems. First of all, only two of the three axes were measured. Because the extruded pasta is a biological material, the potential for non-isotropic shrinkage exists. The change in sample thickness was approximated to be proportional to the square root of the change in sample area, but this relationship was not experimentally validated. The second issue is that the pasta samples warped as they dried, causing the final shape to resemble a shallow bowl more than a flat slab. This served to slightly decrease the area observed by the camera.

Additionally, the thickness of the sheet of pasta emerging from the extruder was not completely uniform. Because the sheet was allowed to hang freely from the end of the die, the sheet stretched slightly under its own weight. This resulted in some sections of the sheet being thicker than others, and this may have impacted the drying rate of the samples.

5. MODEL OUTLINE

5.1 Assumptions

Several key assumptions were made to simplify the problem. These are listed below:

- The slab is thin enough that it only dries from the top and bottom (1-dimensional)
- The drying rate is the same for the top and bottom of the slab (symmetric)
- The sample rapidly reaches thermal equilibrium at the drying temperature (isothermal)
- Internal mass transfer is rate-limiting ($Bi = \infty$)
- Deformations due to shrinkage are small (infinitesimal strain)
- Mass transfer of moisture occurs only by diffusion
- The pores in the sample are initially filled with water

5.2 Composition

In order to calculate the density of the slab at various temperatures and moisture contents, the Choi-Okos equations were used (Choi and Okos, 1986). These equations are a set of empirical relations used to determine density, thermal conductivity, and heat capacity of foods as a function of their composition, and temperature. The composition is supplied as mass fractions of protein, fat, carbohydrate, fiber, ash, water, and ice. The density of each component is calculated using Eqs. 5.1. In order to calculate the density of the whole product, the density of the components

is averaged according to Eq. 5.2. The composition data was taken from Cummings et al. (1993), and is presented in Table 2.5.

$$\rho_{pro} = 1.3299 \times 10^3 - 5.1840 \times 10^{-1} T \tag{5.1a}$$

$$\rho_{fat} = 9.2559 \times 10^2 - 4.1757 \times 10^{-1} T \tag{5.1b}$$

$$\rho_{car} = 1.5991 \times 10^3 - 3.1046 \times 10^{-1} T \tag{5.1c}$$

$$\rho_{fib} = 1.3115 \times 10^3 - 3.6589 \times 10^{-1} T \tag{5.1d}$$

$$\rho_{ash} = 2.4238 \times 10^3 - 2.8063 \times 10^{-1} T \tag{5.1e}$$

$$\rho_{wat} = 997.18 + 3.1439 \times 10^{-3} T - 3.7574 \times 10^{-3} T^2 \tag{5.1f}$$

$$\rho_{ice} = 916.89 - 1.3071 \times 10^{-1} T \tag{5.1g}$$

$$\frac{1}{\rho} = \sum_i \frac{M_i}{\rho_i} \tag{5.2}$$

These equations are used to calculate both the density of water and the density of dry pasta as a function of temperature. Additionally, they are used to calculate the initial density of the moist product; however, once the sample begins to dry, Eq. 5.2 and Eq. 5.1 cannot be used due to the presence of pores.

5.3 Isotherm

The Oswin isotherm model was used to relate moisture content to water activity where needed in the other equations in the model.

$$X_{db} = (k_0 + k_1 T) \left(\frac{a_w}{1 - a_w} \right)^{(n_0 + n_1 T)}$$

The parameters for this equation come from Xiong et al. (1992), and is presented along with other sets of parameters for the Oswin isotherm in Table 5.1. The equation is plotted in Figs. 5.1 and 5.2.

Table 5.1.
Oswin isotherm parameters for extruded durum semolina (Xiong et al., 1992).

k_0	k_1	n_0	n_1
0.176	-1.748×10^{-3}	0.182	6.946×10^{-3}

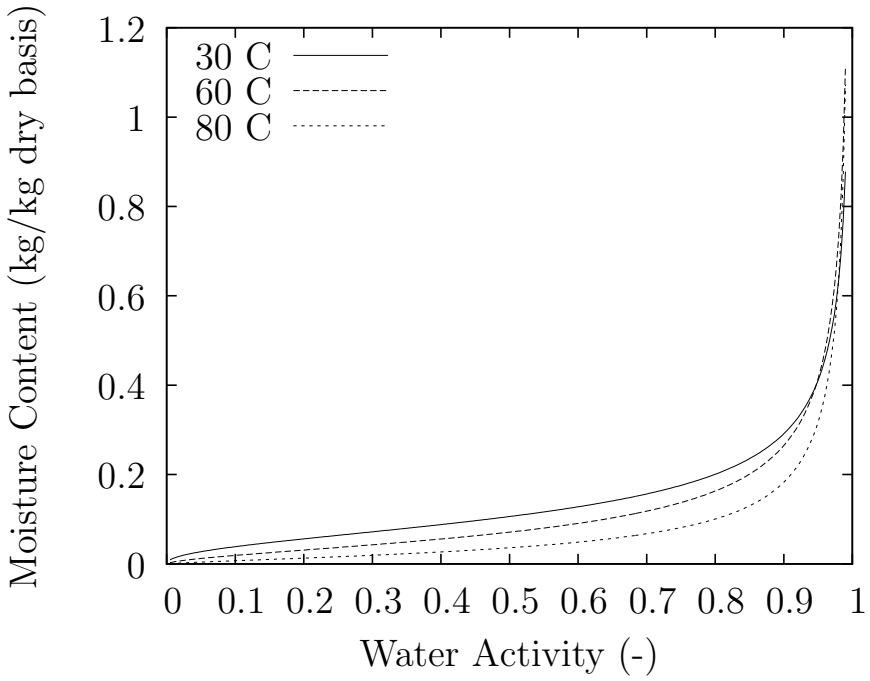

Fig. 5.1. Isotherm data for durum semolina plotted as a function of water activity (Xiong et al., 1992)

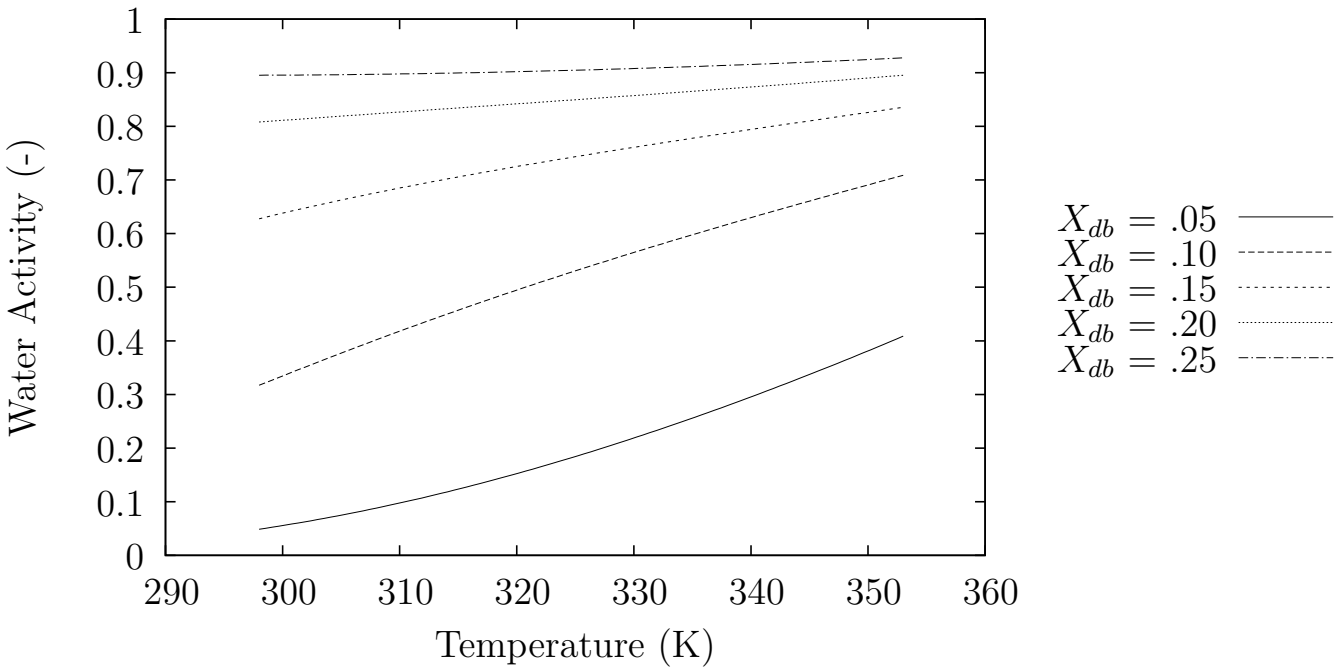

Fig. 5.2. Isotherm data for durum semolina plotted as a function of temperature (Xiong et al., 1992)

5.4 Diffusivity

In order to calculate effective diffusivity as a function of temperature and moisture, the semi-empirical equation from Xiong et al. (1992) is employed. This equation calculates diffusivity based on the self diffusivity of water ($D_{self} = D_0 \exp \frac{-E_a}{RT}$, the binding energy of water, and a binding rate constant, K.

$$D_{eff} = D_0 e^{\frac{-E_a}{RT}} \frac{K e^{\frac{-E_b}{RT}}}{1 + K e^{\frac{-E_b}{RT}}} \tag{5.3}$$

Here, $D_0 = 6.3910 \times 10^{-8} \frac{\mathrm{m}^2}{\mathrm{s}}$, $E_a = 21\,760 \frac{\mathrm{J}}{\mathrm{mol}}$ (Xiong et al., 1992), $K = 1032.558$ (Xiong et al., 1992), and R is the gas constant.

For comparison, Eq. 2.71 is plotted as well. This equation was also used for the numerical simulation to show the impact of effective diffusivity on the magnitude of observed shrinkage.

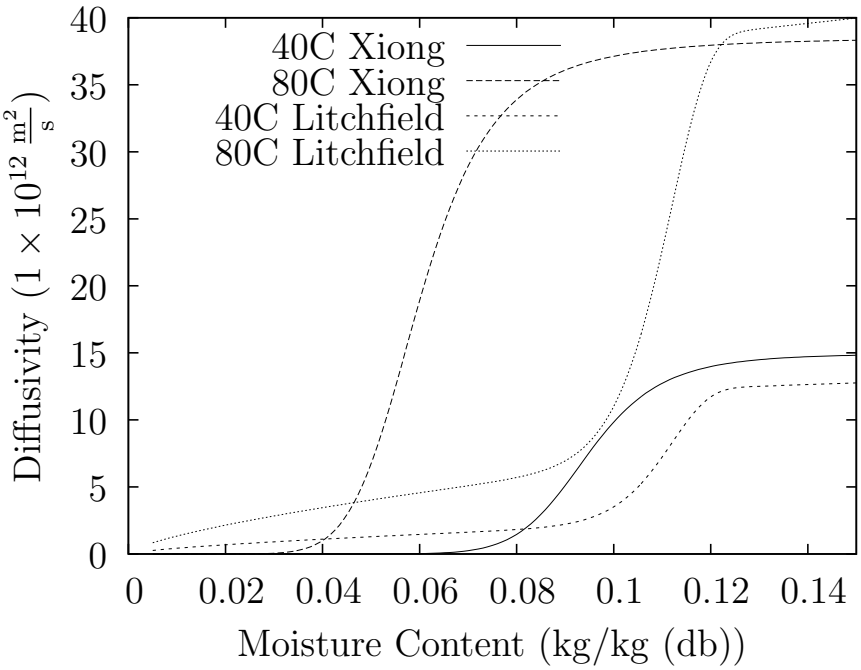

Fig. 5.3. Eq. 5.3 and Eq. 2.71 plotted at 40 °C and 80 °C (Litchfield and Okos, 1992; Xiong et al., 1992).

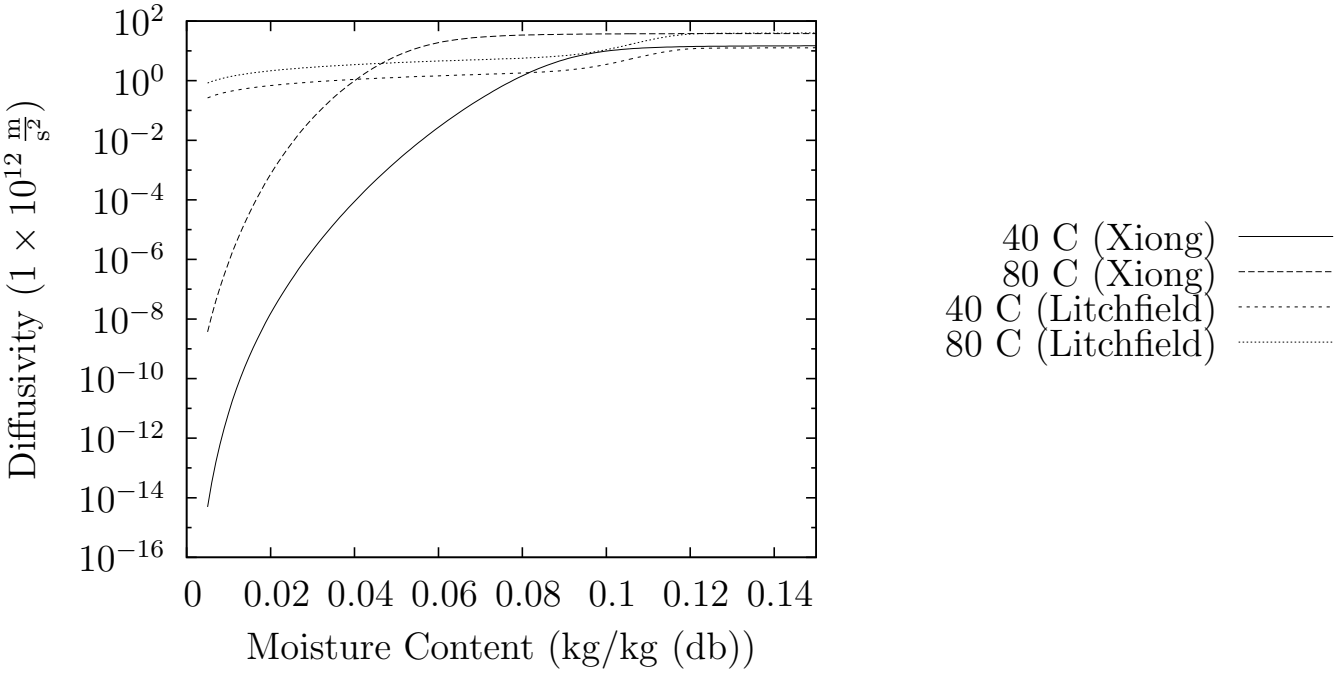

Fig. 5.4. Effective diffusivity plotted on a semi-log scale (Oswin isotherm) (Litchfield and Okos, 1992; Xiong et al., 1992)

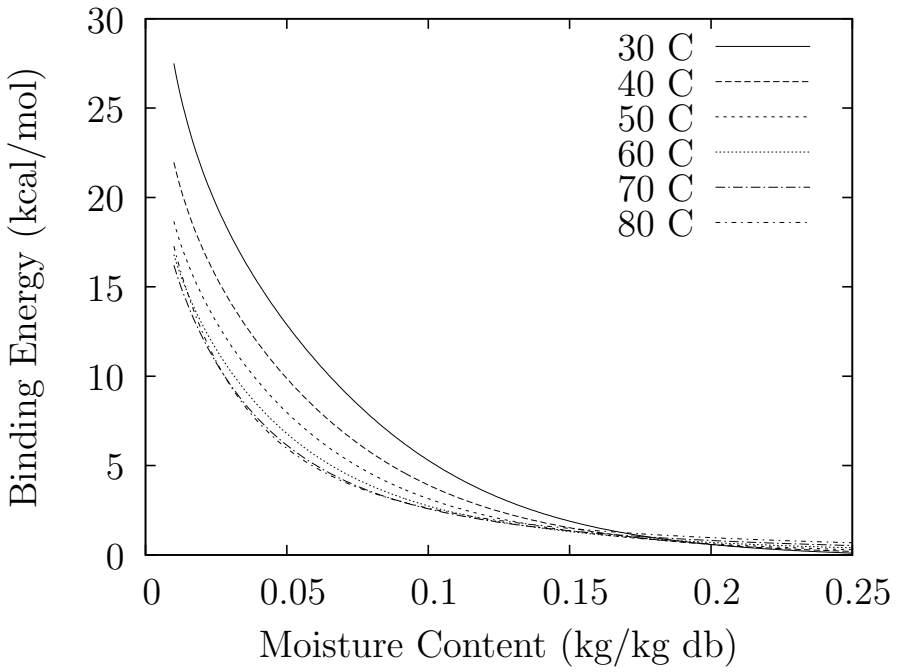

Fig. 5.5. Binding energy (Oswin isotherm) (Xiong et al., 1992)

Binding energy is calculated using the Clasius-Clapeyron equation. Water activity is calculated by using the Oswin isotherm equation (Eq 2.5).

$$\left[\frac{\partial \ln a_w}{\partial T}\right]_{P,X\,db} = -\frac{E_b}{T^2} \tag{5.4}$$

5.5 Fick's Law

In order to describe mass transport, the advection-diffusion in Lagrangian coordinates is used (Thiffeault, 2003).

$$\frac{\partial c}{\partial t} + \underline{v} \cdot \nabla c = \frac{1}{\rho}\nabla \cdot (\rho D \cdot \nabla c) \tag{5.5}$$

For the case of constant density, zero velocity, and constant diffusivity, this equation simplifies to the normal Fick's law equation.

$$\frac{\partial c}{\partial t} = D\nabla^2 c \tag{5.6}$$

The effective diffusivity is calculated using Eq 5.3 to account for the decrease in diffusivity near the end of the drying process. Density is calculated using Eq. 5.7 and Eq. 5.1.

$$\rho = (1 - \phi)\rho_{co} \tag{5.7}$$

5.6 Stress

The driving force for deformation of the pasta slab is moisture stress (Brinker and Scherer, 1990). Here, R is the gas constant, T is the absolute temperature, M_w is the molar volume of water.

$$P_c = -\frac{\rho_w RT}{V_w} \ln a_w \tag{5.8}$$

Because the solid is initially at equilibrium, the net force acting exerted by the change in moisture is calculated by subtracting the stress at the initial moisture content.

$$P = \psi(X) - \psi(X_0) \tag{5.9}$$

Only a portion of the stress generated by the water in the pores is felt by the solid matrix. The effective stress experienced by the solid is calculated using Eq. 2.24.

$$\langle \sigma_{ij} \rangle = \sigma_{ij} - \zeta P_c \delta_{ij}$$

where the parameter ζ is taken to be equal to the 0.0612, which was the final porosity measured by Xiong et al. (1992) (Garg and Nur, 1973). The externally applied force is equal to σ_{ij}. Here, the sample is under no external load, so σ_{ij} can be set equal to zero.

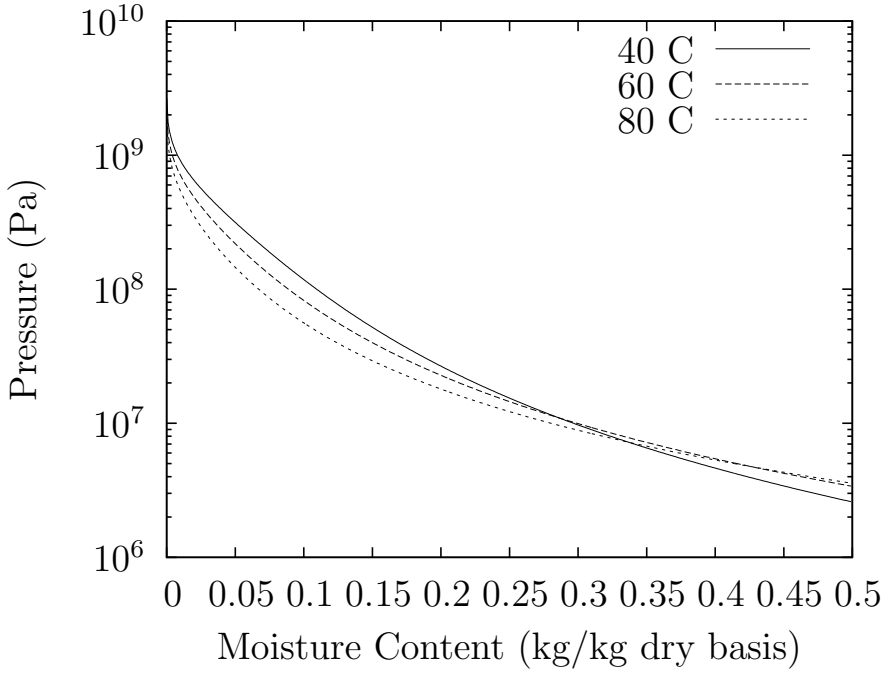

Fig. 5.6. Capillary pressure calculated using Eq. 2.24 and Oswin isotherm data from Bressani (2014).

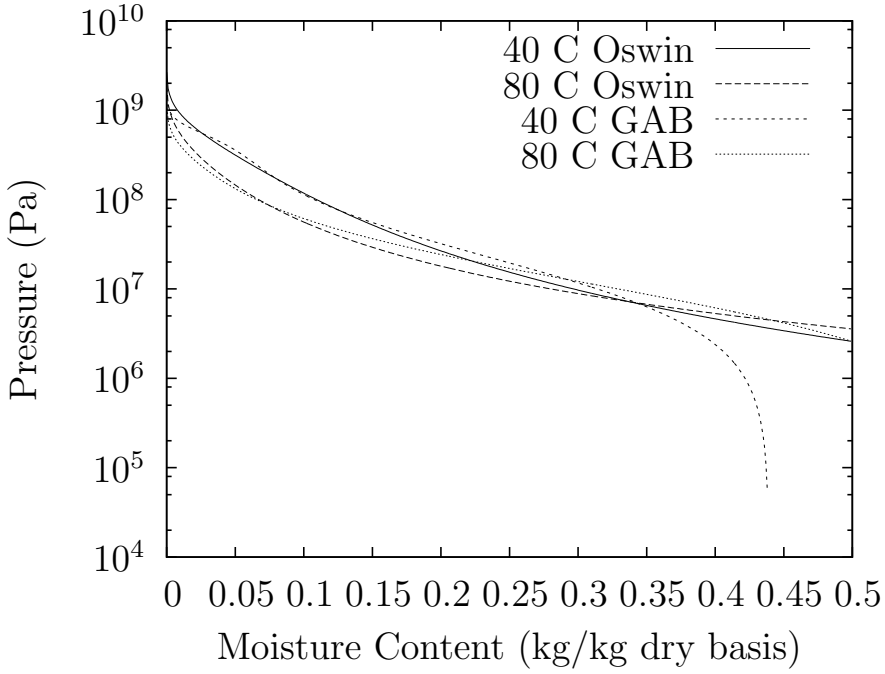

Fig. 5.7. Capillary pressure calculated using Eq. 2.24 and Oswin isotherm data from Bressani (2014) compared against pressure calculated using the GAB isotherm with data from Andrieu et al. (1985).

5.7 Viscoelasticity

Since the slab is made of a viscoelastic material, its time-dependent response to an applied stress can be described using the generalized Maxwell model.

$$G(t) = E_a + \sum_{i=0}^{N} E_i \exp \frac{-t}{\lambda_i} \tag{5.10}$$

Two Maxwell elements were used to describe the solid, and the model is shown in Fig. 5.11(a). The stiffness of the elastic elements are dependent on both temperature and moisture content, but the relaxation times are considered to be constant. The values of the these parameters are given by Eq 5.11 and plotted in Figs. 5.8, 5.9, and 5.10 (Rozzi, 2002).

$$E_a(M,T) = 68.18 \left(\left(1 + \exp \left\{ \frac{M - 250.92 \exp(-0.0091T)}{2.19} \right\} \right)^{-1} + 0.078 \right) \tag{5.11a}$$

$$E_1(M,T) = 20.26 \exp \left\{ -0.0802(M + 0.0474T - 14.283) \right\} \tag{5.11b}$$

$$E_2(M) = 2.484 + \frac{6.576}{1 + \exp\{\frac{M-19.36}{0.848}\}} \tag{5.11c}$$

$$\lambda_1 = 7\,\mathrm{s} \tag{5.11d}$$

$$\lambda_2 = 110\,\mathrm{s} \tag{5.11e}$$

In order to convert the relaxation function into a creep function, an inverse Laplace transform is applied according to Ferry (1980).

$$J(t) = \mathcal{L}^{-1} \left\{ \frac{1}{s^2 \hat{G}(s)} \right\} \tag{5.12}$$

This equation is evaluated numerically using the Euler inversion algorithm, and the resulting plots of the creep compliance parameters are presented in Figs. E.8, E.9, E.10, E.11, and E.12. This conversion changes the model from a generalized Maxwell model to a generalized Kelvin model. A diagram for this is presented in Fig. 5.11(b).

Since the stress generated during dessication induces a volumetric change, the bulk compliance is the appropriate viscoelastic modulus to use to describe the deformation

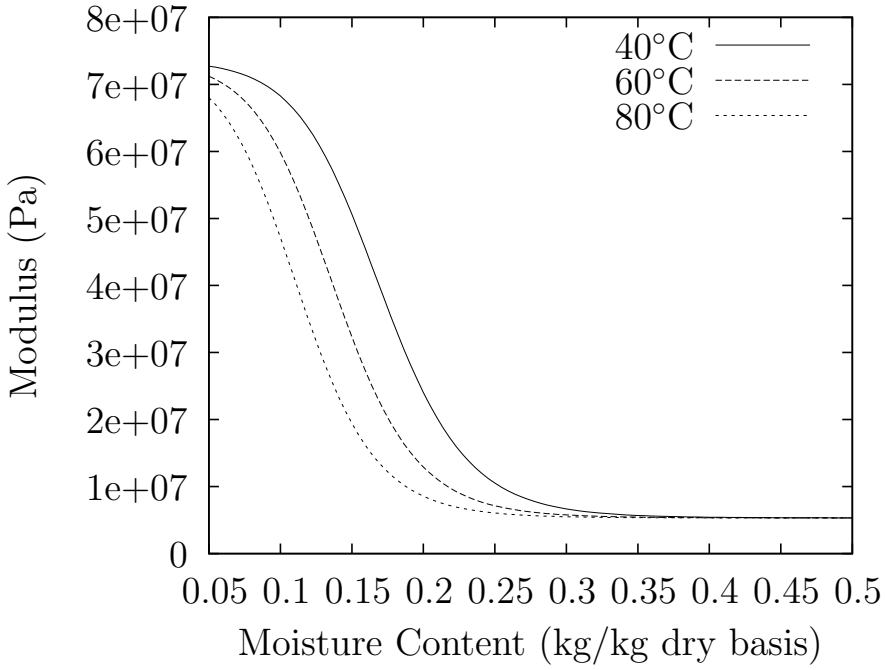

Fig. 5.8. Stress relaxation (E_a) (Rozzi, 2002)

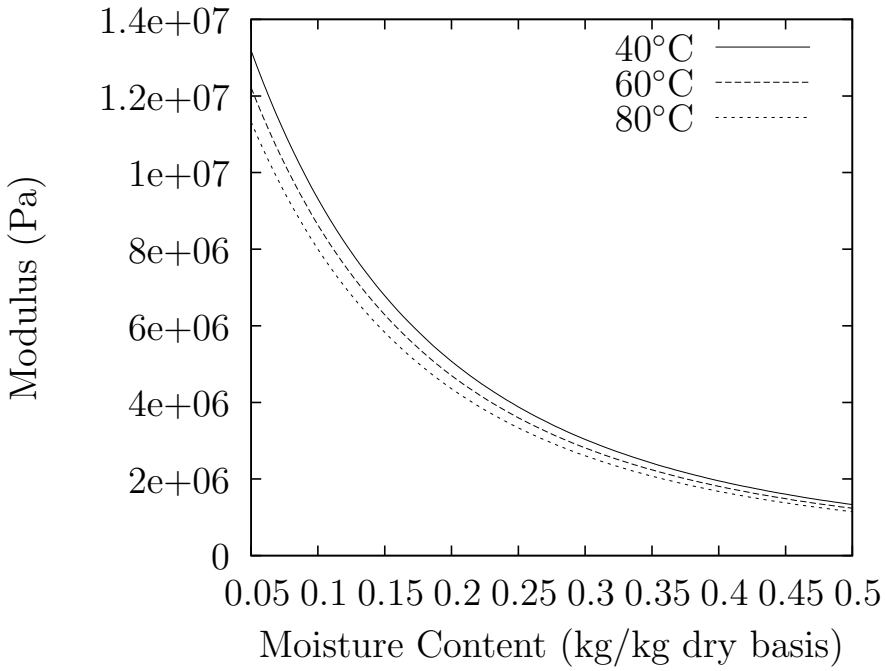

Fig. 5.9. Stress relaxation (E_1) (Rozzi, 2002)

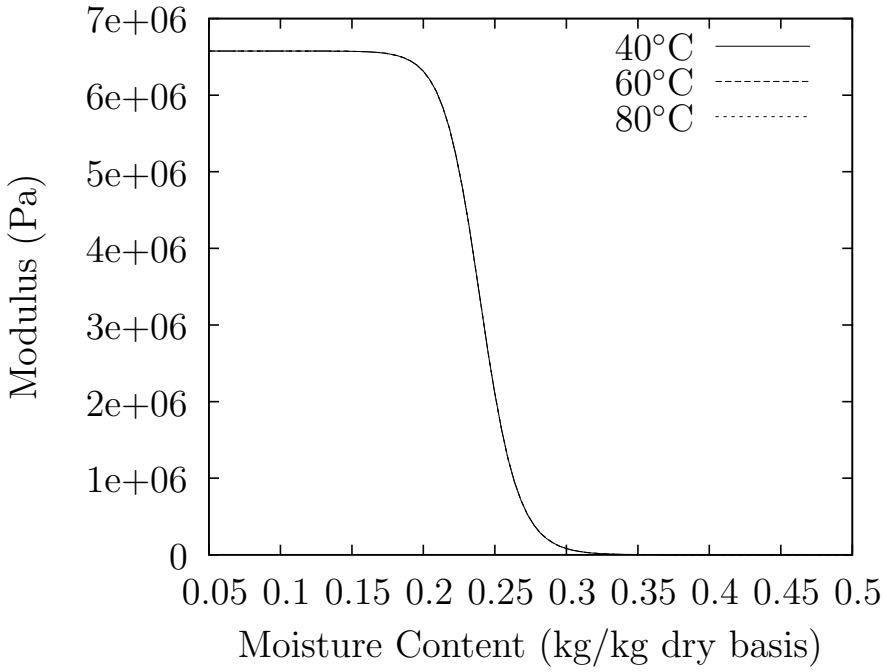

Fig. 5.10. Stress relaxation (E_2) (Rozzi, 2002)

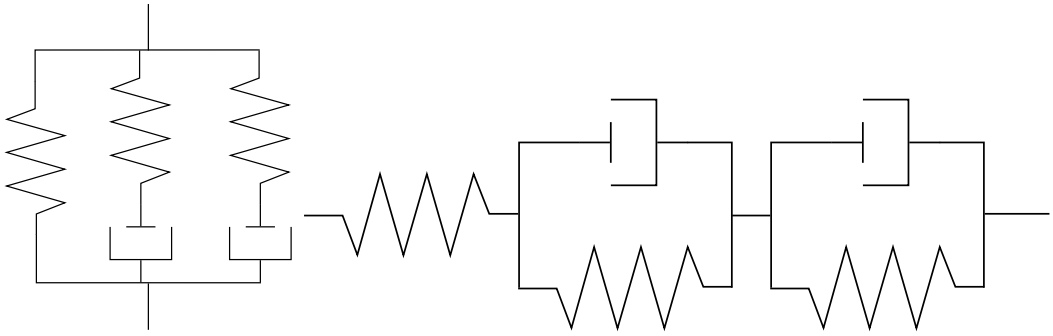

(a) Generalized Maxwell model

(b) Generalized Kelvin model

Fig. 5.11. Spring and dashpot diagrams for both the generalized Maxwell and Kelvin models.

of the slab. To convert between creep compliance and bulk compliance, an equation from Bažant (1975) is used.

$$J^V(t,t') = 6\left(\frac{1}{2} - \nu\right) J(t,t') \tag{5.13}$$

The value of the Poisson ratio is taken to be 0.37.

This set of equations from Zienkiewicz et al. (2014) is used to calculate strain by using this system of equations:

$$\epsilon = J_0\sigma + \sum_{m=1}^{M} J_m r^{(m)} \tag{5.14a}$$

$$\sigma = \frac{\partial}{\partial t} r^{(m)} + \frac{1}{\tau_m} r^{(m)} \tag{5.14b}$$

A set of creep compliance parameters at multiple moisture contents was generated for a single temperature and these values were interpolated to incorporate the moisture content dependence of each parameter. The $r^{(m)}$ variables describe the partial strains of the individual Kelvin elements shown in Fig. 5.11(b).

5.8 Kinematics

Displacement is calculated from the deformation gradient. Deformation gradient tensor is defined to be

$$F_{jK} = \frac{\partial x_j}{\partial X_K} \tag{5.15}$$

where $\underline{x}$ is the location of a point in the deformed coordinate system, and $\underline{X}$ is the same point in the undeformed, reference coordinate system. Displacement is given by Eq. 5.16, which can be simplified to Eq. 5.17 for a one-dimensional case.

$$\nabla \underline{u} = \underline{\underline{F}} - \underline{\underline{I}} \tag{5.16}$$

$$\frac{\partial u}{\partial x} = \epsilon - 1 \tag{5.17}$$

5.9 Finite Element Formulation

5.9.1 Weak Form

The diffusivity equation converted into weak form for use in the finite element solver is presented in Eq. 5.18. The first term represents the change in moisture content at a single point with time. The second and third terms are the chain rule expansion of the $\nabla \cdot (D\nabla c)$ term in Eq. 5.5. The final term allows for imposition of Neumann boundary conditions, and was obtained through integration by parts.

$$\begin{aligned} R_i^c = &\int_0^L \left\{ c_i \frac{1}{\rho}\frac{\partial \rho}{\partial x} D \frac{\partial \phi_i}{\partial x}\phi_j + c_i \frac{\partial D}{\partial x}\frac{\partial \phi_i}{\partial x}\phi_j + c_i D \frac{\partial \phi_i}{\partial x}\frac{\partial \phi_j}{\partial x} - \frac{\partial c_i}{\partial t}\phi_i\phi_j - c_i \frac{\partial u_i}{\partial t}\phi_i \frac{\partial \phi_i}{\partial x}\phi_j \right\} dx \\ &- \left[D\frac{\partial c}{\partial x} \right]_0^L \\ &= 0 \end{aligned} \tag{5.18}$$

Strain is calculating using Eqs. 5.19a and 5.19b. Here, ϵ represents the total strain, and the $r^{(m)}$ variables are the partial strains for the first and second Kelvin-Voigt elements.

$$R_i^T = \int_0^L \left\{ J_0\sigma + \sum_{m=1}^{M} J_m r_i^{(m)}\phi_i - \epsilon_i\phi_i \right\} \phi_j dx = 0 \tag{5.19a}$$

$$R_i^{P_m} = \int_0^L \left\{ \frac{\partial r_i^{(m)}}{\partial t}\phi_i + \frac{1}{\tau_m} r_i^{(m)}\phi_i - \sigma \right\} \phi_j dx = 0 \tag{5.19b}$$

Strain is integrated using Eq. 5.20 to calculate displacement. The value of $u(x = L)$ is equal to the normalized thickness change of the slab overall $(1 - L/L_0)$.

$$R_i^u = u_i \frac{\partial \phi_i}{\partial x}\phi_j - \epsilon_i\phi_i\phi_j \tag{5.20}$$

Stress is calculated using Eq 2.24 and Eq 2.23, where the initial stress was defined to be zero as follows:

$$\sigma(x, 0) = P_c(X, T) - P_c(X_0, T_0)$$

This accounted for the sample being at equilibrium initially. The derivations for all of the weak for equations are presented in Appendix G.1.

5.9.2 Boundary Conditions

The boundary conditions imposed on Eq. 5.18 are:

$$\left.\frac{\partial c(x,t)}{\partial x}\right|_{x=0} = 0 \tag{5.21a}$$

$$c(L,t) = c_A \tag{5.21b}$$

The symmetry boundary condition at the center of the slab is considered by using Eq. 5.21a, and Eq. 5.21b imposes the boundary condition at the surface. For a non-infinite Biot number, this equation would instead be $\left.\frac{\partial c(x,t)}{\partial x}\right|_{x=L} = Bi\Delta c$.

The displacement boundary condition is given by Eq. 5.22. This ensures that the center of the slab is always considered to be stationary.

$$u(0,t) = 0 \tag{5.22}$$

5.9.3 Initial Conditions

The initial conditions for each of the dependent variables is defined as follow:

$$c(x,0) = c_0 \tag{5.23a}$$

$$\epsilon(x,0) = 0 \tag{5.23b}$$

$$r_i^{(1)}(x,0) = 0 \tag{5.23c}$$

$$r_i^{(2)}(x,0) = 0 \tag{5.23d}$$

$$u(x,0) = 0 \tag{5.23e}$$

$$\sigma(x,0) = 0 \tag{5.23f}$$

5.10 Solution Method

5.10.1 Domain

The half thickness for the slab is defined to be $1 \times 10^{-3}\,\mathrm{m}$, for an overall slab thickness of 2 mm. The one-dimensional domain is divided into twenty linear elements

using the shape functions presented in Eq. 5.24 (in local coordinates). The spacing between the nodes in the mesh was set to be uniform. For all cases, the simulation was run from t=0 h to t=20 h.

$$\phi_1(\xi) = 1 - \xi, \qquad 0 < \xi < 1 \tag{5.24a}$$

$$\phi_2(\xi) = \xi, \qquad 0 < \xi < 1 \tag{5.24b}$$

5.10.2 Matrix Assembly

The equations in Section 5.9.1 are differentiated with respect to each dependent variable, and the per-element matrix equations are assembled as follows:

$$\underline{\underline{M}} = \begin{bmatrix} \frac{\partial R_i^c}{\partial c_i} & \frac{\partial R_i^c}{\partial \epsilon_i} & \frac{\partial R_i^c}{\partial r_i^{(1)}} & \frac{\partial R_i^c}{\partial r_i^{(2)}} & \frac{\partial R_i^c}{\partial u_i} \\ \frac{\partial R_i^T}{\partial c_i} & \frac{\partial R_i^T}{\partial \epsilon_i} & \frac{\partial R_i^T}{\partial r_i^{(1)}} & \frac{\partial R_i^T}{\partial r_i^{(2)}} & \frac{\partial R_i^T}{\partial u_i} \\ \frac{\partial R_i^{P_1}}{\partial c_i} & \frac{\partial R_i^{P_1}}{\partial \epsilon_i} & \frac{\partial R_i^{P_1}}{\partial r_{(1)}^i} & \frac{\partial R_i^{P_1}}{\partial r_{(2)}^i} & \frac{\partial R_i^{P_1}}{\partial u_i} \\ \frac{\partial R_i^{P_2}}{\partial c_i} & \frac{\partial R_i^{P_2}}{\partial \epsilon_i} & \frac{\partial R_i^{P_2}}{\partial r_{(1)}^i} & \frac{\partial R_i^{P_2}}{\partial r_{(2)}^i} & \frac{\partial R_i^{P_2}}{\partial u_i} \\ \frac{\partial R_i^u}{\partial c_i} & \frac{\partial R_i^u}{\partial \epsilon_i} & \frac{\partial R_i^u}{\partial r_{(1)}^i} & \frac{\partial R_i^u}{\partial r_{(2)}^i} & \frac{\partial R_i^u}{\partial u_i} \\ \frac{\partial R_i^s}{\partial c_i} & \frac{\partial R_i^s}{\partial \epsilon_i} & \frac{\partial R_i^s}{\partial r_{(1)}^i} & \frac{\partial R_i^s}{\partial r_{(2)}^i} & \frac{\partial R_i^s}{\partial u_i} \end{bmatrix} \tag{5.25}$$

$$\underline{\underline{N}} = \begin{bmatrix} \frac{\partial R_i^c}{\partial \dot{c}_i} & \frac{\partial R_i^c}{\partial \dot{\epsilon}_i} & \frac{\partial R_i^c}{\partial r_i^{(1)}} & \frac{\partial R_i^c}{\partial r_i^{(2)}} & \frac{\partial R_i^c}{\partial \dot{u}_i} \\ \frac{\partial R_i^T}{\partial \dot{c}_i} & \frac{\partial R_i^T}{\partial \dot{\epsilon}_i} & \frac{\partial R_i^T}{\partial r_i^{(1)}} & \frac{\partial R_i^T}{\partial r_i^{(2)}} & \frac{\partial R_i^T}{\partial \dot{u}_i} \\ \frac{\partial R_i^{P_1}}{\partial \dot{c}_i} & \frac{\partial R_i^{P_1}}{\partial \dot{\epsilon}_i} & \frac{\partial R_i^{P_1}}{\partial r_{(1)}^i} & \frac{\partial R_i^{P_1}}{\partial r_{(2)}^i} & \frac{\partial R_i^{P_1}}{\partial \dot{u}_i} \\ \frac{\partial R_i^{P_2}}{\partial \dot{c}_i} & \frac{\partial R_i^{P_2}}{\partial \dot{\epsilon}_i} & \frac{\partial R_i^{P_2}}{\partial r_{(1)}^i} & \frac{\partial R_i^{P_2}}{\partial r_{(2)}^i} & \frac{\partial R_i^{P_2}}{\partial \dot{u}_i} \\ \frac{\partial R_i^u}{\partial \dot{c}_i} & \frac{\partial R_i^u}{\partial \dot{\epsilon}_i} & \frac{\partial R_i^u}{\partial r_{(1)}^i} & \frac{\partial R_i^u}{\partial r_{(2)}^i} & \frac{\partial R_i^u}{\partial \dot{u}_i} \\ \frac{\partial R_i^s}{\partial \dot{c}_i} & \frac{\partial R_i^s}{\partial \dot{\epsilon}_i} & \frac{\partial R_i^s}{\partial r_{(1)}^i} & \frac{\partial R_i^s}{\partial r_{(2)}^i} & \frac{\partial R_i^s}{\partial \dot{u}_i} \end{bmatrix} \tag{5.26}$$

$$\underline{u}^T = \begin{bmatrix} c_i & \epsilon_i & r_i^{(1)} & r_i^{(2)} & u_i \end{bmatrix} \tag{5.27}$$

This yields a per-element equation of

$$\underline{\underline{M}} \cdot \underline{u} + \underline{\underline{N}} \cdot \dot{\underline{u}} = \underline{B} \tag{5.28}$$

where $\underline{B}$ is the load vector.

The per-element equations were integrated using 3-point Gaussian quadrature. The formula, weights, and Gauss points used are given in Eq. 5.29. After integration, the equations are combined into a single global matrix equation for the entire domain, and the boundary conditions are imposed as needed. The final equation has the same form as Eq. 5.28.

$$\int_{-1}^{1} f(x)dx = \sum_{i=1}^{n} w_i f(x_i) \tag{5.29a}$$

$$\underline{x} = \begin{bmatrix} -0.774\,596\,669\,241\,483 \\ 0.0 \\ 0.774\,596\,669\,241\,483 \end{bmatrix} \tag{5.29b}$$

$$\underline{w} = \begin{bmatrix} 0.555\,555\,555\,555\,555 \\ 0.888\,888\,888\,888\,888 \\ 0.555\,555\,555\,555\,555 \end{bmatrix} \tag{5.29c}$$

5.10.3 Matrix Solver

The global matrix equation solved at each time step using an implicit, nonlinear solver, and time integration is handled using a backward difference integration scheme. The Jacobian matrix is calculated using Eq. 5.30 and the residual matrix from Eq. 5.31.

$$\underline{\underline{J}} = \frac{1}{\Delta t}\underline{\underline{N}}(\underline{u_{i+1}}) + \underline{\underline{M}}(\underline{u_{i+1}}) \tag{5.30}$$

$$\underline{\underline{R}} = \frac{1}{\Delta t}\underline{\underline{N}}(\underline{u_{i+1}}) \cdot \underline{u_i} - \underline{\underline{M}}(\underline{u_{i+1}}) \cdot \underline{u_{i+1}} \tag{5.31}$$

The set of equations is then solved iteratively using Gaussian elimination until each component of the vector Δu_i is less than a pre-defined threshold.

$$\underline{\underline{J}} \cdot \underline{\Delta u_i} = \underline{\underline{R}} \tag{5.32a}$$

$$\underline{u_{i+1}} = \underline{u_i} + \underline{\Delta u_i} \tag{5.32b}$$

At the start of each time step, the initial guess for $\underline{u_{i+1}}$ is taken to be equal to $\underline{u_i}$.

The initial time step size is set to $\Delta t = 1 \times 10^{-15}$ to ensure that the boundary conditions at the initial time step do not cause the solver to fail to converge. This is particularly important for the diffusion equation (Eq. 5.21b and Eq. 5.23a). To decrease the running time of the solver, the time step is increased after the initial step to a maximum value of $\Delta t = 0.0001 \cdot \frac{L^2}{D_{avg}}$.

6. MODEL OUTPUT

6.1 Mass Transfer

6.1.1 Drying Curves

Simulated drying curves are presented in Figs. 6.1, 6.2, and 6.3. The samples take less than ten hours to reach equilibrium except for very low equilibrium moisture contents. The change in drying rate is due to the decrease in effective diffusivity at low moisture contents (shown in both Fig. 2.6 and Fig. 2.7). Increasing the temperature serves to increase the drying rate. The drying curve for 313 K and an equilibrium moisture content of 0.05 calculated using Xiong's diffusivity model (Eq. 2.73) did not compare well to the experimentally observed data. Compared to the drying curve for 40 °C in Fig. 4.1, even the lowest moisture samples exhibited a sharp drop in the moisture content within the first ten hours. This indicates that the Eq. 2.73 is not accurate at low moisture contents.

6.1.2 Moisture Profiles

The simulated drying curves display a sharp gradient near the surface, particularly at both low drying temperatures and low equilibrium moisture contents. This is consistent with the observations made by Litchfield and Okos (1992) and Hills et al. (1997). At higher moisture contents, the surface gradient is less sharply defined. A large gradient, such as the one shown in Fig. 6.4, indicates that the effective diffusivity near the surface is significantly lower than the diffusivity near the interior of the slab. This causes the surface diffusivity to limit the rate of moisture removal.

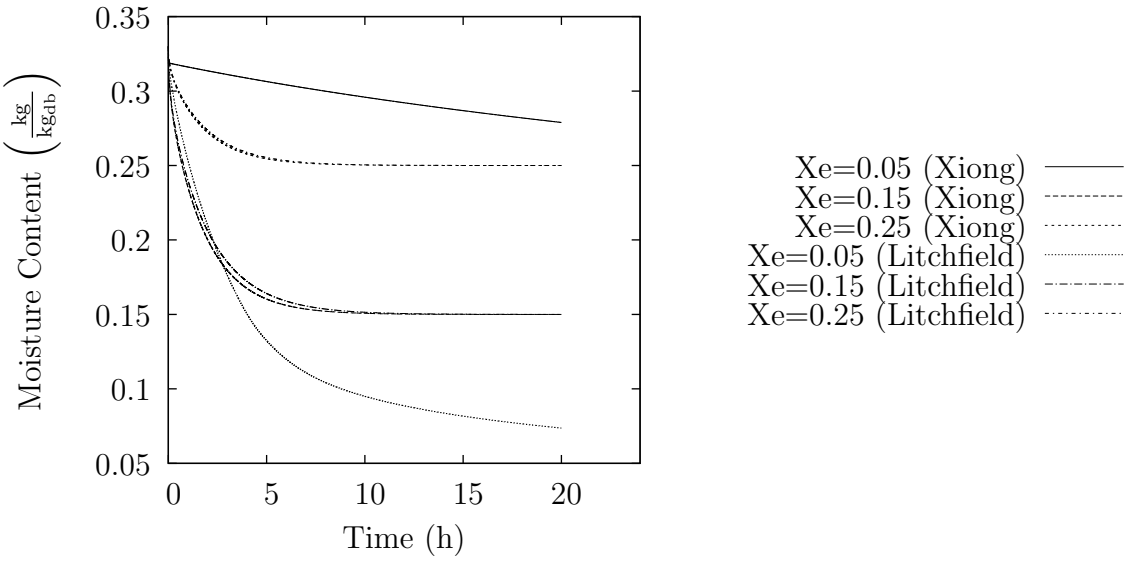

Fig. 6.1. Drying curves for selected equilibrium moisture contents. T=313 K D_{eff}: Eq. 2.71 and Eq. 2.73

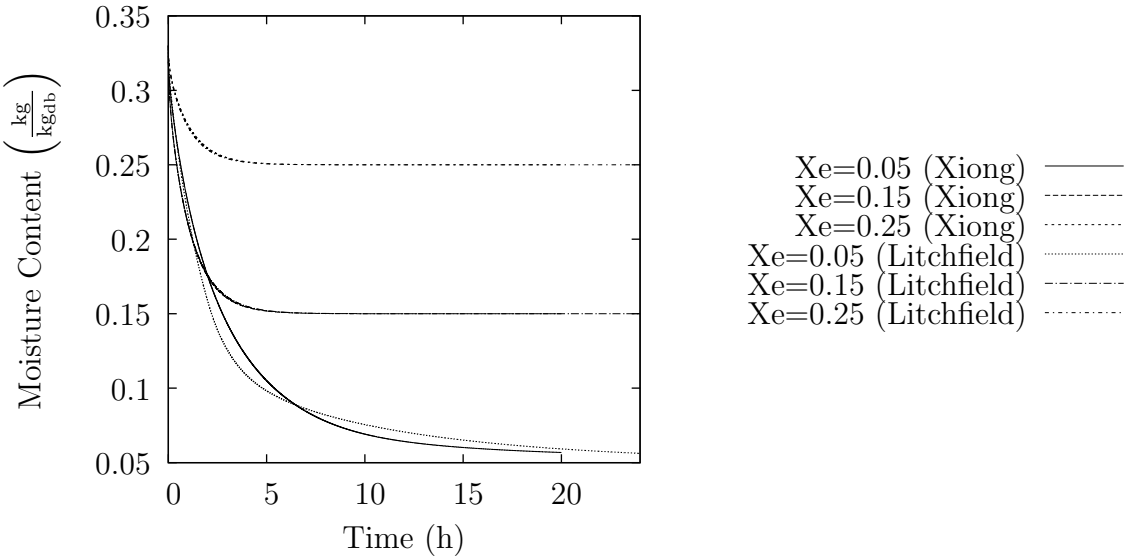

Fig. 6.2. Drying curves for selected equilibrium moisture contents. T=333 K D_{eff}: Eq. 2.71 and Eq. 2.73

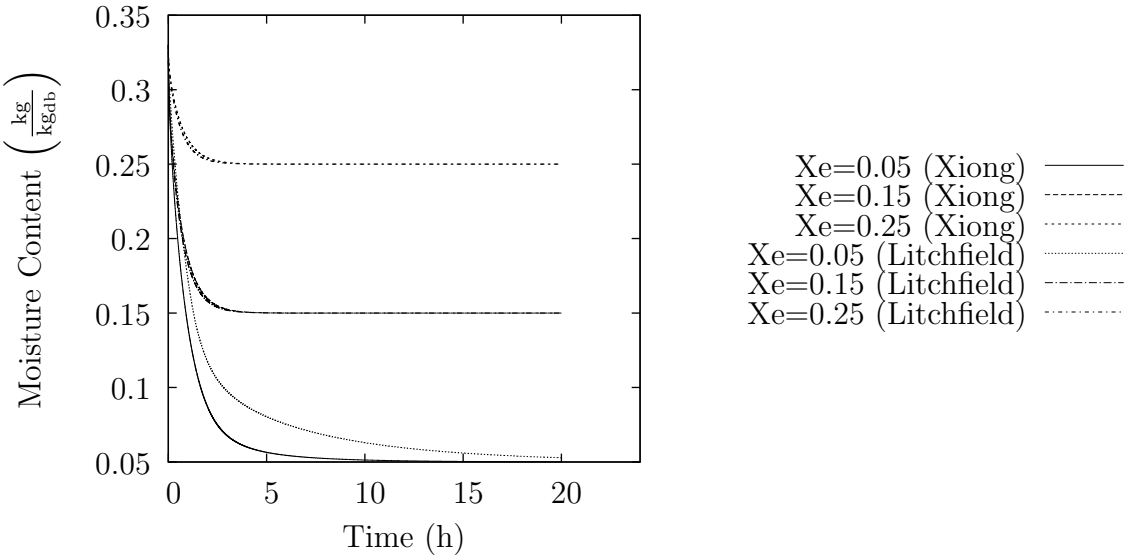

Fig. 6.3. Drying curves for selected equilibrium moisture contents. T=353 K D_{eff}: Eq. 2.71 and Eq. 2.73

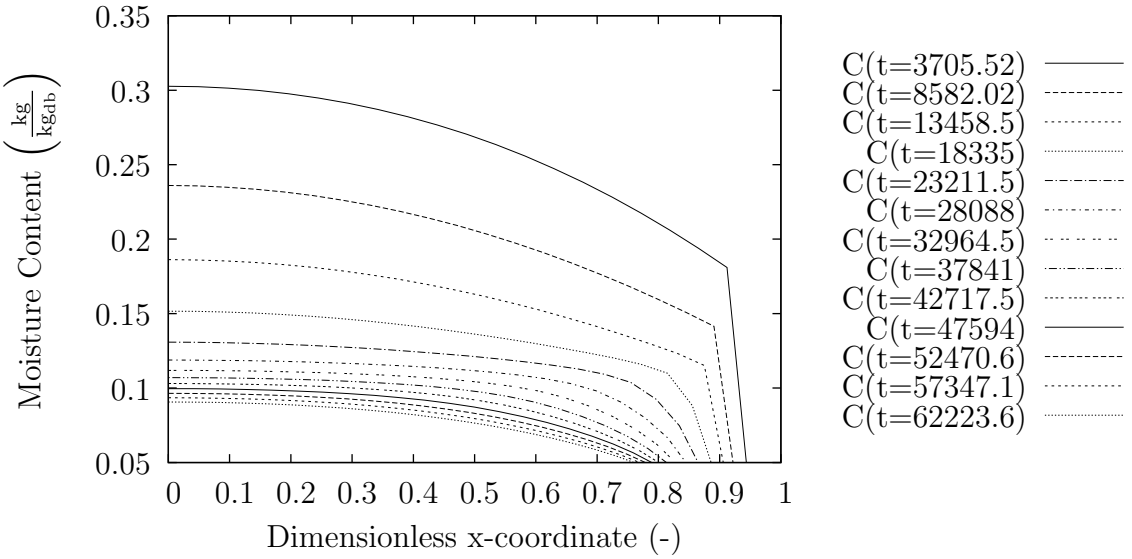

Fig. 6.4. Moisture profiles. $X_e = 0.05$; T=313 K; D_{eff}: Eq. 2.71

6.2 Shrinkage

At moderate to high moisture contents, the final strain increased at a roughly linear rate with decreasing equilibrium moisture content. When the equilibrium moisture content is set below 0.10 $\frac{\text{kg}}{\text{kg}_{\text{db}}}$ to 0.15 $\frac{\text{kg}}{\text{kg}_{\text{db}}}$, depending on drying temperature, the strain begins to decrease more quickly with decreasing moisture content. This sharp change was not observed experimentally.

Changing the diffusivity model has little effect on the observed strain at equilibrium. Figure 6.6 shows the relative difference between the strains calculated using each of the two effective diffusivity models. The only notable differences occur at low moisture contents where the samples were not entirely at equilibrium when the simulation ended.

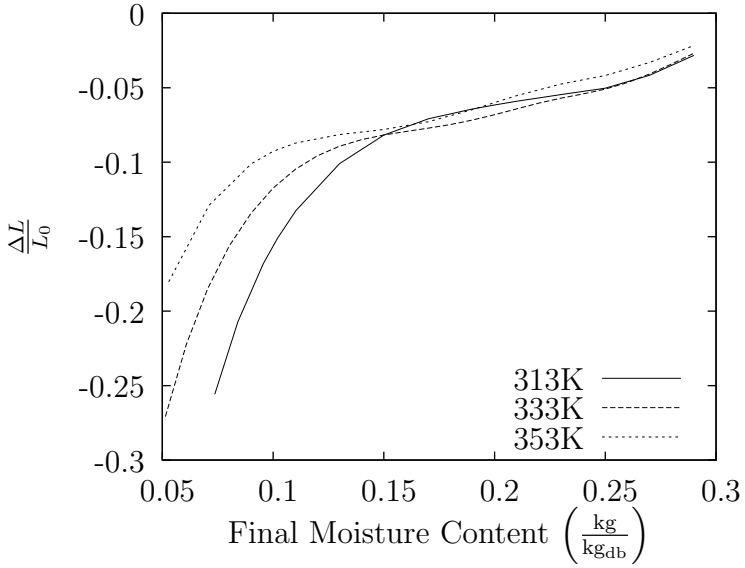

Fig. 6.5. Strain vs Time $\phi = 0.0612$; D_{eff}: Eq. 2.71

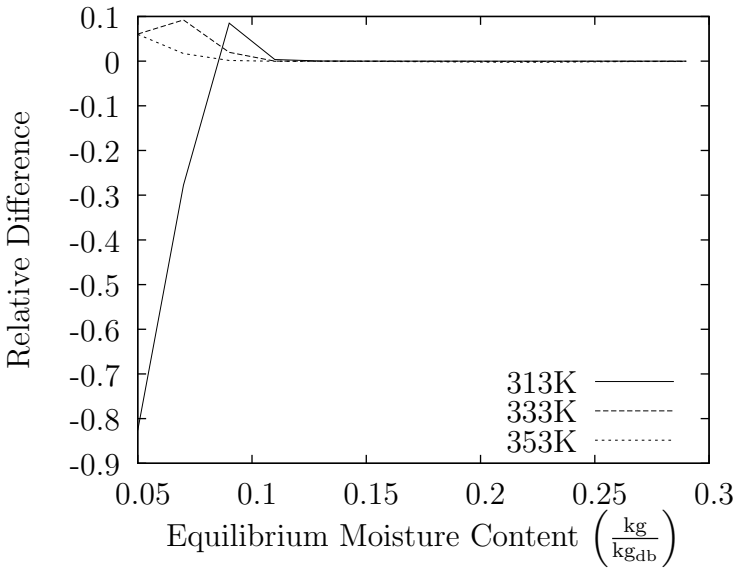

Fig. 6.6. Strain vs Time $\phi = 0.0612$; D_{eff}: Eq. 2.71, Eq. 2.73

6.3 Validation and Comparison with Literature

In comparison to the experimental data, the model fits well, especially at lower higher moisture contents. Additionally, at high temperatures, a greater range of moisture contents display a good fit with the numerical model (Fig. 6.7). At low moisture contents, however, the predicted strain deviates sharply from the experimentally observed strain. The numerical model calculates drying-induced stresses based on the water sorption isotherm, and this method is less accurate at lower moisture contents (Christenson, 1988). For the ranges over which the numerical model predicts the strain well, the error is between 10% and 20% (Fig. 6.8).

In order to predict what pressures would yield the experimentally observed shrinkage, the equilibrium stress was calculated from the regression model for linear shrinkage and the creep compliance model at infinite time $\left(\lim_{t\to\infty} J(t)\right)$. The resulting curves are presented in Fig. 6.10 and Fig. 6.11. These curves show that in order for the nu-

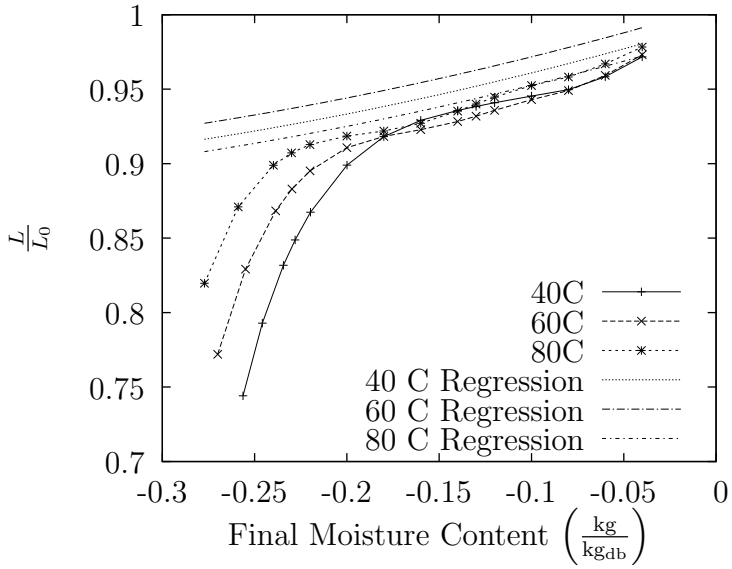

Fig. 6.7. Strain vs Time compared to the experimentally-determined regression equation. The regression model used is given in Eq. 4.2 with parameters found in Table 4.4.

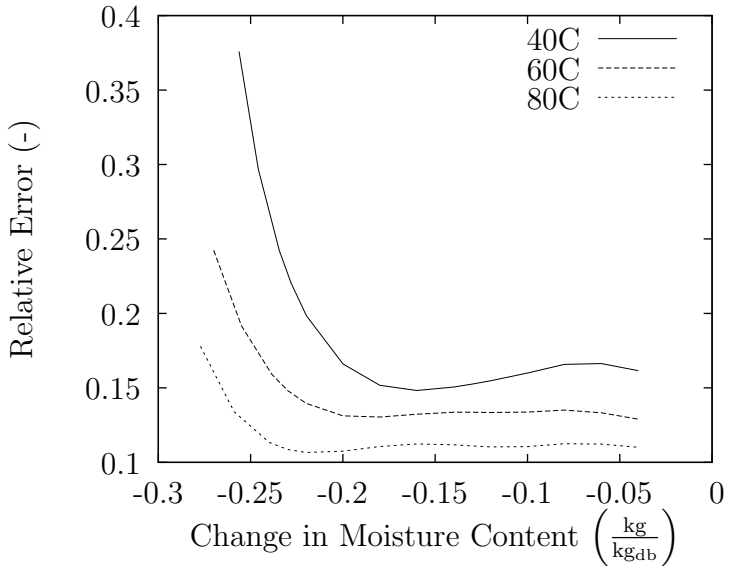

Fig. 6.8. Relative difference between experimentally determined regression equation and numerical analysis of strain vs. change in moisture content.

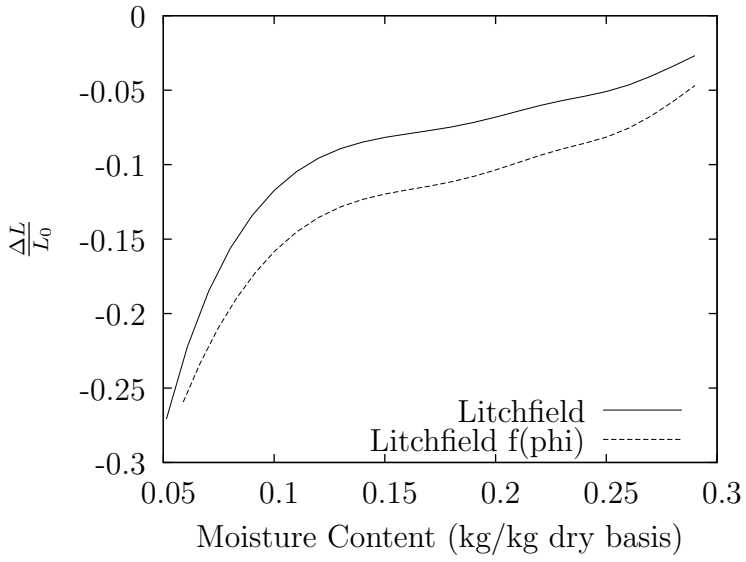

Fig. 6.9. Solid fraction added as a variable when calculating stress. $T = 333\,\mathrm{K}$; D_{eff}: Eq. 2.71

merically calculated shrinkage to line up with the experimental data, the capillary pressure should increase at a roughly linear rate once the moisture content drops below $0.12\,\frac{\mathrm{kg}}{\mathrm{kg_{db}}}$. Alternatively, if capillary stress increases as predicted by Eq. 2.23 and porosity decreases at lower moisture contents, then the effective stress curve would come more in line with what it would need to be to match experimental observations.

Porosity can be calculated dynamically when determining effective stress (Eq. 2.24). This would necessitate adding an additional equation to the system presented in section 5.9.1 to calculate stress, and would also require an estimate for the initial porosity of the sample. A shrinkage curve where solid fraction was used in place of porosity when calculating effective stress, and the porosity was initially assumed to be zero (pores completely filled with water) is presented in Fig. 6.9.

Low moisture capillary pressure curves are not well studied in literature (Bear et al., 2011). Typical capillary pressure curves do not provide data below the irreducible saturation limit. Lenhard and Parker (1987) determined the capillary pressure curve for water in a sandy soil, and their data is presented in Fig. 6.12. Engelhardt

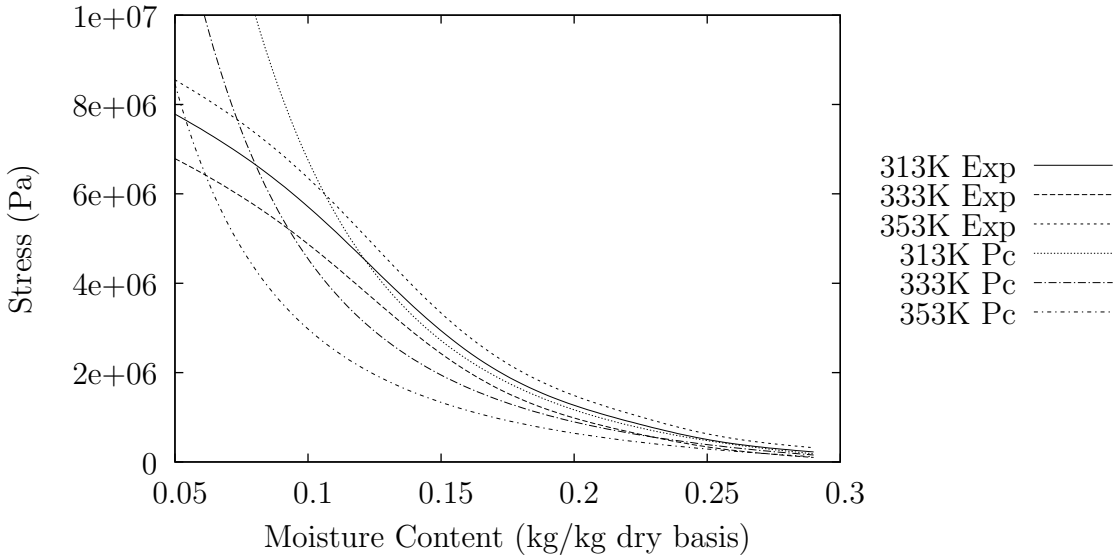

Fig. 6.10. Capillary pressure calculated both from Eq. 5.8 and 2.24 compared against back-calculated stress curves at selected temperatures. Stress was multipled by a factor of -1 to make it positive. ($\phi = 0.0612$)

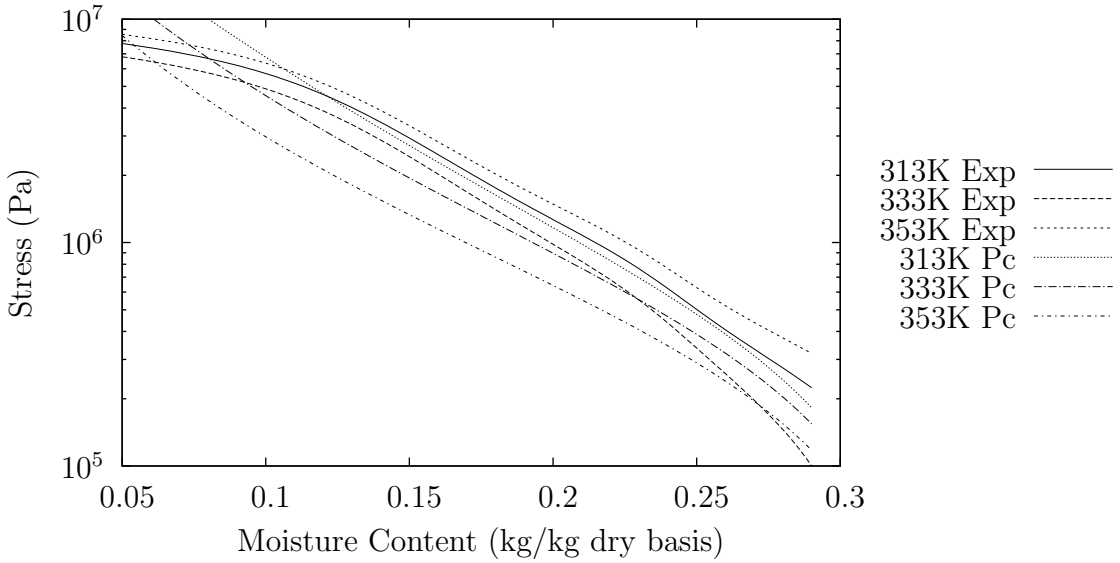

Fig. 6.11. Capillary pressure calculated both from Eq. 5.8 and 2.24 compared against back-calculated stress curves at selected temperatures and plotted on a semi-log scale. Stress was multipled by a factor of -1 to make it positive. ($\phi = 0.09$)

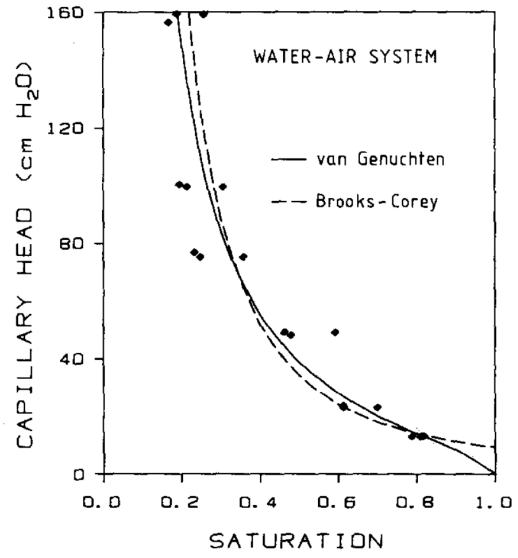

Fig. 6.12. Experimental capillary pressure-saturation data and models from Lenhard and Parker (1987)

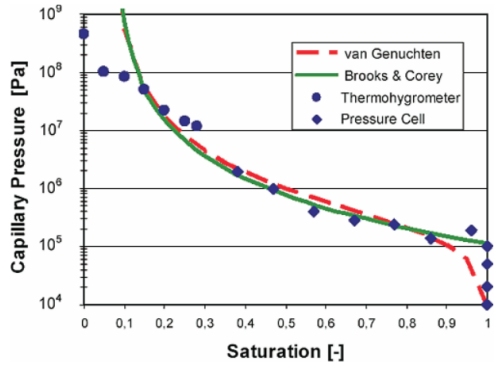

Fig. 6.13. Experimental capillary pressure-saturation data and models from Engelhardt et al. (2003)

et al. (2003) measured the capillary pressure curve for bentonite rock, and found that the capillary pressure curves calculated using water activity measurements did not fit the standard models at both extremely low and extremely high moisture contents. A plot of their results is presented in Fig. 6.13 The set of data they measured is more in

line with the experimentally-derived stress curves in Fig. 6.11 than the stress curves that were predicted using Eq. 2.23.

Alternatively, the amount of shrinkage could be limited by either glass transition temperature or the presence of non-shrinking particulates, such as starch, in the solid matrix (Willis, 2001). Neither of these mechanisms are well described by the model presented in this study, and either could be responsible for capping the amount of shrinkage at lower moisture contents.

The strain was repredicted using the pressure curve in Fig. 6.10 instead of the capillary pressure equation. The force here was calculated by taking the experimentally determined regression model for strain as a function of temperature and change in moisture content and calculating the equilibrium stress that would need to be experienced by the sample to create that deformation, as shown in Eq. 6.1.

$$\sigma = \frac{\epsilon_e}{J(t=\infty)} \tag{6.1}$$

Here, ϵ_e is the experimental strain calculated from Eq 4.2, and the value of $J(t)$ is calculated from Eq. 2.31. As can be seen in Fig. 6.14, this method for determining stress is only accurate for higher moisture contents. At low moisture contents, there is some deviation from the experimental results. This is because Eq. 6.1 does not factor in the time effects that are calculated in the FEM model. Figure 6.15 shows that time can have a significant impact on the predicted stress level. At lower moisture contents, it is likely that these time effects cause the creep compliance to increase, which results in higher strains. This can be seen in Eq. 6.2.

$$\epsilon = \int_0^t J(t-\tau)\frac{\partial}{\partial\tau}\left[\frac{\epsilon_e}{J_\infty}\right]d\tau \tag{6.2}$$

In order to compare the strain from the experimentally-derrived pressure curve to the experimental strain data, a purely elastic model numerical model was formulated. This formulation used Eq. 5.5 to water content, Eq 6.4 to calculate strain, and Eq 5.16 to determine deformation. These equations were combined into a three-by-three matrix in the same way as the viscoelastic model and solved using the same

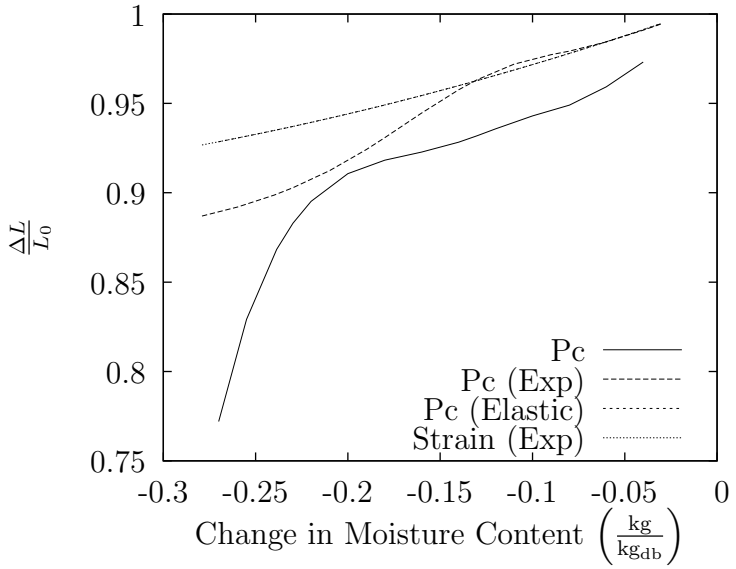

Fig. 6.14. Strain calculated from capillary pressure from Eq. 5.8 compared with experimentally determined strain, and strain based on a modified pressure curve calculated from experimental strain. (T=60 °C)

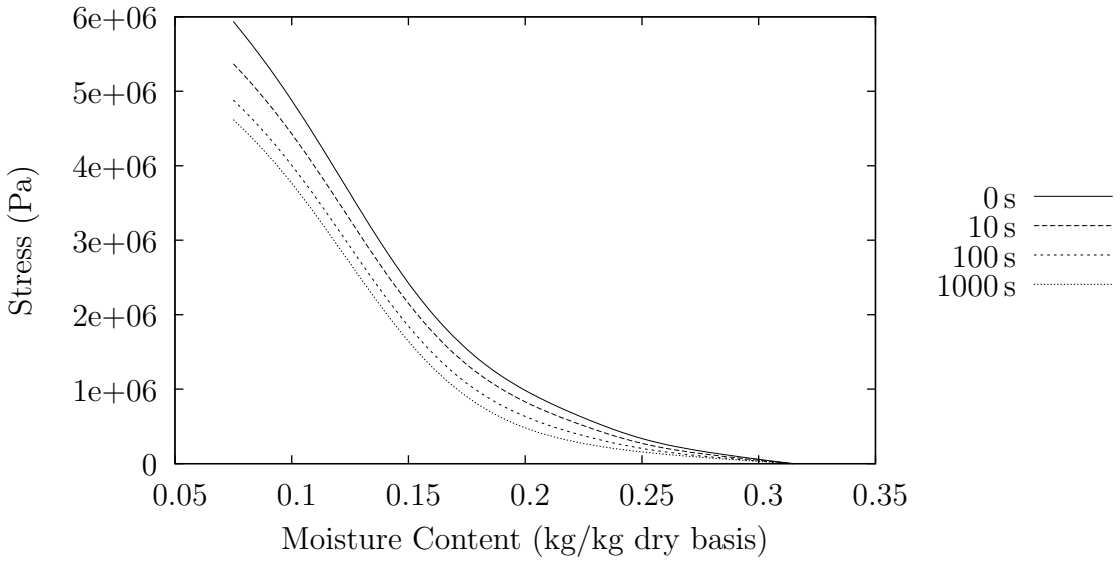

Fig. 6.15. Creep compliance at selected times. (T=60 °C)

technique.The results from the numerical model matched exactly with the the experimental shrinkage curves.

$$E = \frac{\sigma}{\epsilon} \tag{6.3}$$

$$\sigma = \frac{1}{J_\infty}\epsilon \tag{6.4}$$

6.4 Porosity

Once the strain and moisture content of the sample have been calculated, porosity can be calculated based on a volume balance, as shown in Eq. 6.5. Solid fraction can be determined from Eq. 6.6. The derivations for both of these equations are presented in Appendix G.

$$\phi = \frac{X_0 \frac{\rho_w}{\rho_s}(\epsilon + 1) + \epsilon - X \frac{\rho_w}{\rho_s}}{X_0 \frac{\rho_w}{\rho_s}(\epsilon + 1) + \epsilon + 1} \tag{6.5}$$

$$x_f = \frac{1}{(\epsilon + 1)\left(X_0 \frac{\rho_w}{\rho_s} + 1\right)} \tag{6.6}$$

Porosity is a function of initial moisture content, final moisture content, strain, and temperature. The density of the solid and liquid phases are calculated using the Choi-Okos equations (Choi and Okos, 1986).

The numerical model predicts that porosity increases as drying temperature increases. Porosity also increases as more water is removed. Low-moisture simulations show that the porosity increases initially and then decreases. This trend, shown in Fig 6.16, does not seem to be physically reasonable. Because the numerical model exhibits a large deviation from the experimental data at these low moisture contents, these results are likely invalid. The results for higher moisture content drying conditions (Fig. 6.17) do appear physically reasonable, however. The predicted trends agree with those presented in Rahman et al. (2005) for apple drying. For low equilibrium moisture contents, porosity increases with decreasing temperature because capillary pressure is lower at high temperatures. This results in less shrinkage for the same volume of water lost. At moderate to high equilibrium moisture contents, the effect of temperature on capillary pressure is lower, and the mechanical properties of

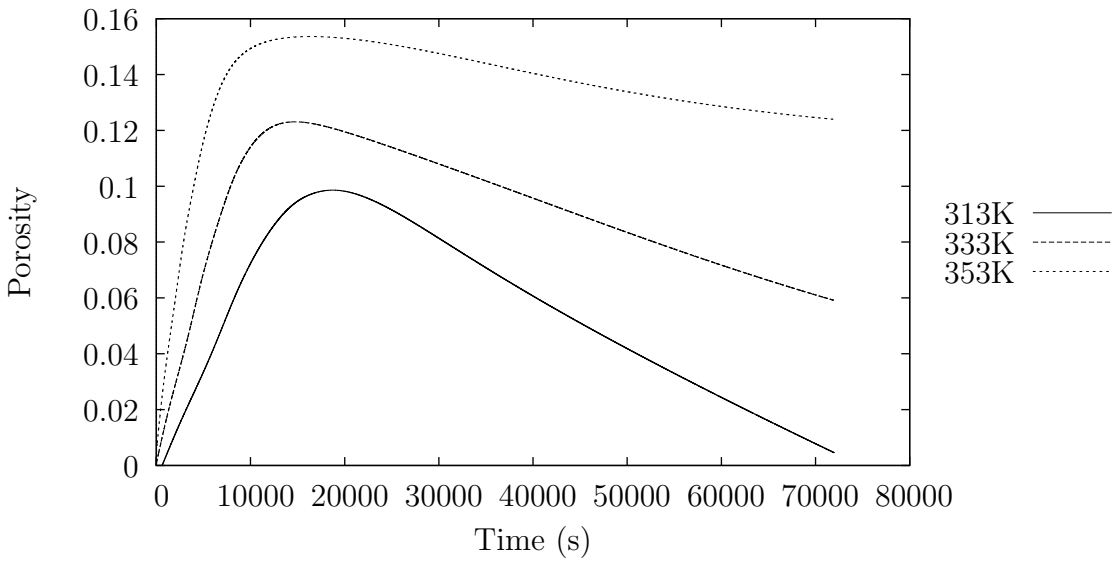

Fig. 6.16. Porosity vs. Time at an equilibrium moisture content of $0.05\,\frac{\text{kg}}{\text{kg}_{\text{db}}}$.

the dough also play a significant role in determining which temperature yields the minimum porosity.

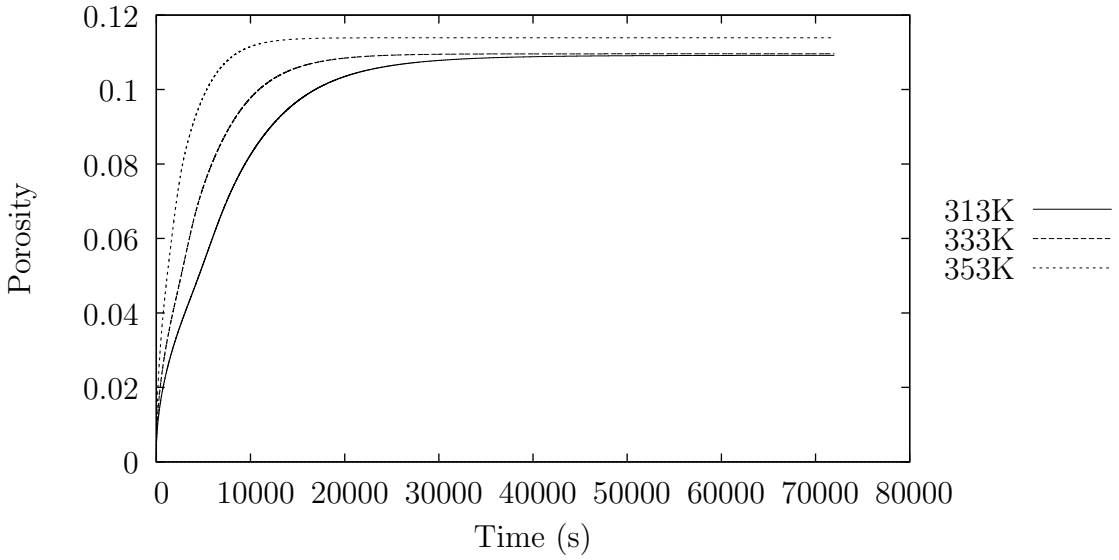

Fig. 6.17. Porosity vs. Time at an equilibrium moisture content of $0.15\,\frac{\text{kg}}{\text{kg}_{\text{db}}}$.

7. CONCLUSIONS

7.1 Experimental

7.1.1 Convection Drying

The experimental drying data showed that the overall drying time was less than twenty-four hours for each case. By the end of this time period, the samples had nearly reached equilibrium. The statistically significant parameters for determining shrinkage were the difference between initial and equilibrium moisture contents, drying temperature, and time taken to measure the sample once it was removed from the drying oven.

The most significant of these was the change in moisture content, which exhibited a quadratic relationship with shrinkage. The linear coefficient was comparable to other linear shrinkage coefficients from literature, and the presence of a quadratic term showed that glass transition temperature had a significant impact on the final dimensions of the product.

The temperature effect was statistically significant, but minor. It accounts for, at most, a 2-3% change in linear dimension. For comparison, the moisture content term accounts for approximately a 10% change in dimension over the range considered.

The final term, time between removal and measurement, is simply a quantification of experimental error. Like the temperature effect, it is relatively small, yet statistically significant. Calculating error in this way allows for better estimation of the other terms in the regression model.

7.1.2 Freeze Drying

Freeze dried samples displayed a degree of shrinkage consistent with the samples dried using convection. This indicates that the freeze drying conditions were above the glass transition temperature of the sample for at least a portion of the drying process. Literature sources indicate that samples that are freeze dried below their glass transition temperature exhibit minimal shrinkage.

7.2 Numerical Model

The finite element model was able to predict drying times and to determine the volume change of the simulated samples. The moisture profiles that were predicted displayed a sharp gradient near the surface and which was consistent with those found in both Litchfield and Okos (1992) and Hills et al. (1997). The total drying time was predicted to be less than twenty hours for all but the lowest equilibrium moisture contents, which agreed with experimental data.

Shrinkage was predicted to be primarily a function of the change in moisture content, with temperature having a minor effect. When predicting linear shrinkage, the model showed good agreement with the experimental data for equilibrium moisture contents above $0.15\,\frac{\mathrm{kg}}{\mathrm{kg_{db}}}$. In this moisture content range, the deviation from the experimentally measured shrinkage was between 10% and 20%, depending on the temperature. For low moisture conditions, the error is significantly larger, and these results do not agree well with the experiments conducted. The most likely source of this error is the capillary pressure equation used to predict drying stress.

8. RECOMMENDATIONS

8.1 Transient Shrinkage Measurements

In order to better understand the effects of differing rates of shrinkage and moisture diffusion, it is recommended that non-equilibrium shrinkage data be collected throughout the drying process. Due to the relatively short time period over which the bulk of moisture is lost during drying, and because the time scale over which stress relaxation occurs is short, collecting data continuously while the sample is drying would yield the best results. Shrinkage could be measured at regular intervals using a camera, and the results could be processed using software such as OpenCV (Bradski and Kaehler, 2008). A drying curve could be recorded using a scale connected to a data acquisition program on a computer.

The main obstacles to implementing this technique are that the camera and scale must both be isolated from the temperature, humidity, and vibration created by the drying chamber. To isolate the scale from noise due to vibration, it should be set outside the chamber on its own platform and hooked to a sample platform inside the drying chamber. Additionally, to reduce measurement errors from air currents moving, baffles or foam windscreens should be placed in front of the air inlets and outlets inside the chamber. Any residual noise should be removable through use of a Fourier transform-based noise-reduction algorithm.

The camera should either be rated for high temperature ($T > 80\,^{\circ}\mathrm{C}$) and sealed against moisture, or it should be located outside the drying chamber and fitted with fiber optics. Keeping the camera outside of the temperature-controlled environment or running the experiments at low temperatures would be key to reducing thermal noise (Johnson-Nyquist noise) measured by the CCD sensor. Additionally, the lighting and camera location relative to the samples should remain constant to simplify automation

of extracting the area of the sample and the reference from the images. A 5 MP image sensor was found to be adequate for measuring a single sample with reasonable accuracy at a distance of approximately 3 in., however a higher resolution sensor would allow for multiple samples to be measured simultaneously with a single image.

8.2 Improved Diffusivity Model

The primary diffusivity models used for this model did not factor in porosity or vapor flux (Litchfield and Okos, 1992; Xiong, 1989). Models do exist that include porosity, but these are mostly empirical (Waananen, 1989). It is recommended that the model presented in Xiong (1989) be modified to incorporate vapor flux. An attempt at developing this model is presented in Appendix G; however, more refinement is required for the model to match experimental results.

8.3 Capillary Pressure Measurement

The equation used for to predict drying stresses in this study (Eq. 2.23 is based off of the moisture sorption isotherm, and is not an accurate model of capillary pressures at lower moisture contents. More accurate data of suction potential could likely be obtained from experimental measurement using a tensiometer (Labuza and Lewicki, 1978; Rao et al., 2014). This would allow for better modelling of stresses in lower moisture samples.

8.4 Solid Mechanics Model

Alternate solid mechanics models should be investigated for a better fit with the experimental shrinkage data. The set of viscoelasticity data used incorporated the glass transition temperature well, but did not account for any material plasticity. Additionally, the relaxation times for the model were significantly smaller than other models (Cummings et al., 1993; Rozzi, 2002). The smaller relaxation times cause the

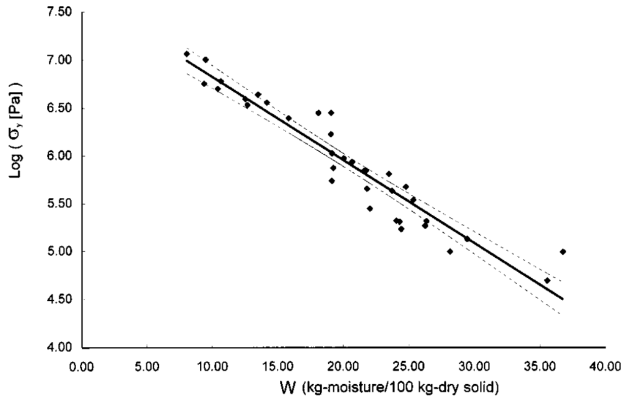

Fig. 8.1. Yield stress reported by Liu et al. (1997).

viscoelastic effects to be much less significant during the drying process, and a purely elastic model would yield similar results with significantly reduced computational complexity.

An elasto-plastic or visco-plastic model should also be considered. Because capillary pressure only causes shrinkage above the irreducible saturation point, a model that maintains strain after force is removed would be more effective at describing shrinkage than the currently used model. Liu et al. (1997) measured the yield stress for extruded durum semolina. Their results are summarized in Fig. 8.1.

REFERENCES

REFERENCES

Achanta, S. (1993). Multiphase transport in interacting porous media applied to drying. Masters, Purdue University, West Lafayette, IN.

Achanta, S., Cushman, J. H., and Okos, M. R. (1994). On multicomponent, multiphase thermomechanics with interfaces. *International Journal of Engineering Science*, 32:1717–1738.

Achanta, S., Okos, M. R., Cushman, J. H., and Kessler, D. P. (1997). Moisture transport in shrinking gels during saturated drying. *AIChE Journal*, 43(8):2112–2122.

Adam, G. and Gibbs, J. H. (1965). On the temperature dependence of cooperative relaxation properties in glass-forming liquids. *The Journal of Chemical Physics*, 43. Available from: 139-146.

Al-Muhtaseb, A., McMinn, W., and Magee, T. (2002). Moisture sorption isotherm characteristics of food products: A review. *Food and Bioproducts Processing*, 80:118 – 128. Available from: http://www.sciencedirect.com/science/article/pii/S0960308502703052.

Andrieu, J., Gonnet, E., and Laurent, M. (1989). Thermal conductivity and diffusivity of extruded durum wheat pasta. *Lebensmittel-Wissenschaft+ Technologie*, 22:6–10.

Andrieu, J. and Stamatopoulos, A. (1986). Durum wheat pasta drying kinetics. *Lebensmittel-Wissenschaft+ Technologie*, 19:448–456.

Andrieu, J., Stamatopoulos, A., and Zafiropoulos, M. (1985). Equation for fitting desorption isotherms of durum wheat pasta. *International Journal of Food Science & Technology*, 20:651–657. Available from: http://dx.doi.org/10.1111/j.1365-2621.1985.tb01825.x.

Arnold, M., Boccaccini, A., and Ondracek, G. (1996). Prediction of the poisson's ratio of porous materials. *Journal of Materials Science*, 31:1643–1646. Available from: http://dx.doi.org/10.1007/BF00357876.

Bažant, Z. P. (1975). Theory of creep and shrinkage in concrete structures: A precis of recent developments. *Mechanics today*, 2:1–93.

Bear, J., Buchlin, J., and for Fluid Dynamics, V. K. I. (1991). *Modelling and Applications of Transport Phenomena in Porous Media*. Theory and Applications of Transport in Porous Media. Springer Netherlands. Available from: http://books.google.com/books?id=Dft-_W_RcvoC.

Bear, J., Rubinstein, B., and Fel, L. (2011). Capillary pressure curve for liquid menisci in a cubic assembly of spherical particles below irreducible saturation. *Transport in Porous Media*, 89:63–73. Available from: http://dx.doi.org/10.1007/s11242-011-9752-7.

Bentz, D. P., Garboczi, E. J., and Quenard, D. A. (1998). Modelling drying shrinkage in reconstructed porous materials: Application to porous vycor glass. *Modelling and Simulation in Materials Science and Engineering*, 6:211.

Biot, M. A. (1941). General theory of three-dimensional consolidation. *Journal of applied physics*, 12:155–164.

Biot, M. A. (1973). Nonlinear and semilinear rheology of porous solids. *Journal of Geophysical Research*, 78:4924–4937.

Bird, R. B., Stewart, W. E., and Lightfoot, E. N. (2007). *Transport phenomena*. Wiley. com.

Bradski, G. and Kaehler, A. (2008). *Learning OpenCV: Computer Vision with the OpenCV Library*. O'Reilly Media. Available from: https://books.google.com/books?id=seAgiOfu2EIC.

Bressani, G. (2014). Shrinkage prediction during pasta dehydration. Masters, Purdue University, West Lafayette, IN.

Brinker, C. and Scherer, G. W. (1990). *Sol-gel Science: The Physics and Chemistry of Sol-gel Processing*. Academic Press. Available from: http://books.google.com/books?id=V2vRvsTaCwMC.

Carcione, J. M., Campanella, O. H., and Santos, J. E. (2007). A poroelastic model for wave propagation in partially frozen orange juice. *Journal of food engineering*, 80:11–17.

Chemkhi, S., Zagrouba, F., and Bellagi, A. (2004). Mathematical model for drying of highly shrinkable media. *Drying Technology*, 22:1023–1039. Available from: http://www.tandfonline.com/doi/abs/10.1081/DRT-120038578.

Choi, Y. and Okos, M. R. (1986). Effects of temperature and composition on the thermal properties of foods. *Food engineering and process applications*, 1:93–101.

Christensen, R. (2003). *Theory of Viscoelasticity*. Civil, Mechanical and Other Engineering Series. DOVER PUBN Incorporated. Available from: http://books.google.com/books?id=SvYQyLJtTtUC.

Christenson, H. K. (1988). Adhesion between surfaces in undersaturated vapors—a reexamination of the influence of meniscus curvature and surface forces. *Journal of Colloid and Interface Science*, 121:170 – 178. Available from: http://www.sciencedirect.com/science/article/pii/0021979788904201.

Crank, J. (1956). *The Mathematics of Diffusion*. Clarendon Press. Available from: http://books.google.com/books?id=GBYIAQAAIAAJ.

Cummings, D. A. (1981). Modeling of stress development during drying of extruded durum semolina. Masters, Purdue University, West Lafayette, IN.

Cummings, D. A., Litchfield, B. J., and Okos, M. R. (1993). Stress and failure prediction for the drying, tempering, and cooling of extruded durum semolina. *Drying Technology*, 11(7):1809–1836.

Cummings, D. A. and Okos, M. R. (1981). Viscoelastic behavior of extruded durum semolina as a function of temperature and moisture content. *Paper-American Society of Agricultural Engineers (USA)*.

Cuq, B. and Icard-Verniere, C. (2001). Characterisation of glass transition of durum wheat semolina using modulated differential scanning calorimetry. *Journal of Cereal Science*, 33:213 – 221. Available from: http://www.sciencedirect.com/science/article/pii/S0733521000903576.

Datta, A. K. (2006). Hydraulic permeability of food tissues. *International Journal of Food Properties*, 9:767–780. Available from: http://www.tandfonline.com/doi/abs/10.1080/10942910600596167.

Detournay, E. and Cheng, A. H. D. (1993). *Fundamentals of Poroelasticity*, volume 2, chapter 5, pages 113–171. Pergamon Press. Available from: http://ci.nii.ac.jp/naid/10007205437/en/.

Eichler, S., Ramon, O., Ladyzhinski, I., Cohen, Y., and Mizrahi, S. (1997). Collapse processes in shrinkage of hydrophilic gels during dehydration. *Food Research International*, 30:719 – 726. Available from: http://www.sciencedirect.com/science/article/pii/S0963996998000283.

Emri, I. (2005). Rheology of solid polymers. *Rheology Reviews*, pages pp 49–100.

Engelhardt, I., Finsterle, S., and Hofstee, C. (2003). Experimental and numerical investigation of flow phenomena in nonisothermal, variably saturated bentonite–crushed rock mixtures. *Vadose Zone Journal*, 2:239–246.

Erbas, M., Ertugay, M. F., and Certel, M. (2005). Moisture adsorption behaviour of semolina and farina. *Journal of Food Engineering*, 69:191 – 198. Available from: http://www.sciencedirect.com/science/article/pii/S0260877404003656.

Etzler, F. M. and Fagundus, D. M. (1987). The extent of vicinal water: Implications from the density of water in silica pores. *Journal of Colloid and Interface Science*, 115:513 – 519. Available from: http://www.sciencedirect.com/science/article/pii/0021979787900695.

Etzler, F. M. and White, P. J. (1987). The heat capacity of water in silica pores. *Journal of Colloid and Interface Science*, 120:94 – 99. Available from: http://www.sciencedirect.com/science/article/pii/0021979787903262.

Ferry, J. (1980). *Viscoelastic Properties of Polymers*. Wiley. Available from: https://books.google.com/books?id=9dqQY3Ujsx4C.

Field, K. (2009). The spaghetti wars. 2015(12/30/2015). Available from: http://www.designnews.com/document.asp?doc_id=228735.

Fisher, L. R. and Israelachvili, J. N. (1981a). Direct measurement of the effect of meniscus forces on adhesion: A study of the applicability of macroscopic thermodynamics to microscopic liquid interfaces. *Colloids and Surfaces*, 3:303 – 319. Available from: http://www.sciencedirect.com/science/article/pii/0166662281800583.

Fisher, L. R. and Israelachvili, J. N. (1981b). Experimental studies on the applicability of the kelvin equation to highly curved concave menisci. *Journal of Colloid and Interface Science*, 80:528 – 541. Available from: http://www.sciencedirect.com/science/article/pii/0021979781902125.

Frias, J., Foucat, L., Bimbenet, J., and Bonazzi, C. (2002). Modeling of moisture profiles in paddy rice during drying mapped with magnetic resonance imaging. *Chemical Engineering Journal*, 86:173 – 178. Available from: http://www.sciencedirect.com/science/article/pii/S1385894701002856.

Garg, S. K. and Nur, A. (1973). Effective stress laws for fluid-saturated porous rocks. *Journal of Geophysical Research*, 78:5911–5921. Available from: http://dx.doi.org/10.1029/JB078i026p05911.

Gawin, D., Pesavento, F., and Schrefler, B. A. (2002). Modelling of hygro-thermal behaviour and damage of concrete at temperature above the critical point of water. *International Journal for Numerical and Analytical Methods in Geomechanics*, 26:537–562. Available from: http://dx.doi.org/10.1002/nag.211.

Greenspan, L. (1977). Humidity fixed points of binary saturated aqueous solutions. *J of Research, National Bureau of Standards*, page 81–89.

Han, M. and Lytton, R. (1995). Theoretical prediction of drying shrinkage of concrete. *Journal of Materials in Civil Engineering*, 7:204–207. Available from: http://dx.doi.org/10.1061/(ASCE)0899-1561(1995)7:4(204).

Heldman, D., Lund, D., and Sabliov, C. (2006). *Handbook of Food Engineering, Second Edition*. Food science and technology. Taylor & Francis. Available from: http://books.google.com/books?id=vg10zQP0FkwC.

Hills, B., Godward, J., and Wright, K. (1997). Fast radial {NMR} microimaging studies of pasta drying. *Journal of Food Engineering*, 33:321 – 335. Available from: http://www.sciencedirect.com/science/article/pii/S0260877497000599.

Katekawa, M. and Silva, M. A. (2006). A review of drying models including shrinkage effects. *Drying technology*, 24:5–20.

Knoff, W. F. and Hopkins, I. L. (1972). An improved numerical interconversion for creep compliance and relaxation modulus. *Journal of Applied Polymer Science*, 16:2963–2972. Available from: http://dx.doi.org/10.1002/app.1972.070161120.

Kowalski, S. J. and Mielniczuk, B. (2006). Drying-induced stresses in macaroni dough. *Drying Technology*, 24:1093–1099. Available from: http://dx.doi.org/10.1080/07373930600778171.

Krokida, M., Karathanos, V., and Maroulis, Z. (1998). Effect of freeze-drying conditions on shrinkage and porosity of dehydrated agricultural products. *Journal of Food Engineering*, 35:369 – 380. Available from: http://www.sciencedirect.com/science/article/pii/S0260877498000314.

Labuza, T. P. and Lewicki, P. P. (1978). Measurement of gel water-binding capacity by capillary suction potential. *Journal of Food Science*, 43:1264–1269. Available from: http://dx.doi.org/10.1111/j.1365-2621.1978.tb15284.x.

Lenhard, R. and Parker, J. (1987). Measurement and prediction of saturation-pressure relationships in three-phase porous media systems. *Journal of Contaminant Hydrology*, 1:407 – 424. Available from: http://www.sciencedirect.com/science/article/pii/0169772287900179.

Leung, C. K. (2009). Non-linear drying diffusion and viscoelastic drying shrinkage modeling in hardened cement pastes. masters, Texas A&M University, College Station, TX.

Lewicki, P. P. and Pawlak, G. (2003). Effect of drying on microstructure of plant tissue. *Drying Technology*, 21:657–683. Available from: http://dx.doi.org/10.1081/DRT-120019057.

Litchfield, B. J. and Okos, M. R. (1992). Moisture diffusivity in pasta during drying. *Journal of food engineering*, 17(2):117–142.

Liu, H., Qi, J., and Hayakawa, K. (1997). Rheological properties including tensile fracture stress of semolina extrudates influenced by moisture content. *Journal of Food Science*, 62:813–820. Available from: http://dx.doi.org/10.1111/j.1365-2621.1997.tb15461.x.

Liu, Y. (2006). Some consideration on the langmuir isotherm equation. *Colloids and Surfaces A: Physicochemical and Engineering Aspects*, 274:34 – 36. Available from: http://www.sciencedirect.com/science/article/pii/S0927775705006138.

Matyka, M. and Koza, Z. (2012). How to calculate tortuosity easily? *arXiv preprint arXiv:1203.5646*.

Mayor, L. and Sereno, A. (2004). Modelling shrinkage during convective drying of food materials: a review. *Journal of Food Engineering*, 61:373 – 386. Available from: http://www.sciencedirect.com/science/article/pii/S0260877403001444.

Mead, D. W. (1994). Numerical interconversion of linear viscoelastic material functions. *Journal of Rheology (1978-present)*, 38. Available from: 1769-1795.

Mercier, S., Moresoli, C., Villeneuve, S., Mondor, M., and Marcos, B. (2013). Sensitivity analysis of parameters affecting the drying behaviour of durum wheat pasta. *Journal of Food Engineering*, 118:108 – 116. Available from: http://www.sciencedirect.com/science/article/pii/S0260877413001453.

Mercier, S., Villeneuve, S., Mondor, M., and Des Marchais, L.-P. (2011). Evolution of porosity, shrinkage and density of pasta fortified with pea protein concentrate during drying. *LWT-Food Science and Technology*, 44:883–890.

Migliori, M., Gabriele, D., de Cindio, B., and Pollini, C. M. (2005). Modelling of high quality pasta drying: mathematical model and validation. *Journal of Food Engineering*, 69:387 – 397. Available from: http://www.sciencedirect.com/science/article/pii/S0260877404003887.

Miranda, M. N. N. and Silva, M. A. (2005). Capillary pressure determination from sorption isotherms for mixtures of porous solids. *Drying Technology*, 23:1841–1857. Available from: http://www.tandfonline.com/doi/abs/10.1080/07373930500210028.

Mittal, G. S. (1999). Mass diffusivity of food products. *Food Reviews International*, 15:19–66. Available from: http://dx.doi.org/10.1080/87559129909541176.

Morland, L. W. and Lee, E. (1960). Stress analysis for linear viscoelastic materials with temperature variation. *Journal of Rheology*, 4:233.

Morrow, N. R. (1970). Irreducible wetting-phase saturations in porous media. *Chemical Engineering Science*, 25:1799 – 1815. Available from: http://www.sciencedirect.com/science/article/pii/0009250970800707.

Mulet, A., Tarrazo, J., Garcia-Reverter, J., and Berna, A. (1997). Shrinkage of cauliflower florets and stems during drying. *Engineering and Food at ICEF*, 7:97–100.

Narasimhan, T. and Witherspoon, P. (1977). Numerical model for saturated-unsaturated flow in deformable porous media 1. theory. *Water Resources Research*, 13:657–664.

Peleg, M. (1994). A model of mechanical changes in biomaterials at and around their glass transition. *Biotechnology Progress*, 10:385–388. Available from: http://dx.doi.org/10.1021/bp00028a007.

Perré, P. and Passard, J. (2004). A physical and mechanical model able to predict the stress field in wood over a wide range of drying conditions. *Drying Technology*, 22:27–44. Available from: http://www.tandfonline.com/doi/abs/10.1081/DRT-120028202.

Rahman, M. S., Al-Zakwani, I., and Guizani, N. (2005). Pore formation in apple during air-drying as a function of temperature: porosity and pore-size distribution. *Journal of the Science of Food and Agriculture*, 85:979–989. Available from: http://dx.doi.org/10.1002/jsfa.2056.

Rahman, M. S., Perera, C. O., Chen, X., Driscoll, R., and Potluri, P. (1996). Density, shrinkage and porosity of calamari mantle meat during air drying in a cabinet dryer as a function of water content. *Journal of Food Engineering*, 30:135 – 145. Available from: http://www.sciencedirect.com/science/article/pii/S0260877496000131.

Rao, M., Rizvi, S., Datta, A., and Ahmed, J. (2014). *Engineering Properties of Foods, Fourth Edition*. Food & culinary science. Taylor & Francis. Available from: https://books.google.com/books?id=3smSAwAAQBAJ.

Rozzi, L. A. Z. (2002). The effect of the rheological properties of semolina on the granulation process. Masters, Purdue University, West Lafayette, IN.

Samaniego-Esguerra, C. M., Boag, I. F., and Robertson, G. L. (1991). Comparison of regression methods for fitting the gab model to the moisture isotherms of some dried fruit and vegetables. *Journal of Food Engineering*, 13:115 – 133. Available from: http://www.sciencedirect.com/science/article/pii/026087749190014J.

Schanz, I. M. and Cheng, A. H. D. (2000). Transient wave propagation in a one-dimensional poroelastic column. *Acta Mechanica*, 145:1–18.

Schanz, I. M. and Cheng, A. H. D. (2001). Dynamic analysis of a one-dimensional poroviscoelastic column. *Journal of applied mechanics*, 68(2):192–198.

Schapery, R. (1967). Stress analysis of viscoelastic composite materials. *Journal of Composite Materials*, 1:228–267.

Shen, L. and Chen, Z. (2007). Critical review of the impact of tortuosity on diffusion. *Chemical Engineering Science*, 62:3748 – 3755. Available from: http://www.sciencedirect.com/science/article/pii/S0009250907003144.

Sozer, N. and Dalgic, A. (2007). Modelling of rheological characteristics of various spaghetti types. *European Food Research and Technology*, 225:183–190. Available from: http://dx.doi.org/10.1007/s00217-006-0402-1.

Steffe, J. (1996). *Rheological Methods in Food Process Engineering*. Freeman Press. Available from: http://books.google.com/books?id=LrrdONuST9kC.

Sterling, M. R. (2000). The role of glass transition temperature in the high shear granulation of semolina. Masters, Purdue University, West Lafayette, IN.

Takhar, P. S., Cushman, J. H., and Maier, D. E. (2003a). Multiscale fluid transport theory for swelling biopolymers. *Chemical Engineering Science*, 58:2409–2419.

Takhar, P. S., Cushman, J. H., and Maier, D. E. (2003b). Three scale thermomechanical theory for swelling biopolymeric systems. *Chemical Engineering Science*, 58:4017 – 4035. Available from: http://www.sciencedirect.com/science/article/pii/S0009250903002835.

Takhar, P. S., Maier, D. E., Cushman, J. H., and Campanella, O. H. (2004). Effect of viscoelastic relaxation on moisture transport in foods. part ii: Sorption and drying of soybeans. *Journal of mathematical biology*, 49(1):20–34.

Temmerman, J. D., Verboven, P., Delcour, J., Nicolaï, B., and Ramon, H. (2008). Drying model for cylindrical pasta shapes using desorption isotherms. *Journal of Food Engineering*, 86:414 – 421. Available from: http://www.sciencedirect.com/science/article/pii/S0260877407005468.

Temmerman, J. D., Verboven, P., Nicolaï, B., and Ramon, H. (2007). Modelling of transient moisture concentration of semolina pasta during air drying. *Journal of Food Engineering*, 80:892 – 903. Available from: http://www.sciencedirect.com/science/article/pii/S0260877406005437.

Terzaghi, K. v. (1923). Die berechnung der durchlassigkeitsziffer des tones aus dem verlauf der hydrodynamischen spannungserscheinungen. *Sitzungsberichte der Akademie der Wissenschaften in Wien, Mathematisch-Naturwissenschaftliche Klasse, Abteilung IIa*, 132:125–138.

Thiffeault, J.-L. (2003). Advection–diffusion in lagrangian coordinates. *Physics Letters A*, 309:415 – 422. Available from: http://www.sciencedirect.com/science/article/pii/S0375960103002445.

Villeneuve, S. and Gélinas, P. (2007). Drying kinetics of whole durum wheat pasta according to temperature and relative humidity. {*LWT*} - *Food Science and Technology*, 40:465 – 471. Available from: http://www.sciencedirect.com/science/article/pii/S0023643806000156.

Waananen, K. M. (1989). Analysis of mass transfer mechanisms during drying of extruded pasta. Master's thesis, Purdue University, West Lafayette.

Waananen, K. M. and Okos, M. R. (1996). Effect of porosity on moisture diffusion during drying of pasta. *Journal of Food Engineering*, 28:121 – 137. Available from: http://www.sciencedirect.com/science/article/pii/0260877494000824.

Wang, J. C. (1984). Young's modulus of porous materials. *Journal of Materials Science*, 19:801–808. Available from: http://dx.doi.org/10.1007/BF00540451.

Williams, J. (1980). *Stress analysis of polymers*. Ellis Horwood series in engineering science. E. Horwood. Available from: http://books.google.com/books?id=7tBRAAAAMAAJ.

Williams, M. L., Landel, R. F., and Ferry, J. D. (1955). The temperature dependence of relaxation mechanisms in amorphous polymers and other glass-forming liquids. *Journal of the American Chemical Society*, 77:3701–3707. Available from: http://dx.doi.org/10.1021/ja01619a008.

Willis, B. F. (2001). The effects of rheological properties on mass transfer and stress development in pasta-type products during drying. Phd, Purdue University, West Lafayette, IN. Available from: http://search.proquest.com/docview/304726927?accountid=13360.

Xiong, X. (1989). Effects of food composition and structure on its water binding properties. Masters, Purdue University, West Lafayette, IN.

Xiong, X., Narsimhan, G., and Okos, M. R. (1992). Effect of composition and pore structure on binding energy and effective diffusivity of moisture in porous food. *Journal of Food Engineering*, 15:187 – 208. Available from: http://www.sciencedirect.com/science/article/pii/026087749290050G.

Yildiz, M. E. and Kokini, J. L. (2001). Determination of williams–landel–ferry constants for a food polymer system: Effect of water activity and moisture content. *Journal of Rheology (1978-present)*, 45:903–912. Available from: http://scitation.aip.org/content/sor/journal/jor2/45/4/10.1122/1.1380425.

Zhu, H., Mukherjee, S., and Dhall, A. (2011). A finite element analysis of coupling between water absorption and swelling of foodstuffs during soaking. *Transport in porous media*, 88(3):399–419.

Zienkiewicz, O., Taylor, R., and Fox, D., editors (2014). *The Finite Element Method for Solid and Structural Mechanics*. The Finite Element Method for Solid and Structural Mechanics (Seventh Edition). Butterworth-Heinemann, Oxford, seventh edition edition. Available from: http://www.sciencedirect.com/science/article/pii/B9781856176347000168.

APPENDICES

A. SENSITIVITY AND ERROR ANALYSIS

A.1 Sensitivity Analysis

In order to determine the effect of key process parameters on the degree of shrinkage observed, a sensitivity analysis was conducted. The two main variables of interest were ambient temperature and equilibrium moisture content. The values used for temperature were 313 K, 333 K, and 353 K, and the equilibrium moisture contents were 0.05, 0.10, and 0.15.

Table A.1.
Sensitivity analysis of the Oswin isotherm equation. (Eq. 2.5)

Deviation	40 °C	60 °C	80 °C
$T - 10\%$	24.7842%	29.154%	40.3304%
$T + 10\%$	24.6908%	35.3212%	60.3371%
$k_0 - 10\%$	14.3759%	18.4217%	25.6364%
$k_0 + 10\%$	14.3759%	18.4217%	25.6364%
$k_1 - 10\%$	4.37592%	8.42167%	15.6364%
$k_1 + 10\%$	4.37592%	8.42167%	15.6364%
$n_0 - 10\%$	3.43044%	3.65067%	3.86612%
$n_0 + 10\%$	3.57437%	3.81756%	4.05192%
$n_1 - 10\%$	2.84148%	4.50189%	6.29859%
$n_1 + 10\%$	2.93954%	4.75838%	6.80704%

Table A.2.
Sensitivity analysis of theoretical diffusivity equation. The variables k_0, k_1, n_0, and n_1 are used to calculate binding energy, E_b and, and show the effect of changes in the isotherm on diffusivity. The changes in E_b were calculated by multiplying binding energy by a factor of 0.9 or 1.1. (Eq. 5.3).

Deviation	40 °C	60 °C	80 °C
$T - 10\%$	64.8176%	61.744%	58.6966%
$T + 10\%$	123.931%	110.29%	99.0555%
$k_0 - 10\%$	5.52667%	3.87048%	2.74508%
$k_0 + 10\%$	5.13731%	3.46728%	2.13609%
$k_1 - 10\%$	1.51993%	1.65695%	2.16859%
$k_1 + 10\%$	1.41101%	1.49374%	1.78963%
$n_0 - 10\%$	2.83907%	2.12385%	1.45913%
$n_0 + 10\%$	2.83591%	2.12141%	1.46812%
$n_1 - 10\%$	1.7003%	2.22119%	2.31709%
$n_1 + 10\%$	1.62787%	2.124%	2.24756%
$D_0 - 10\%$	10.0%	10.0%	10.0%
$D_0 + 10\%$	10.0%	10.0%	10.0%
$E_a - 10\%$	130.756%	119.453%	109.895%
$E_a + 10\%$	56.6641%	54.4321%	52.3571%
$K - 10\%$	0.579177%	0.568578%	0.546506%
$K + 10\%$	0.520496%	0.510358%	0.489833%
$E_b - 10\%$	3.96158%	3.85389%	3.66398%
$E_b + 10\%$	3.55759%	3.48729%	3.34549%

Table A.3.
Difference between $\hat{G}(s)$ and $\mathcal{L}\left\{\frac{1}{s^2\mathcal{L}^{-1}\left\{\frac{1}{s^2\hat{G}(s)}\right\}}\right\}$

	$X_e = 0.05$	$X_e = 0.10$	$X_e = 0.15$
313 K	4.24113%	3.32904%	3.22729%
333 K	4.04593%	3.46587%	4.21189%
353 K	3.93463%	3.90364%	5.48543%

Table A.4.
Relative humidities at selected conditions.

	$X_e = 0.05$	$X_e = 0.10$	$X_e = 0.15$
313 K	0.113 505	0.442 891	0.698 191
333 K	0.241 918	0.585 775	0.771 601
353 K	0.410 120	0.709 539	0.835 925

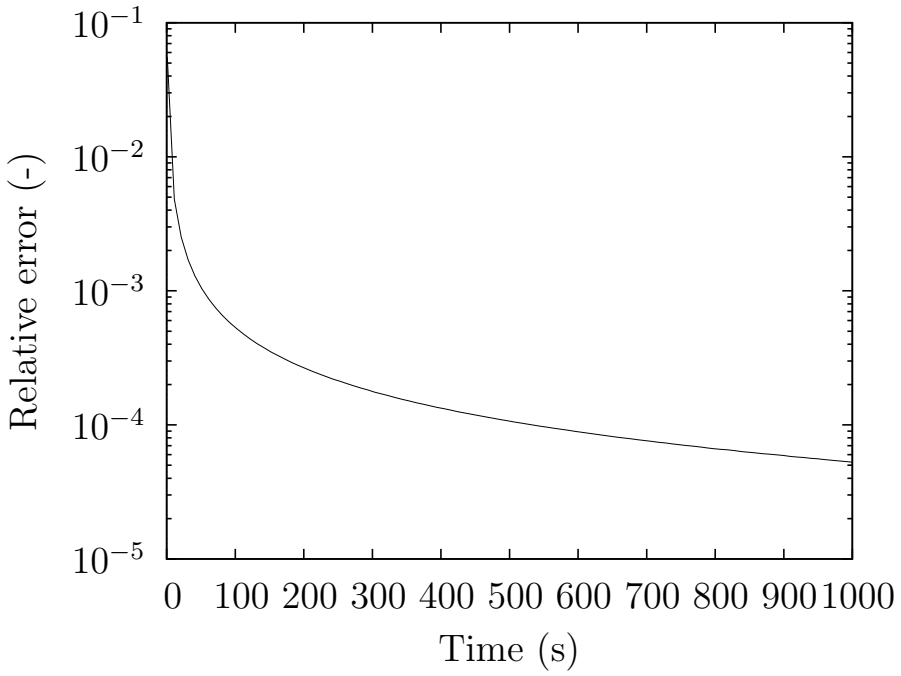

Fig. A.1. Numerical inverse Laplace transform error (T=353 K, M=0.15)

Table A.5.
Set of model parameters

Equation	Variable	Value	Units
Composition	M_{pro}	0.0166	kg/kg
	M_{fat}	0.0239	kg/kg
	M_{car}	0.784	kg/kg
	M_{fib}	0.0179	kg/kg
	M_{ash}	0.00824	kg/kg
Isotherm	k_0	0.176	-
	k_1	-1.748×10^{-3}	1/K
	n_0	0.182	-
	n_1	6.946×10^{-3}	1/K
Diffusivity	D_0	6.3910×10^{-8}	m^2/s
	E_a	21760	J/mol
	K	1032.558	-
Concentrations	C_0	0.5	kg/kg db
	C_a	0.05	kg/kg db
Temperature	T	333	K
Slab Half-thickness	L	1×10^{-3}	m
Kelvin Equation	M_w	1.802×10^{-5}	$\frac{m^3}{mol}$
Poisson Ratio	ν	0.37	-

B. DRYING DATA

Table B.1.
AES data taken at T=60C and RH=43%.

Time	Moisture Content		Area		
	Initial	Final	Initial	Final	V/V0
(min)	$(d.b.)$	$(d.b.)$	(in^2)	(in^2)	
1065	0.4348	0.0937	0.4197	0.3524	0.7696
1065	0.4661	0.1137	0.5007	0.3391	0.5574
1065	0.4580	0.1059	0.4283	0.4024	0.9107
2834	0.4179	0.0765	0.4923	0.3684	0.6473
2834	0.4359	0.0863	0.4820	0.3588	0.6422
2834	0.4248	0.0784	0.4573	0.3544	0.6821
4475	0.4370	0.0943	0.4272	0.3572	0.7648
4475	0.4355	0.0951	0.4460	0.3511	0.6986
4475	0.4271	0.0918	0.4356	0.3856	0.8330
6001	0.4475	0.0953	0.4896	0.3973	0.7309
6001	0.4332	0.0963	0.4483		
6001	0.4238	0.0873	0.5692	0.4704	0.7513
7430	0.4367	0.0904	0.5671	0.4888	0.8001
7430	0.4338	0.0857	0.5502	0.4758	0.8042
7430	0.4339	0.0924	0.4392	0.3611	0.7453

Table B.2.
AES data taken at T=60C and RH=85%.

Moisture Content		Area		
Initial $(d.b.)$	Final $(d.b.)$	Initial (in^2)	Final (in^2)	V/V0
0.4651	0.2189	0.3654	0.3214	0.8252
0.4560	0.2169	0.3039	0.2768	0.8689
0.4443	0.2108	0.2982	0.2576	0.8029
0.4658	0.2139	0.3250	0.3065	0.9157
0.4530	0.2218	0.2995	0.2621	0.8186
0.4476	0.2143	0.3607	0.3159	0.8198
0.4353	0.2102	0.3255	0.3023	0.8950
0.4344	0.2092	0.2750	0.2557	0.8967

Table B.3.: Summary of data collected from salt drying experiments.

	Temperature		Moisture Content		Area			Time	
Salt	Target (°C)	Measured (°C)	Initial (*d.b.*)	Final (*d.b.*)	Initial ($in.^2$)	Final ($in.^2$)	V/V0	Loaded	Removed
K_2SO_4	40	43.2	0.412	0.3963	0.3317	0.3208	0.9511	10/31/2015 16:14:56	11/05/2015 13:58:31
K_2SO_4	40	43.2	0.4886	0.3958	0.3909	0.3707	0.9234	10/31/2015 16:16:44	11/05/2015 14:00:39
K_2SO_4	40	43.2	0.4708	0.3624	0.345	0.313	0.8643	10/31/2015 16:17:36	11/05/2015 14:02:44
K_2SO_4[i]	40	43.2	0.4782	0.3563	0.3543	0.3266	0.8851	10/31/2015 16:19:18	11/05/2015 14:05:26
KNO_3	40	43.2	0.415	0.2227	0.3301	0.2816	0.788	10/31/2015 16:10:03	11/05/2015 13:51:49
KNO_3	40	43.2	0.4352	0.2288	0.3697	0.3258	0.8274	10/31/2015 16:11:18	11/05/2015 13:51:55
KNO_3	40	43.2	0.4178	0.2181	0.3622	0.3284	0.8634	10/31/2015 16:12:32	11/05/2015 13:54:10
KNO_3	40	43.2	0.4186	0.2301	0.3362	0.3043	0.861	10/31/2015 16:13:37	11/05/2015 13:56:32
K_2CO_3	40	49.3			0.3766			10/31/2015 16:04:27	
K_2CO_3	40	49.3	0.4135	0.1029	0.3787	0.3091	0.7374	10/31/2015 16:05:52	11/05/2015 14:25:21
K_2CO_3	40	49.3	0.4112	0.1014	0.355	0.2777	0.692	10/31/2015 16:07:13	11/05/2015 14:27:35
K_2CO_3	40	49.3	0.408	0.1015	0.4051	0.3372	0.7596	10/31/2015 16:08:38	11/05/2015 14:29:16

[i]Mold growth

Salt	Temperature		Moisture Content		Area		V/V0	Time	
	Target	Measured	Initial	Final	Initial	Final		Loaded	Removed
$NaCl$[ii]	40	49.3	0.4271	0.156	0.4052	0.3103	0.6702	10/31/2015 15:56:49	11/05/2015 14:15:56
$NaCl$	40	49.3	0.3838	0.1519	0.4433	0.3617	0.7371	10/31/2015 15:58:13	11/05/2015 14:18:20
$NaCl$	40	49.3	0.421	0.1584	0.3508	0.2955	0.7734	10/31/2015 16:02:09	11/05/2015 14:20:46
$NaCl$	40	49.3	0.3963	0.1577	0.3365	0.2789	0.7545	10/31/2015 16:03:16	11/05/2015 14:23:15
$LiCl$	40	49.3	0.4567	0.0649	0.424	0.3472	0.7409	10/31/2015 15:51:32	11/05/2015 14:07:48
$LiCl$	40	49.3	0.4383	0.0599	0.3425	0.267	0.6884	10/31/2015 15:52:55	11/05/2015 14:09:44
$LiCl$	40	49.3	0.4484	0.0707	0.3482	0.2681	0.6754	10/31/2015 15:54:18	11/05/2015 14:11:54
$LiCl$	40	49.3	0.4416	0.0648	0.3318	0.2651	0.7143	10/31/2015 15:55:34	11/05/2015 14:13:51
K_2SO_4[i]	50	52.4	0.5929	0.5690	0.4550	0.3978	0.8175	11/25/2015 17:25:42	11/19/2015 19:50:29
K_2SO_4[i]	50	52.4	0.5186	0.3650	0.4024	0.3490	0.8077	11/25/2015 17:29:18	11/19/2015 19:51:12
K_2SO_4[i]	50	52.4	0.5512	0.5304	0.5023	0.4011	0.7137	11/25/2015 17:27:49	11/19/2015 19:52:24
K_2SO_4[i]	50	52.4	0.5516	0.5674	0.4649	0.3889	0.7650	11/25/2015 17:30:47	11/19/2015 19:53:14
KNO_3	50	52.4	0.5076	0.1917	0.4411	0.3646	0.7516	11/25/2015 17:34:53	11/19/2015 19:54:16
KNO_3	50	52.4	0.4980	0.1818	0.3601	0.3088	0.7939	11/25/2015 17:34:08	11/19/2015 19:55:10
KNO_3	50	52.4	0.5083	0.1850	0.3288	0.2707	0.7468	11/25/2015 17:33:17	11/19/2015 19:56:08
KNO_3	50	52.4	0.4888	0.1803	0.4441	0.3802	0.7921	11/25/2015 17:32:24	11/19/2015 19:57:04
K_2CO_3	50	42.6	0.5083	0.1047	0.3991	0.3170	0.7080	11/25/2015 17:43:40	11/19/2015 20:02:17

[ii]Outlier

Salt	Temperature		Moisture Content		Area		V/V0	Time	
	Target	Measured	Initial	Final	Initial	Final		Loaded	Removed
K_2CO_3	50	42.6	0.5087	0.1024	0.3909	0.3008	0.6751	11/25/2015 17:40:36	11/19/2015 20:03:10
K_2CO_3	50	42.6	0.4696	0.0822	0.4430	0.3556	0.7192	11/25/2015 17:39:41	11/19/2015 20:04:19
K_2CO_3	50	42.6	0.4671	0.0914	0.4467	0.3502	0.6939	11/25/2015 17:37:04	11/19/2015 20:05:11
$NaCl$	50	42.6	0.5006	0.1521	0.4079	0.3465	0.7827	11/25/2015 17:41:32	11/19/2015 19:57:54
$NaCl$	50	42.6	0.4979	0.1550	0.3928	0.3303	0.7711	11/25/2015 17:42:39	11/19/2015 19:58:47
$NaCl$[ii]	50	42.6	0.4959	0.1518	0.3240	0.2829	0.8159	11/25/2015 17:35:58	11/19/2015 19:59:36
$NaCl$	50	42.6	0.4910	0.1445	0.3330	0.2617	0.6964	11/25/2015 17:38:15	11/19/2015 20:01:10
$LiCl$[iii]	50	42.6	0.4816	0.0577	0.4646	0.3581	0.6768	11/25/2015 17:46:25	11/19/2015 20:06:07
$LiCl$[iii]	50	42.6	0.4751	0.0494	0.5422	0.4193	0.6801	11/25/2015 17:47:03	11/19/2015 20:07:16
$LiCl$[iii]	50	42.6	0.4701	0.0456	0.5239	0.4037	0.6763	11/25/2015 17:45:31	11/19/2015 20:08:01
$LiCl$[iii]	50	42.6	0.4486	0.0537	0.5047	0.3742	0.6384	11/25/2015 17:44:47	11/19/2015 20:08:47
K_2SO_4	60	63.3	0.3671	0.3413	0.3056	0.3004	0.975	10/05/2015 16:19:24	10/16/2015 23:22:24
K_2SO_4	60	63.3	0.3572	0.3307	0.3278	0.331	1.015	10/05/2015 16:32:29	10/16/2015 23:17:29
K_2SO_4	60	63.3	0.3663	0.3417	0.2947	0.294	0.9965	10/05/2015 16:35:49	10/16/2015 23:15:42
K_2SO_4	60	63.3						10/05/2015 16:38:00	
KNO_3	60	63.3	0.3449	0.1547	0.3249	0.2807	0.8031	10/05/2015 16:41:37	10/16/2015 23:26:37
KNO_3	60	63.3	0.3365	0.1537	0.2799	0.2486	0.8372	10/05/2015 16:45:07	10/16/2015 23:20:07

[iii] All salt dissolved.

Salt	Temperature		Moisture Content		Area		V/V0	Time	
	Target	Measured	Initial	Final	Initial	Final		Loaded	Removed
KNO_3	60	63.3	0.3447	0.1072	0.314	0.2641	0.7714	10/05/2015 16:47:49	10/16/2015 23:25:13
KNO_3	60	63.3	0.3395	0.1404	0.358	0.3158	0.8286	10/05/2015 16:50:41	10/16/2015 23:19:13
K_2CO_3	60	63.3	0.3318	0.0755	0.2902	0.256	0.8284	10/05/2015 16:54:37	10/16/2015 23:27:37
K_2CO_3	60	63.3	0.3322	0.0749	0.2953	0.2599	0.8258	10/05/2015 16:57:10	10/16/2015 23:18:21
K_2CO_3	60	63.3	0.3084	0.0764	0.2778	0.2453	0.8298	10/05/2015 16:59:33	10/16/2015 23:15:42
K_2CO_3[ii]	60	63.3	0.334	0.0771	0.3844	0.3541	0.8839	10/05/2015 17:02:55	10/16/2015 23:23:13
$NaCl$[iv]	60	61.1						10/05/2015 17:18:10	
$NaCl$	60	61.1	0.3241	0.1441	0.4225	0.3787	0.8487	10/05/2015 17:20:51	10/16/2015 23:14:43
$NaCl$[iv]	60	61.1	0.3193	0.1409	0.3182	0.2876	0.8595	10/05/2015 17:23:15	10/16/2015 23:21:16
$NaCl$[iv]	60	61.1	0.32	0.141	0.3679	0.3313	0.8546	10/05/2015 17:25:40	10/16/2015 23:24:28
$LiCl$	60	61.1	0.302	0.0363	0.344	0.2966	0.8006	10/05/2015 17:28:19	10/16/2015 23:16:35
$LiCl$	60	61.1	0.2948	0.0377	0.3843	0.319	0.7563	10/05/2015 17:30:46	10/16/2015 23:28:44
$LiCl$	60	61.1	0.2973	0.0379	0.3543	0.3028	0.7901	10/05/2015 17:33:01	10/16/2015 23:25:53
$LiCl$	60	61.1						10/05/2015 17:35:05	
K_2SO_4	80	78.1	0.4082	0.3566	0.4018	0.353	0.8235	11/05/2015 18:59:02	11/08/2015 21:24:38
K_2SO_4[iv]	80	78.1	0.3874	0.2471	0.4331	0.367	0.7799	11/05/2015 18:58:00	11/08/2015 21:29:24
K_2SO_4	80	78.1	0.4215	0.2268	0.341	0.2915	0.79	11/05/2015 18:56:27	11/08/2015 21:31:15

[iv]Salt solution dried out.

Salt	Temperature		Moisture Content		Area		V/V0	Time	
	Target	Measured	Initial	Final	Initial	Final		Loaded	Removed
K_2SO_4[iv]	80	78.1	0.3972	0.0641	0.5043	0.381	0.6566	11/05/2015 18:54:55	11/08/2015 21:23:02
KNO_3[iv]	80	78.1	0.3878	0.0218	0.5923	0.4324	0.6237	11/05/2015 18:53:20	11/08/2015 21:21:05
KNO_3[iv]	80	78.1	0.4252	0.1597	0.391	0.2939	0.6518	11/05/2015 18:51:55	11/08/2015 21:19:28
KNO_3[iv]	80	78.1	0.398	0.2437	0.4651	0.3732	0.7187	11/05/2015 18:50:29	11/08/2015 21:29:37
KNO_3[iii]	80	78.1	0.407	0.1444	0.5426	0.4285	0.7016	11/05/2015 18:49:08	11/08/2015 21:33:01
K_2CO_3	80	80.7	0.4054	0.1028	0.5379	0.4325	0.7209	11/05/2015 18:47:30	11/08/2015 21:08:53
K_2CO_3	80	80.7	0.4098	0.0807	0.3703	0.2852	0.676	11/05/2015 18:46:11	11/08/2015 20:53:59
K_2CO_3	80	80.7	0.4029	0.1072	0.3188	0.2577	0.7267	11/05/2015 18:44:33	11/08/2015 21:16:35
K_2CO_3	80	80.7	0.4136	0.073	0.4217	0.3381	0.7179	11/05/2015 18:42:50	11/08/2015 20:56:40
$NaCl$	80	80.7	0.4261	0.2641	0.386	0.3166	0.7428	11/05/2015 18:41:29	11/08/2015 21:12:29
$NaCl$	80	80.7	0.4198	0.1531	0.479	0.3919	0.7399	11/05/2015 18:40:06	11/08/2015 20:48:52
$NaCl$[iv]	80	80.7	0.4406	0.2643	0.3755	0.3035	0.7265	11/05/2015 18:38:42	11/08/2015 21:14:37
$NaCl$	80	80.7	0.3666	0.1864	0.4776	0.3858	0.7261	11/05/2015 18:37:26	11/08/2015 21:00:38
$LiCl$	80	80.7	0.4409	0.0434	0.5164	0.3969	0.6738	11/05/2015 18:36:04	11/08/2015 21:04:53
$LiCl$	80	80.7	0.4473	0.0466	0.3226	0.2531	0.6949	11/05/2015 18:34:39	11/08/2015 21:10:28
$LiCl$	80	80.7	0.4577	0.0482	0.4213	0.3277	0.6862	11/05/2015 18:32:55	11/08/2015 21:02:29
$LiCl$	80	80.7	0.468	0.0446	0.349	0.2729	0.6912	11/05/2015 18:31:23	11/08/2015 21:06:53

Table B.4.

Freeze drying data.

Moisture Content		Area			
Initial $(d.b.)$	Final $(d.b.)$	Initial (in^2)	Final (in^2)	V/V0	Prefrozen?
0.4276	0.0575	0.5311	0.4467	0.7711	Yes
0.4191	0.0631	0.4555	0.3661	0.7205	Yes
0.4166	0.0691	0.3902	0.3237	0.7557	Yes
0.4400	0.0766	0.4095	0.3251	0.7074	Yes
0.4349	0.0639	0.4102	0.3504	0.7895	Yes
0.4425	0.0593	0.4857	0.3975	0.7404	Yes
0.4362	0.0614	0.4796	0.3867	0.7241	Yes
0.4567	0.0799	0.4385	0.3633	0.7540	Yes
0.4425	0.0595	0.4524	0.3671	0.7310	Yes
0.4513	0.0550	0.4286	0.3596	0.7684	Yes
0.4420	0.0437	0.2943	0.2443	0.7561	No
0.4601	0.0403	0.4044	0.3380	0.7641	No
0.4645	0.0523	0.3321	0.2689	0.7287	No
0.4552	0.0388	0.2950	0.2381	0.7254	No
0.4505	0.0378	0.2708	0.2289	0.7769	No
0.4528	0.0440	0.2867	0.2315	0.7256	No
0.4620	0.0373	0.3745	0.3092	0.7499	No
0.4519	0.0387	0.3559	0.2845	0.7146	No
0.4557	0.0340	0.3407	0.2832	0.7577	No

C. ISOTHERM DATA

Table C.1.: Table of moisture content, temperature, and relative humidity used to calculate isotherm parameters. The relative humidities were calculated using the regression equations from Table 3.2 (Greenspan, 1977).

Salt	Temperature °C	Moisture Content $\frac{\text{kg}}{\text{kg}_{\text{db}}}$	Relative Humidity -
K_2SO_4	43.2	0.3963	0.9623
K_2SO_4	43.2	0.3958	0.9623
K_2SO_4	43.2	0.3624	0.9623
KNO_3	43.2	0.2227	0.8778
KNO_3	43.2	0.2288	0.8778
KNO_3	43.2	0.2181	0.8778
KNO_3	43.2	0.2301	0.8778
K_2CO_3	49.3	0.1029	0.4306
K_2CO_3	49.3	0.1014	0.4306
K_2CO_3	49.3	0.1015	0.4306
$NaCl$	49.3	0.1519	0.7444
$NaCl$	49.3	0.1584	0.7444
$NaCl$	49.3	0.1577	0.7444
$LiCl$	49.3	0.0649	0.1030
$LiCl$	49.3	0.0599	0.1030
$LiCl$	49.3	0.0707	0.1030
$LiCl$	49.3	0.0648	0.1030
K_2CO_3	42.6	0.1047	0.4307

Salt	Temperature	Moisture Content	Relative Humidity
K_2CO_3	42.6	0.1024	0.4307
K_2CO_3	42.6	0.0822	0.4307
K_2CO_3	42.6	0.0914	0.4307
$NaCl$	42.6	0.1521	0.7460
$NaCl$	42.6	0.1550	0.7460
$NaCl$	42.6	0.1445	0.7460
K_2SO_4	63.3	0.3413	0.9504
K_2SO_4	63.3	0.3307	0.9504
K_2SO_4	63.3	0.3417	0.9504
K_2CO_3	63.3	0.0755	0.4304
K_2CO_3	63.3	0.0749	0.4304
K_2CO_3	63.3	0.0764	0.4304
$NaCl$	61.1	0.1441	0.7454
$LiCl$	61.1	0.0363	0.099 26
$LiCl$	61.1	0.0377	0.099 26
$LiCl$	61.1	0.0379	0.099 26
K_2SO_4	78.1	0.3566	0.9417
K_2SO_4	78.1	0.2268	0.9417
K_2CO_3	80.7	0.1028	0.4301
K_2CO_3	80.7	0.0807	0.4301
K_2CO_3	80.7	0.1072	0.4301
K_2CO_3	80.7	0.0730	0.4301
$NaCl$	80.7	0.2641	0.7641
$NaCl$	80.7	0.1531	0.7641
$NaCl$	80.7	0.1864	0.7641
$LiCl$	80.7	0.0434	0.091 68
$LiCl$	80.7	0.0466	0.091 68
$LiCl$	80.7	0.0482	0.091 68

Salt	Temperature	Moisture Content	Relative Humidity
LiCl	80.7	0.0446	0.091 68

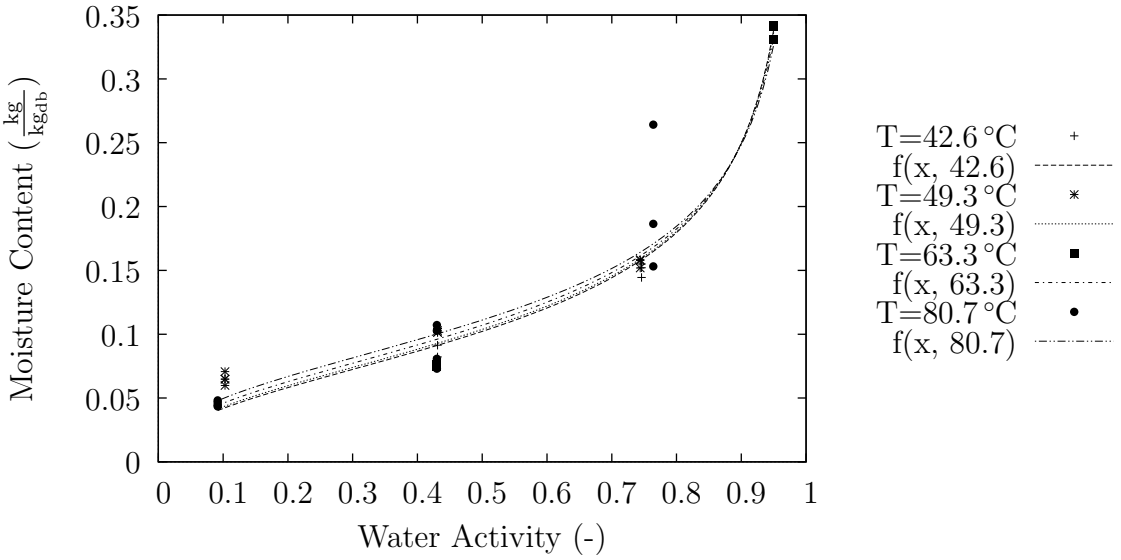

Fig. C.1. Isotherm data (part 1 of 2)

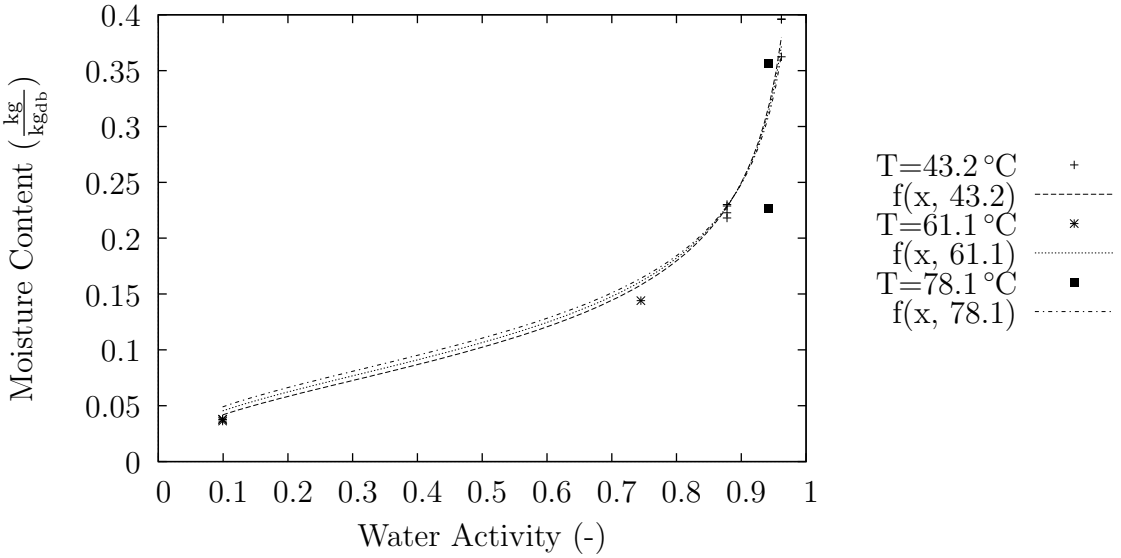

Fig. C.2. Isotherm data (part 2 of 2)

D. EXPERIMENTAL GRAPHS

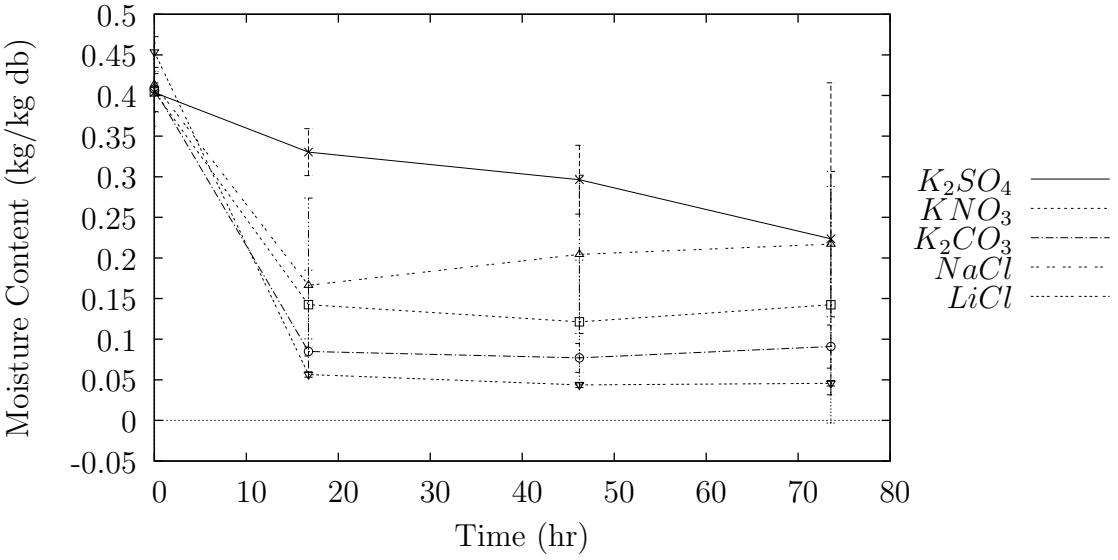

Fig. D.1. Drying curves for samples at 80°C. Error bars represent a 95% confidence interval

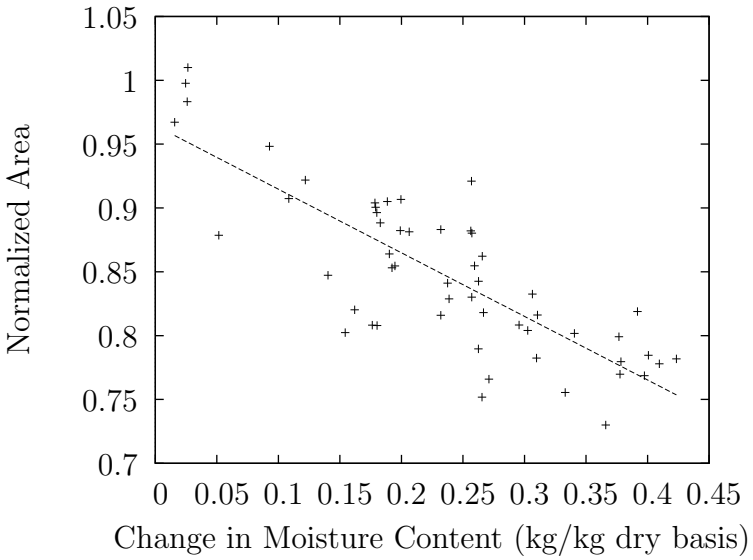

Fig. D.2. Moisture content vs. normalized area for all temperatures.

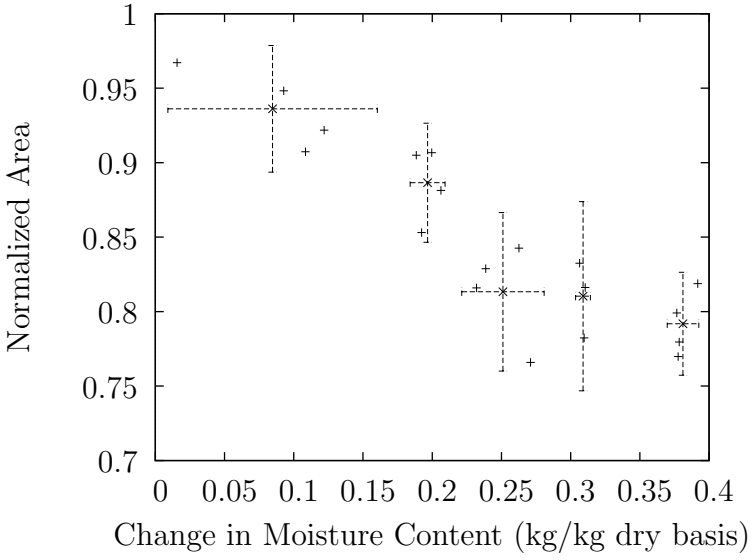

Fig. D.3. Moisture content vs. normalized area T=40°C.

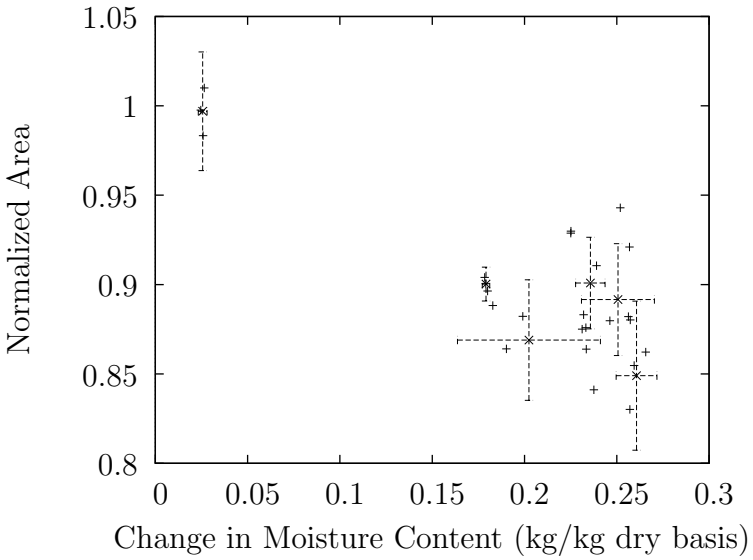

Fig. D.4. Moisture content vs. normalized area T=60°C.

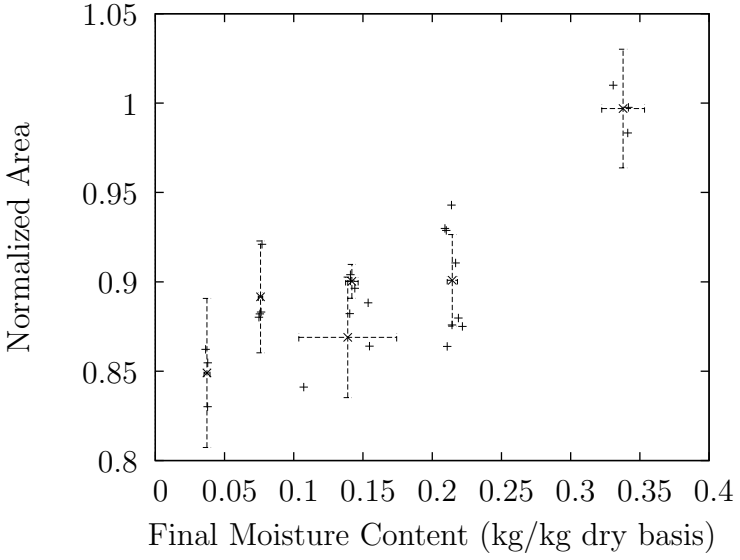

Fig. D.5. Moisture content vs. normalized area T=60°C.

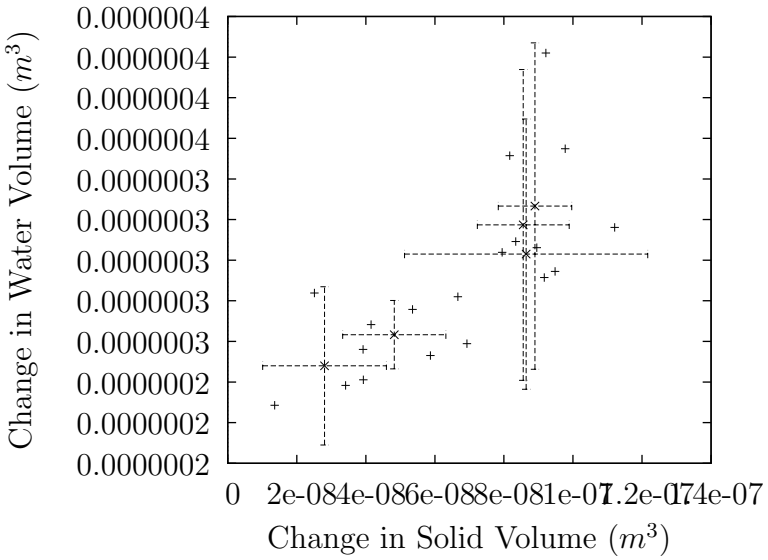

Fig. D.6. Change in volume of solid vs change in volume of water at 40°C.

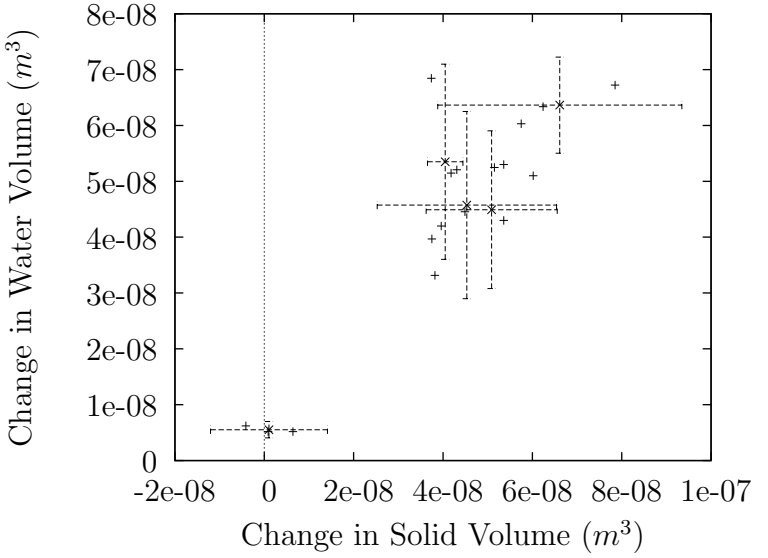

Fig. D.7. Change in volume of solid vs change in volume of water at 60°C.

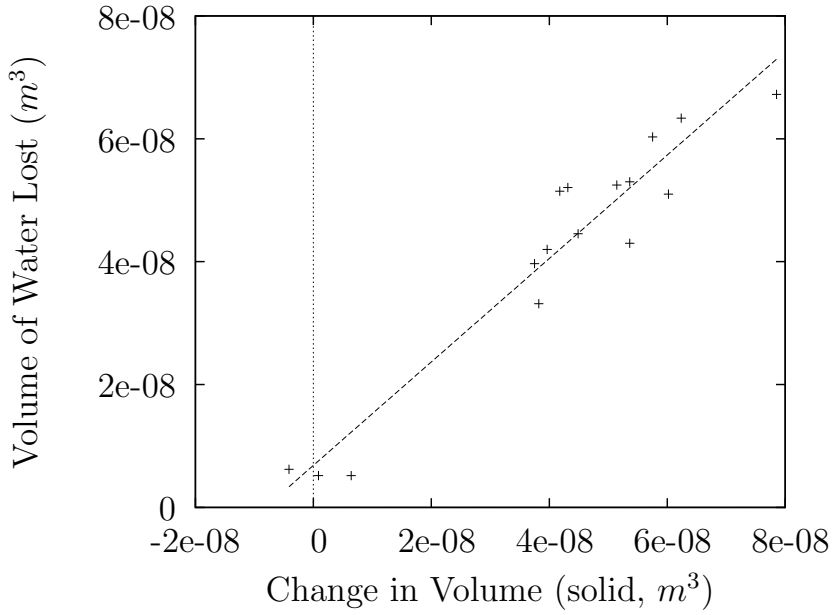

Fig. D.8. Volume loss of water as a function of decrease in volume of the solid matrix. $y = 0.8266x + 9.244 \times 10^{-9}$, $R^2 = 0.8013$.

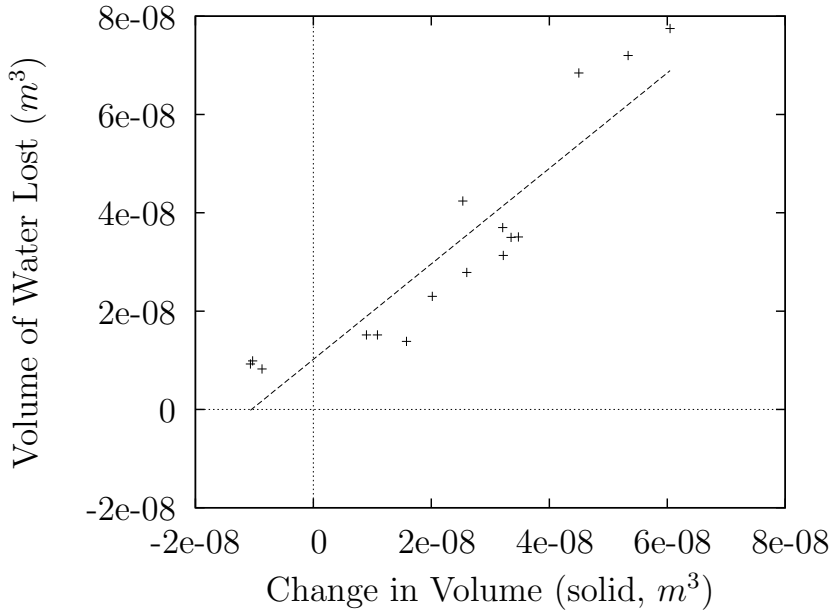

Fig. D.9. Volume loss of water as a function of decrease in volume of the solid matrix when drying at 90°C. $y = 0.9475x + 1.121 \times 10^{-8}$, $R^2 = 0.8368$.

E. PLOTS OF MODEL INPUT

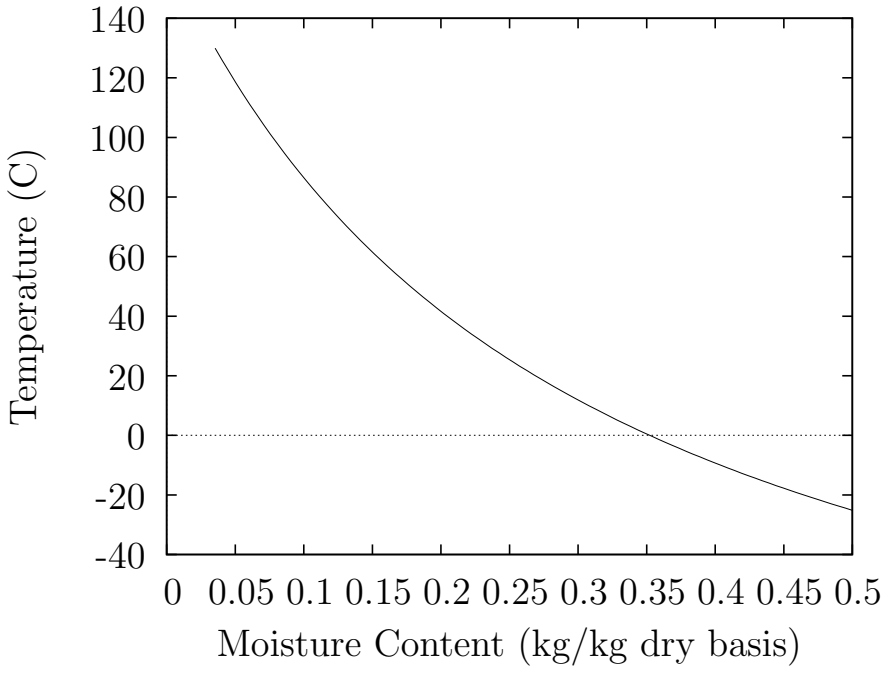

Fig. E.1. Glass transition temperature

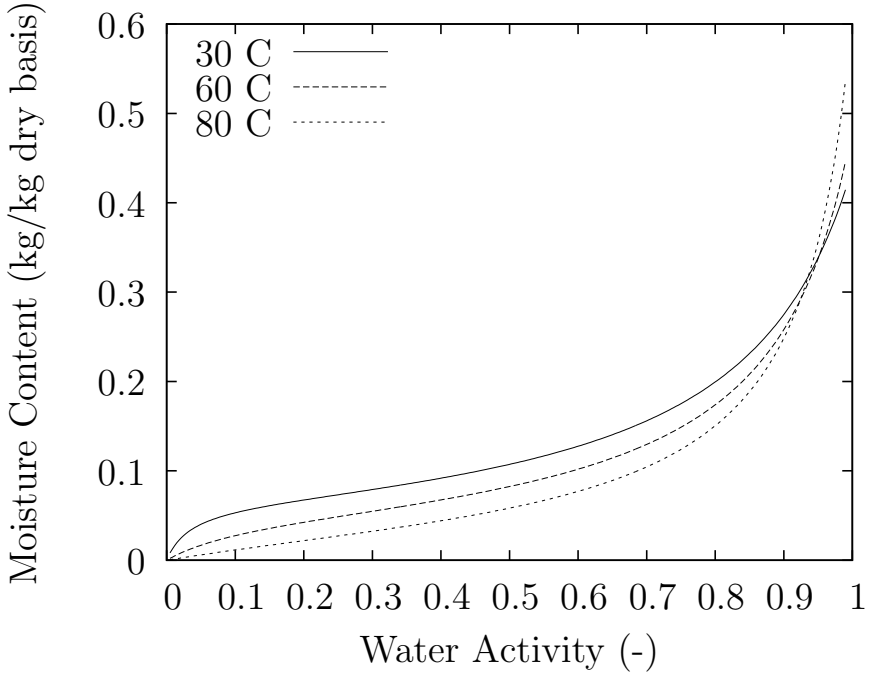

Fig. E.2. Isotherm data for durum semolina (GAB)

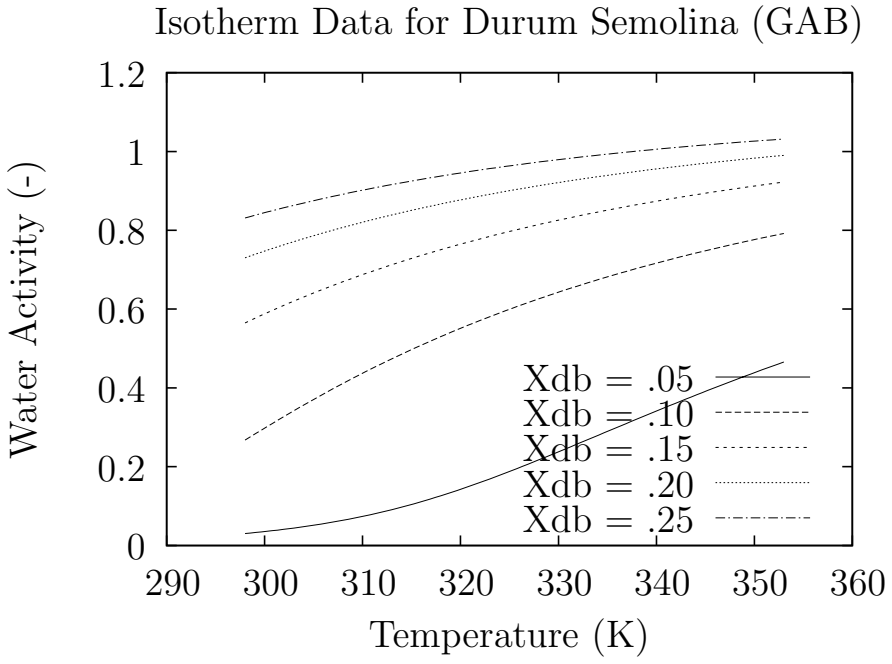

Fig. E.3. Isotherm data for durum semolina (GAB)

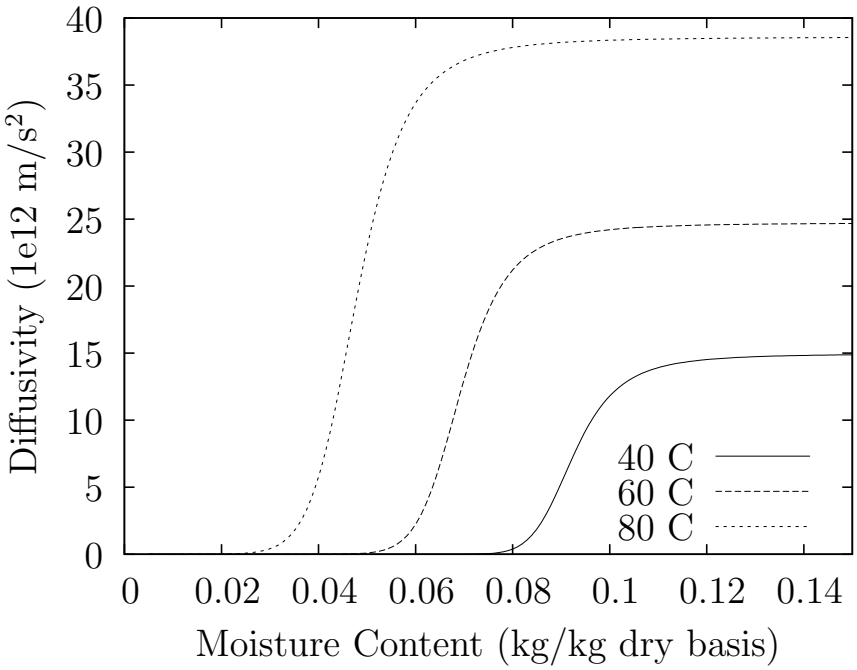

Fig. E.4. Effective diffusivity (GAB Isotherm)

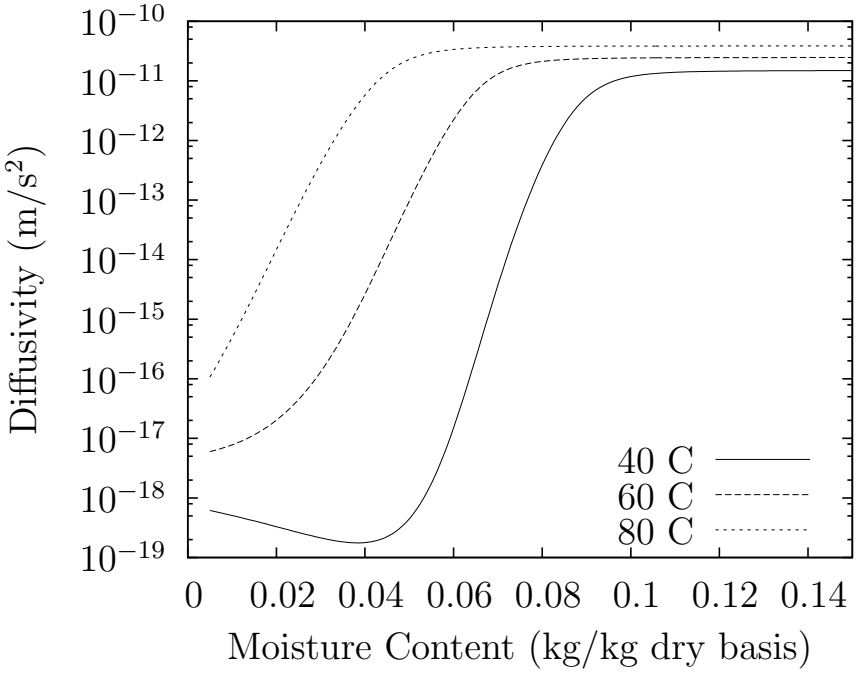

Fig. E.5. Effective diffusivity (GAB Isotherm)

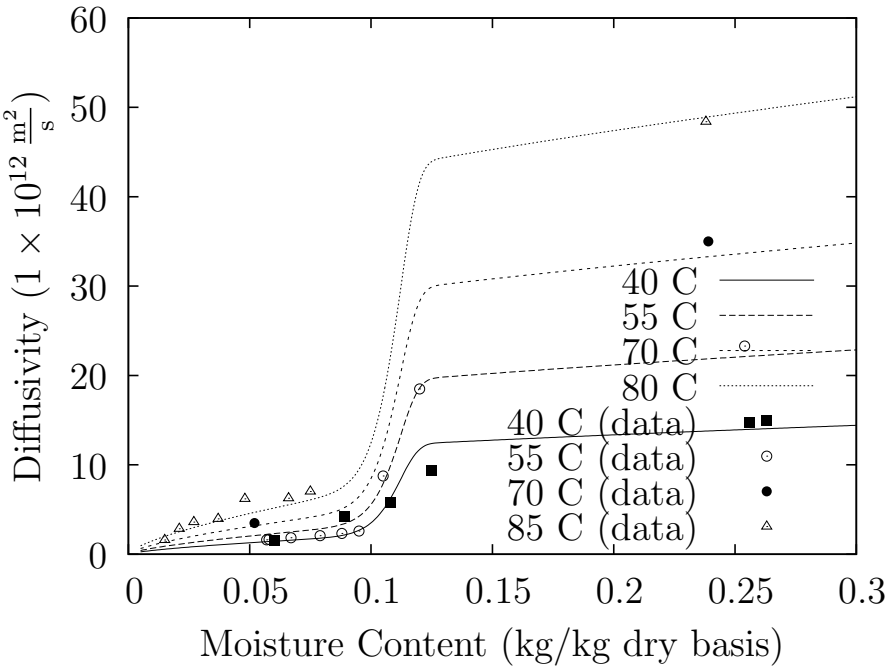

Fig. E.6. Effective diffusivity (Litchfield 1992)

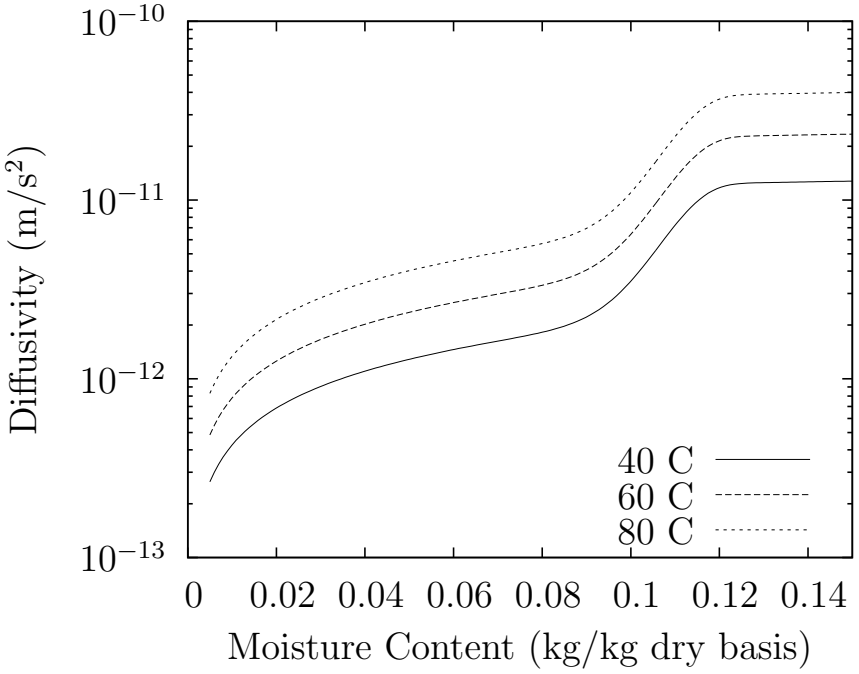

Fig. E.7. Effective diffusivity (Litchfield 1992)

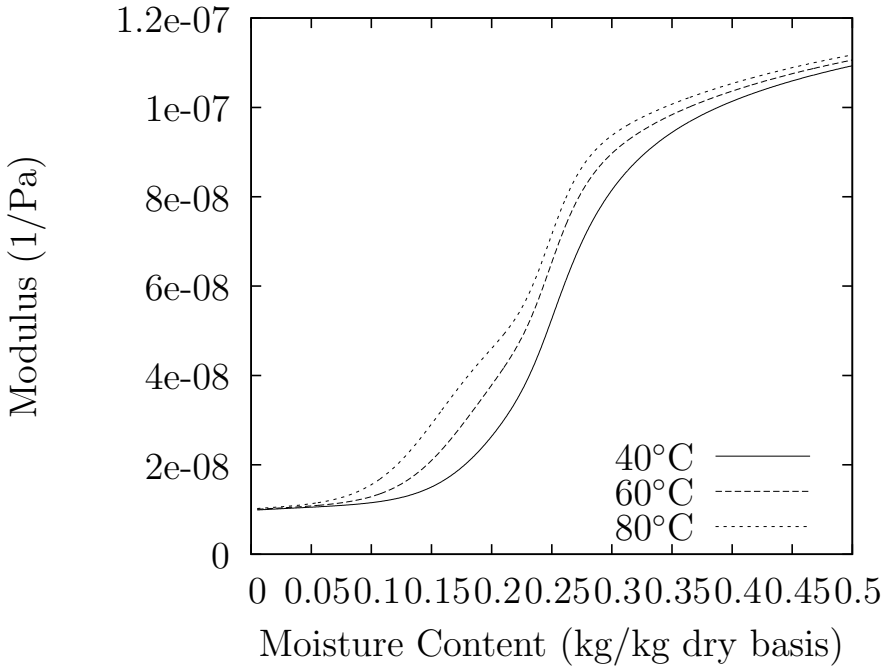

Fig. E.8. Creep compliance (J_0)

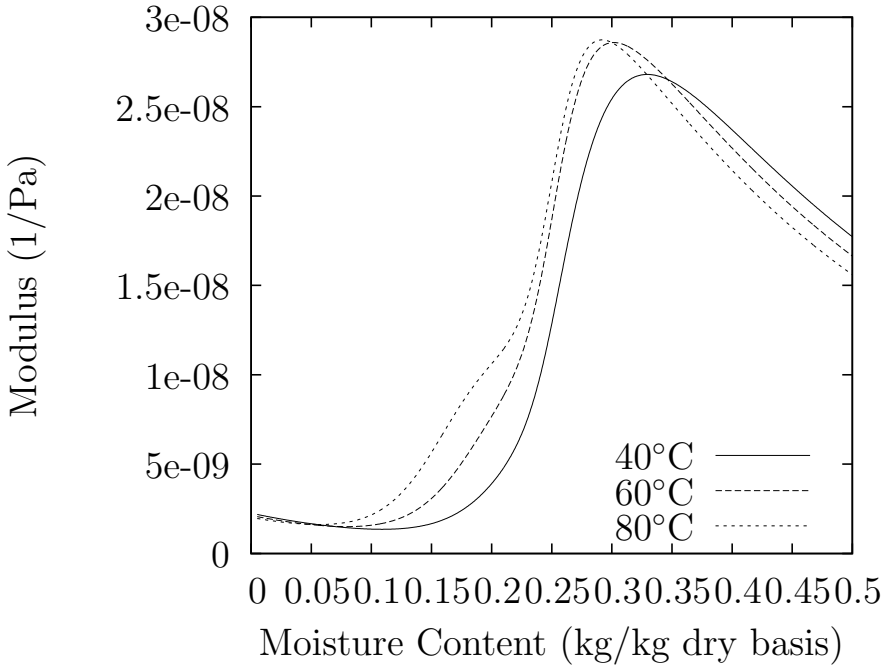

Fig. E.9. Creep compliance (J_1)

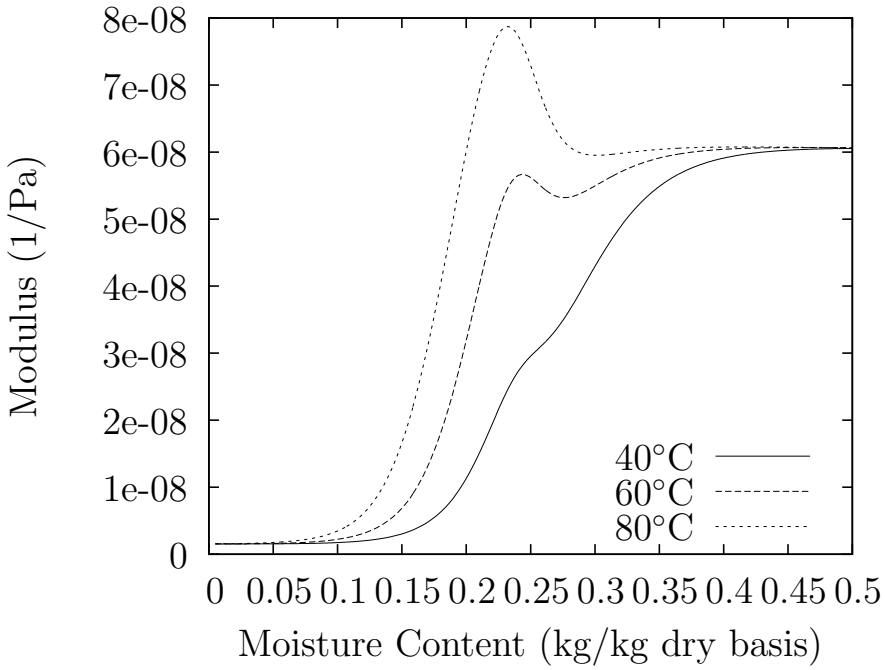

Fig. E.10. Creep compliance (J_2)

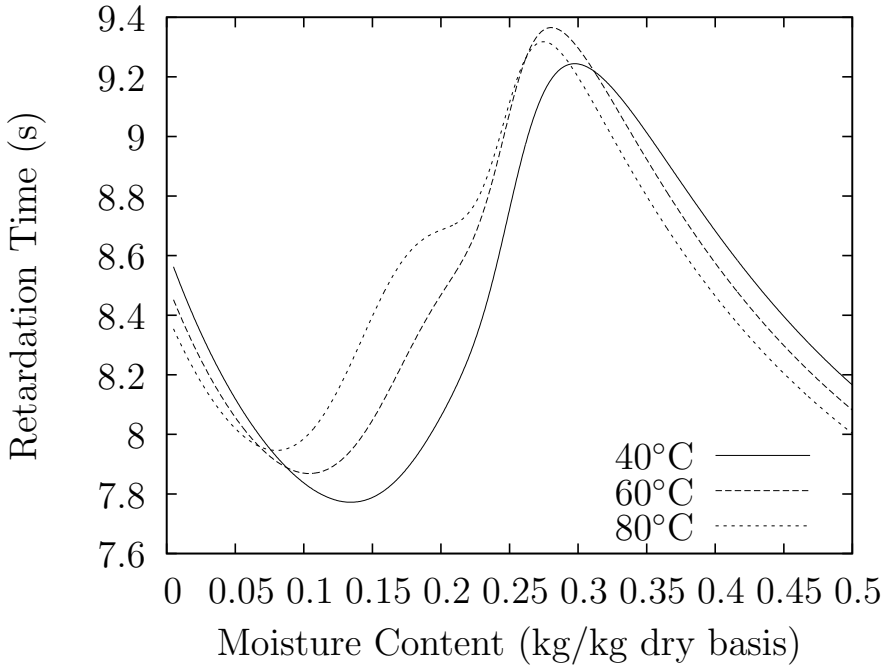

Fig. E.11. Creep compliance (τ_1)

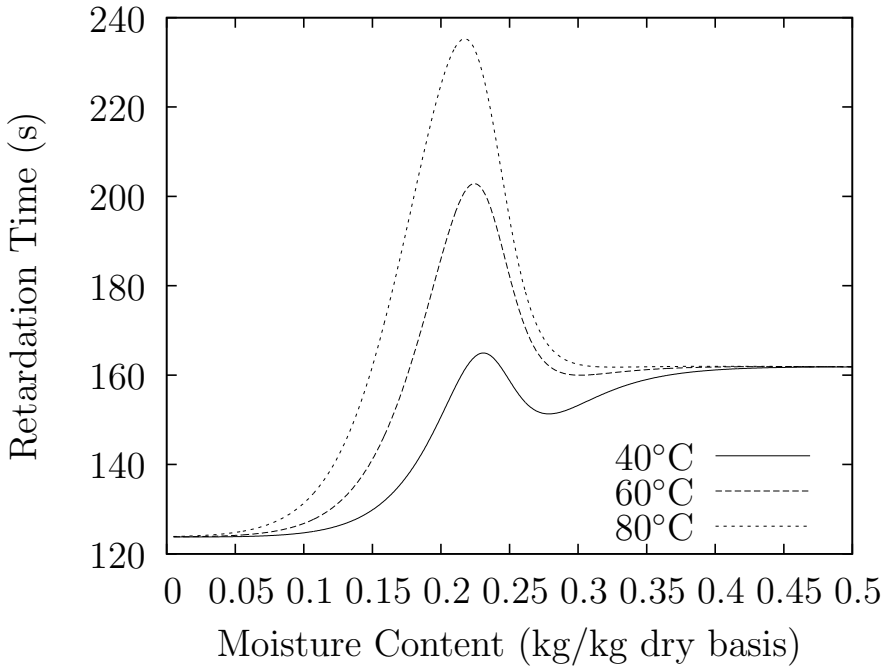

Fig. E.12. Creep compliance (τ_2)

F. SIMULATION GRAPHS

F.1 Drying Profiles

313K

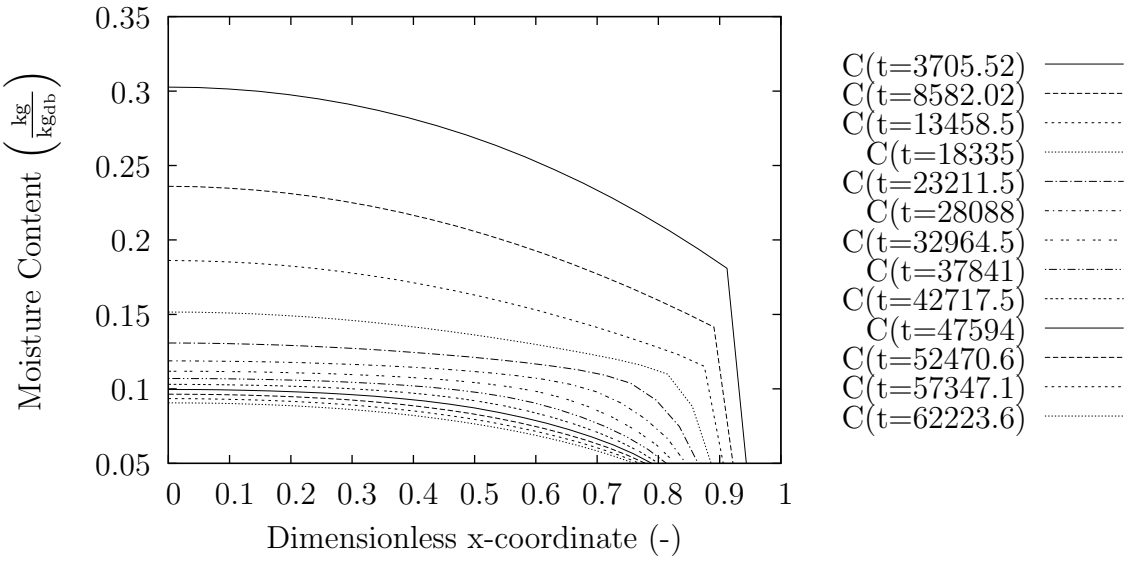

Fig. F.1. Moisture profiles. $X_e = 0.05$; T=313 K; D_{eff}: Eq. 2.71

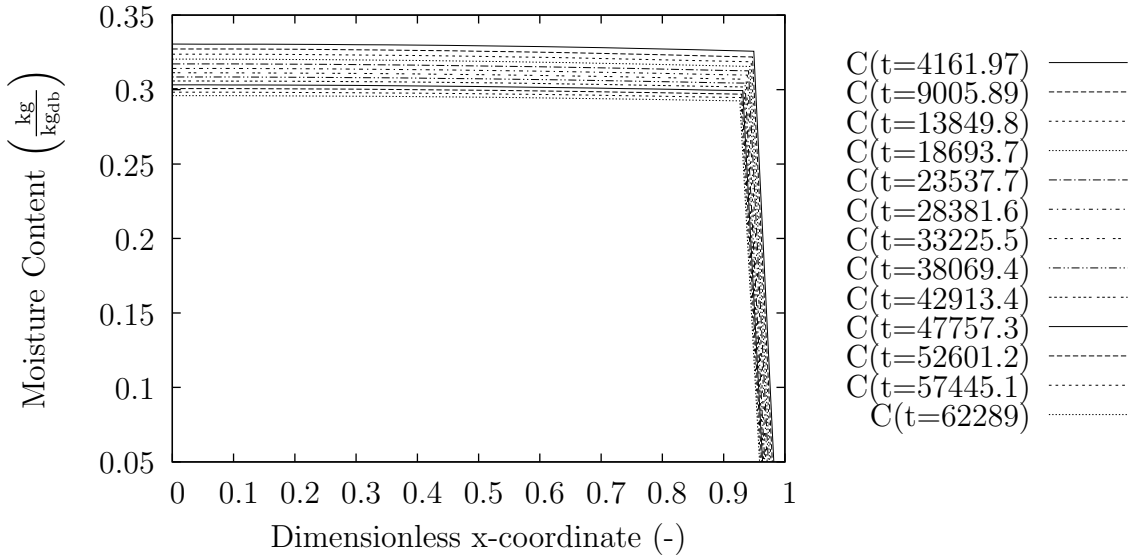

Fig. F.2. Moisture profiles. $X_e = 0.05$; T=313 K; D_{eff}: Eq. 2.73

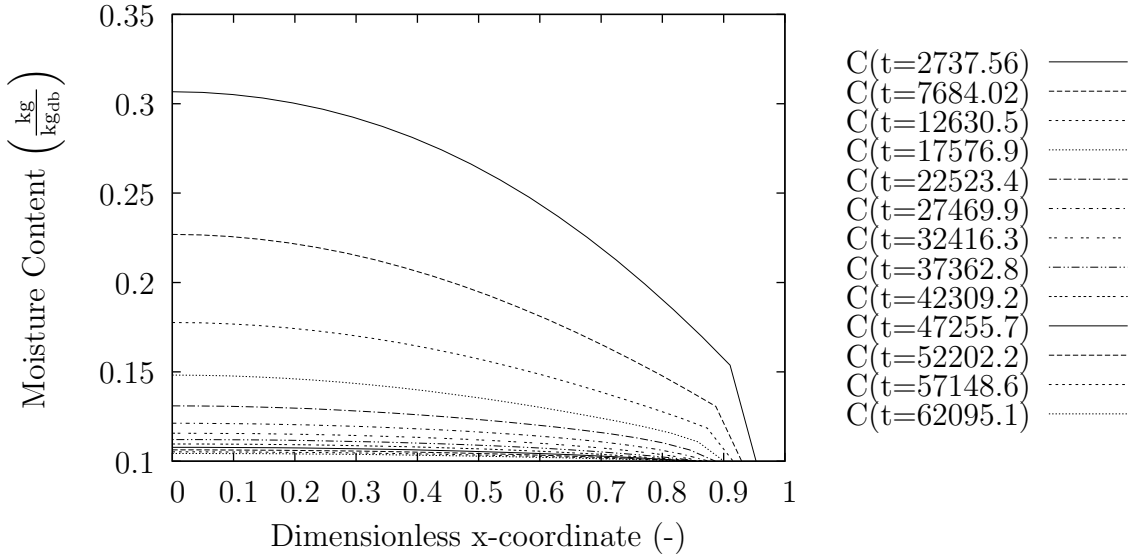

Fig. F.3. Moisture profiles. $X_e = 0.10$; T=313 K D_{eff}: Eq. 2.71

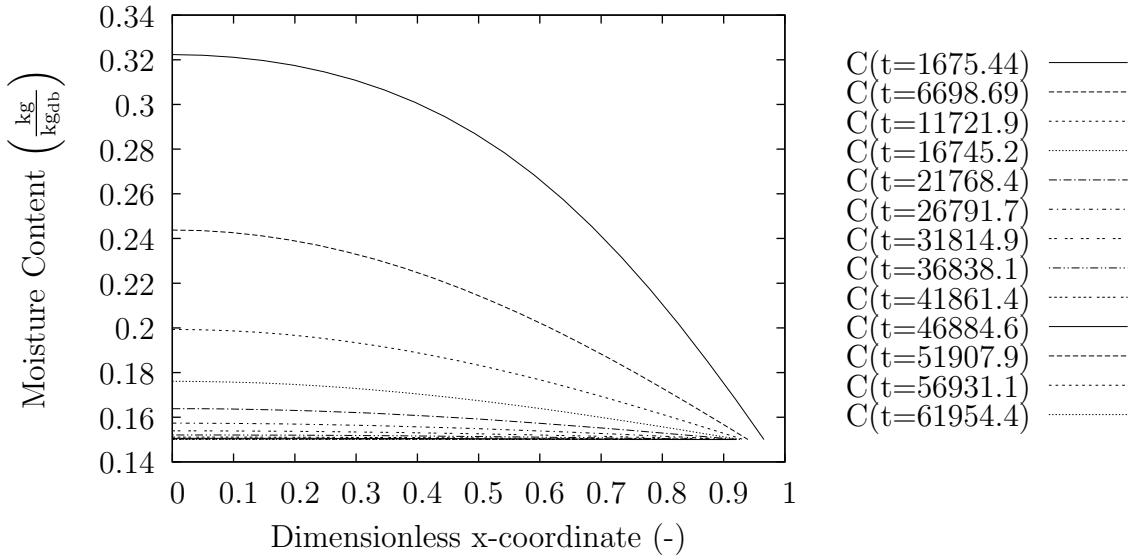

Fig. F.4. Moisture profiles. $X_e = 0.15$; T=313 K D_{eff}: Eq. 2.71

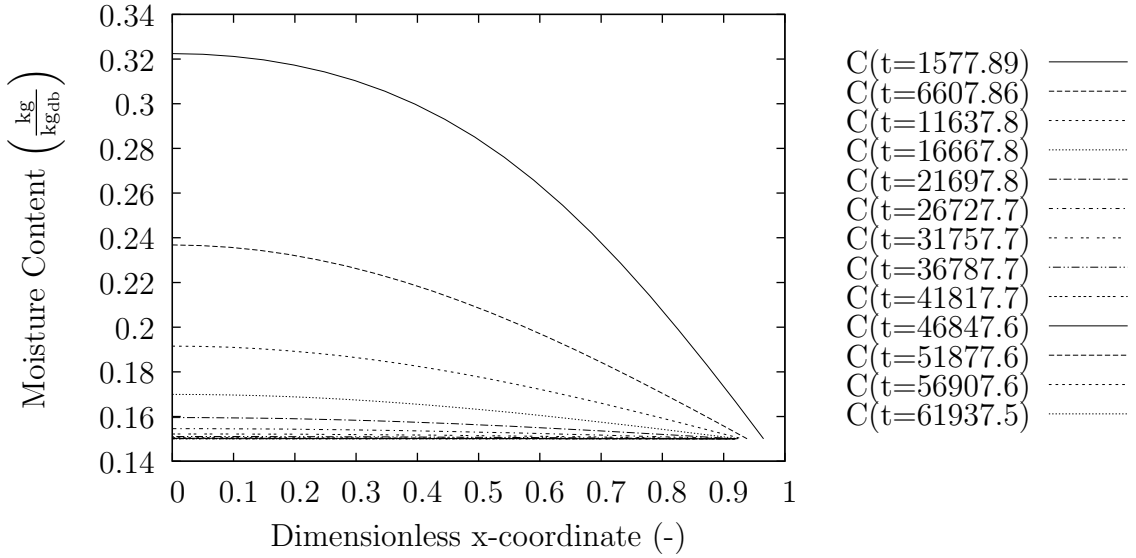

Fig. F.5. Moisture profiles. $X_e = 0.15$; T=313 K D_{eff}: Eq. 2.73

333K

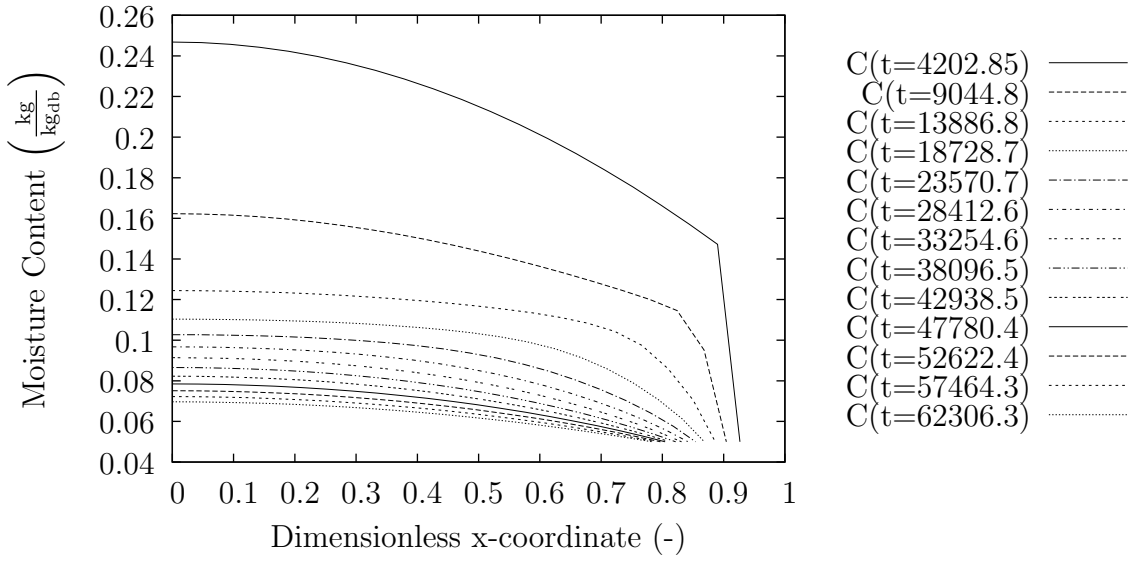

Fig. F.6. Moisture profiles. $X_e = 0.05$; T=333 K; D_{eff}: Eq. 2.71

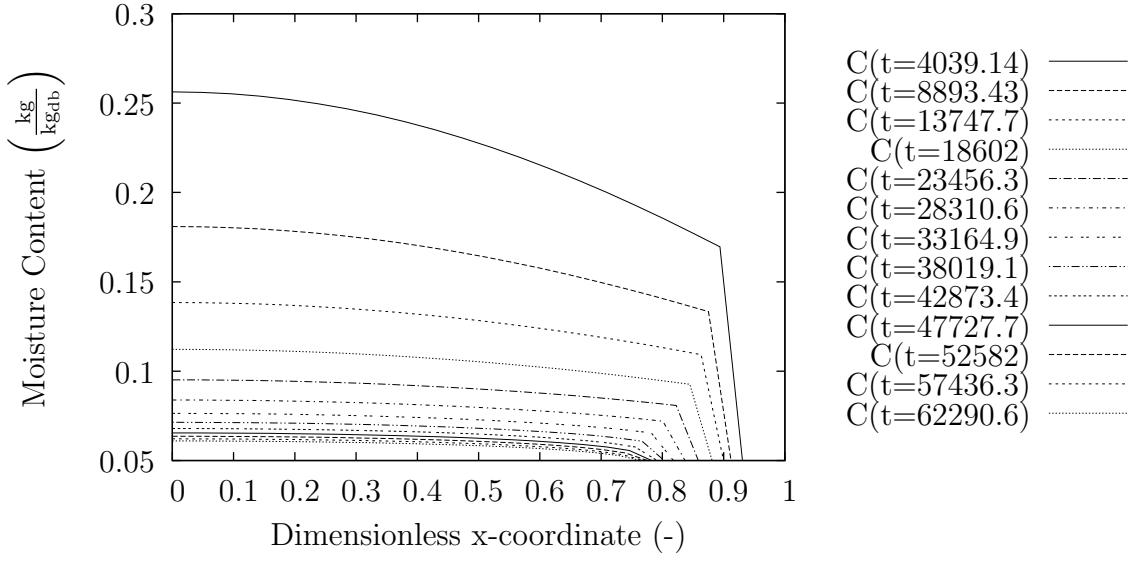

Fig. F.7. Moisture profiles. $X_e = 0.05$; T=333 K; D_{eff}: Eq. 2.73

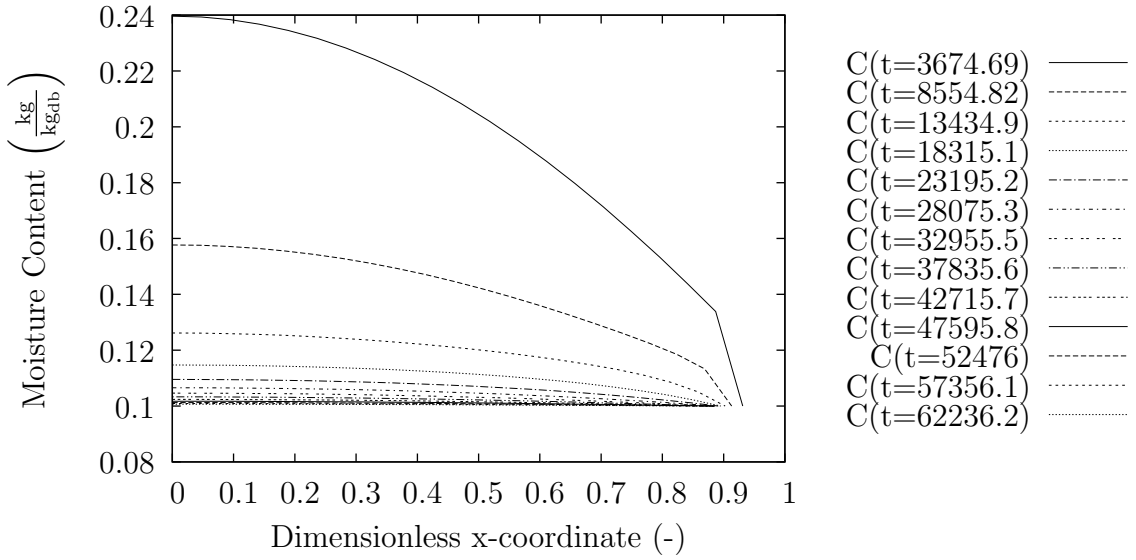

Fig. F.8. Moisture profiles. $X_e = 0.10$; T=333 K D_{eff}: Eq. 2.71

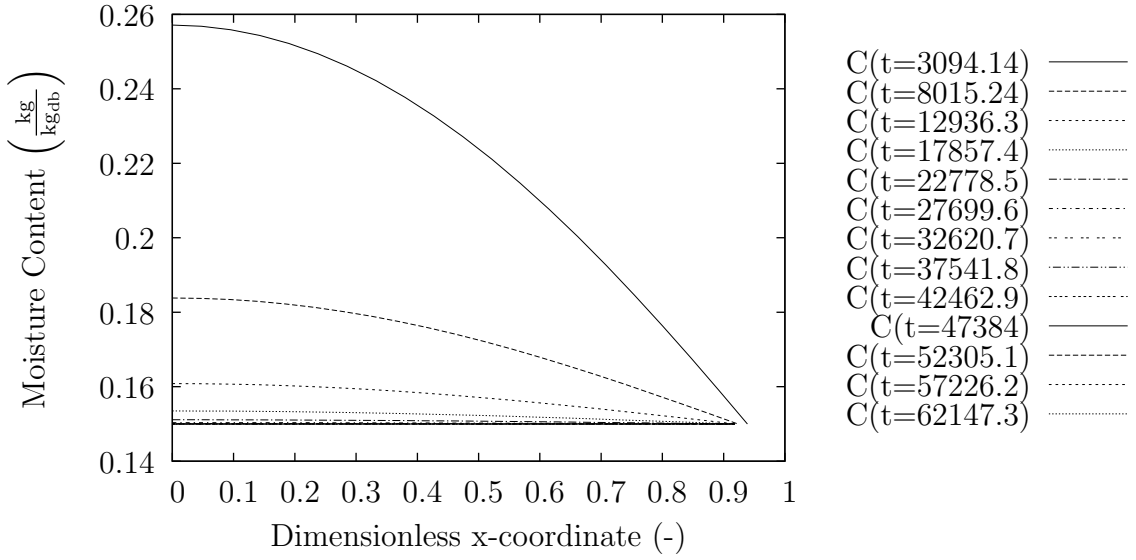

Fig. F.9. Moisture profiles. $X_e = 0.15$; T=333 K D_{eff}: Eq. 2.71

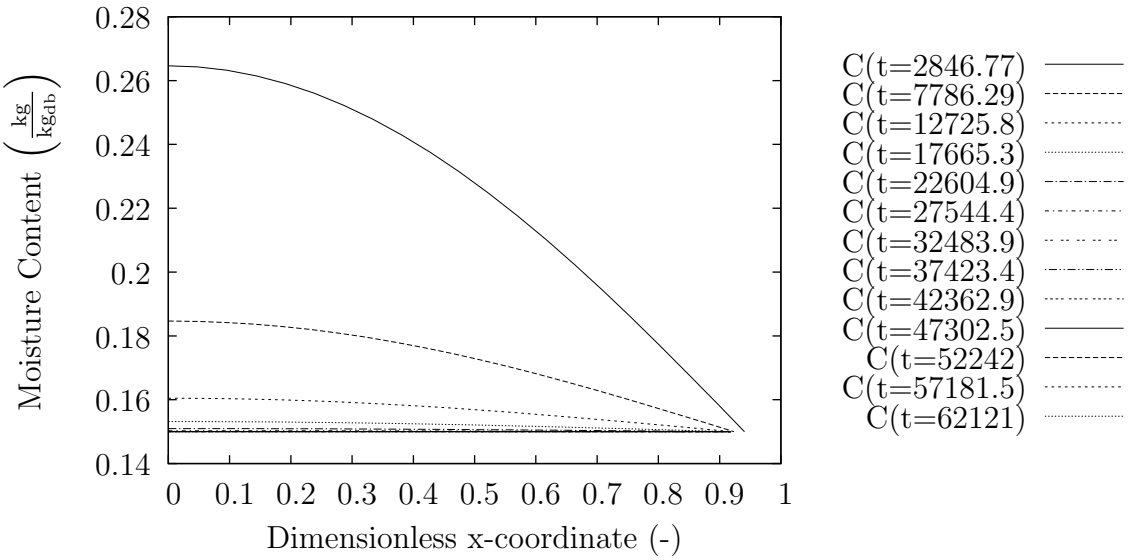

Fig. F.10. Moisture profiles. $X_e = 0.15$; T=333 K D_{eff}: Eq. 2.73

353K

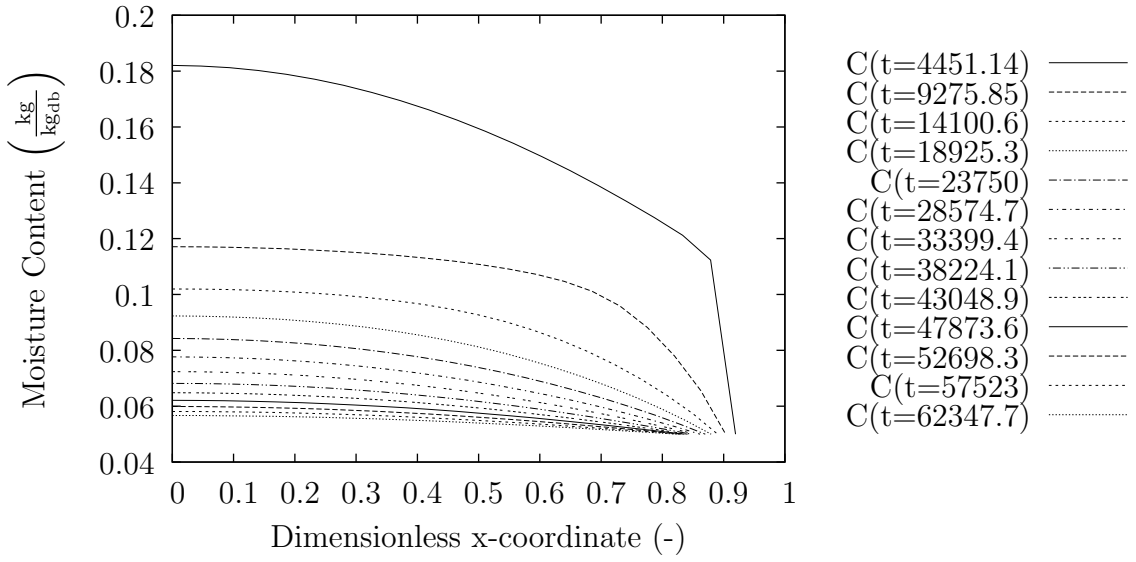

Fig. F.11. Moisture profiles. $X_e = 0.05$; T=353 K; D_{eff}: Eq. 2.71

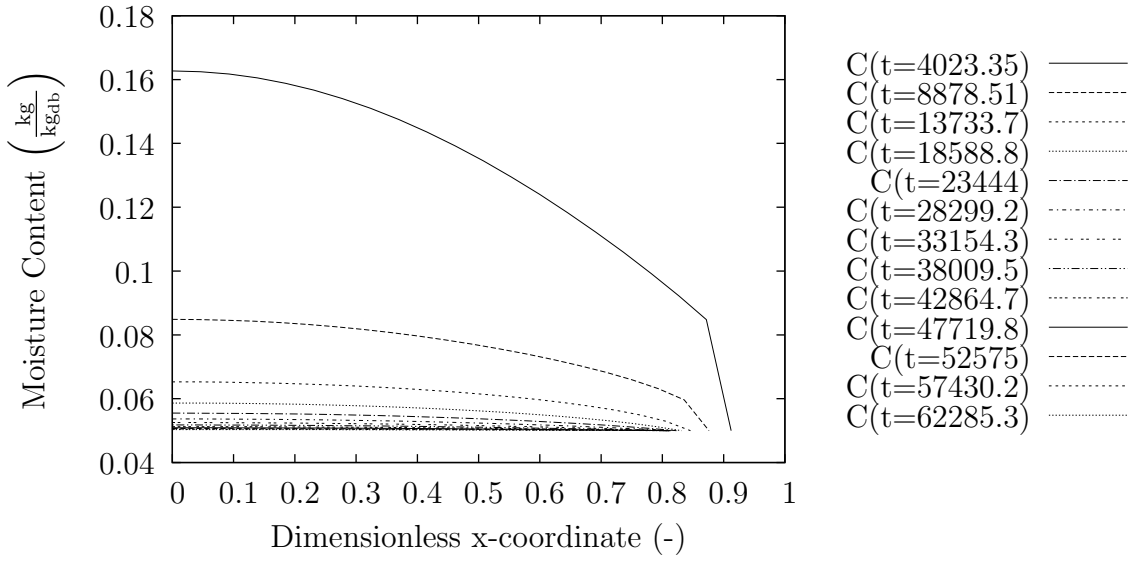

Fig. F.12. Moisture profiles. $X_e = 0.05$; T=353 K; D_{eff}: Eq. 2.73

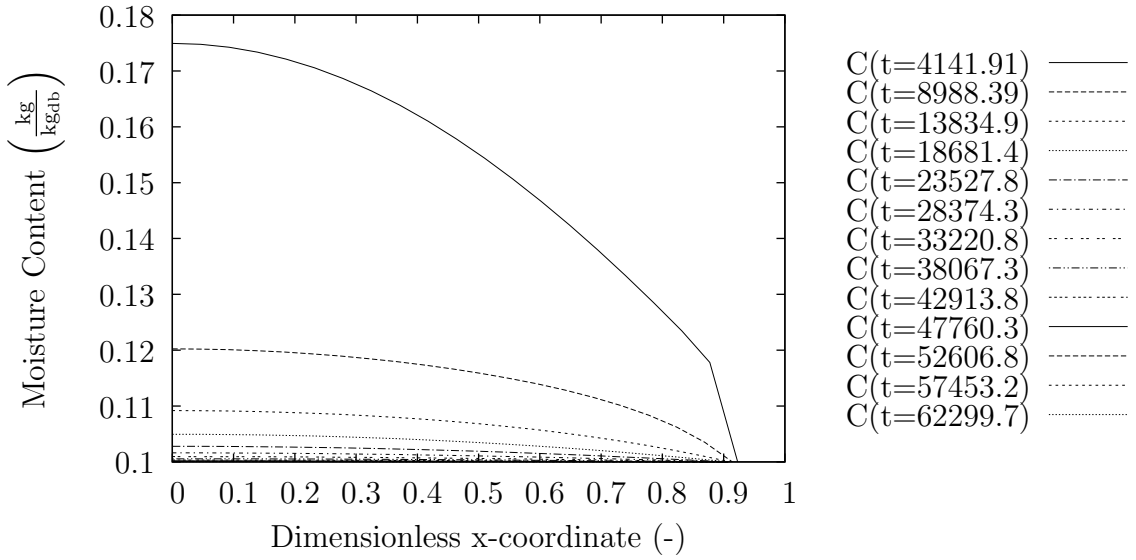

Fig. F.13. Moisture profiles. $X_e = 0.10$; T=353 K D_{eff}: Eq. 2.71

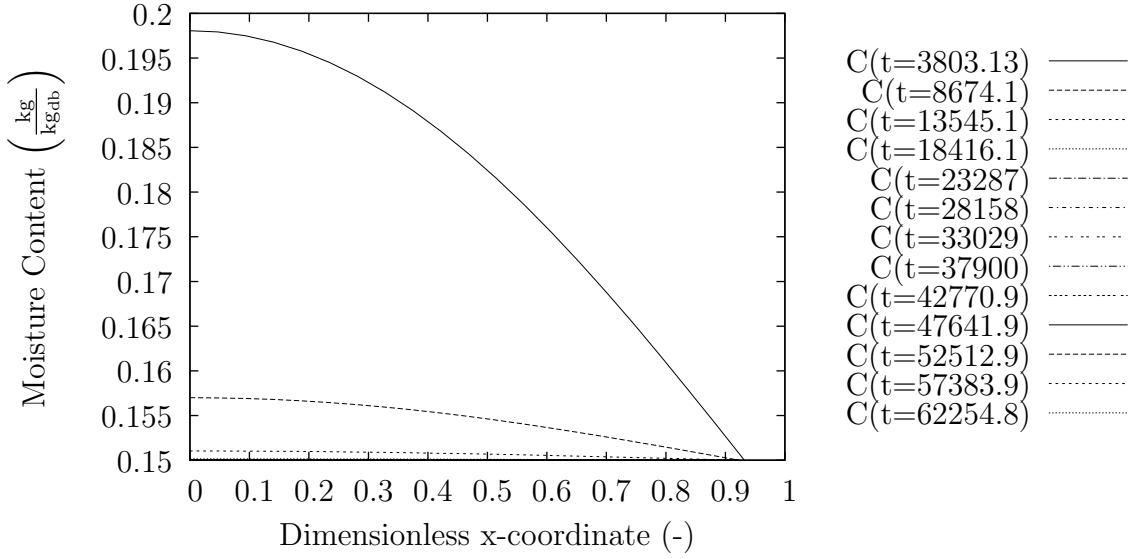

Fig. F.14. Moisture profiles. $X_e = 0.15$; T=353 K D_{eff}: Eq. 2.71

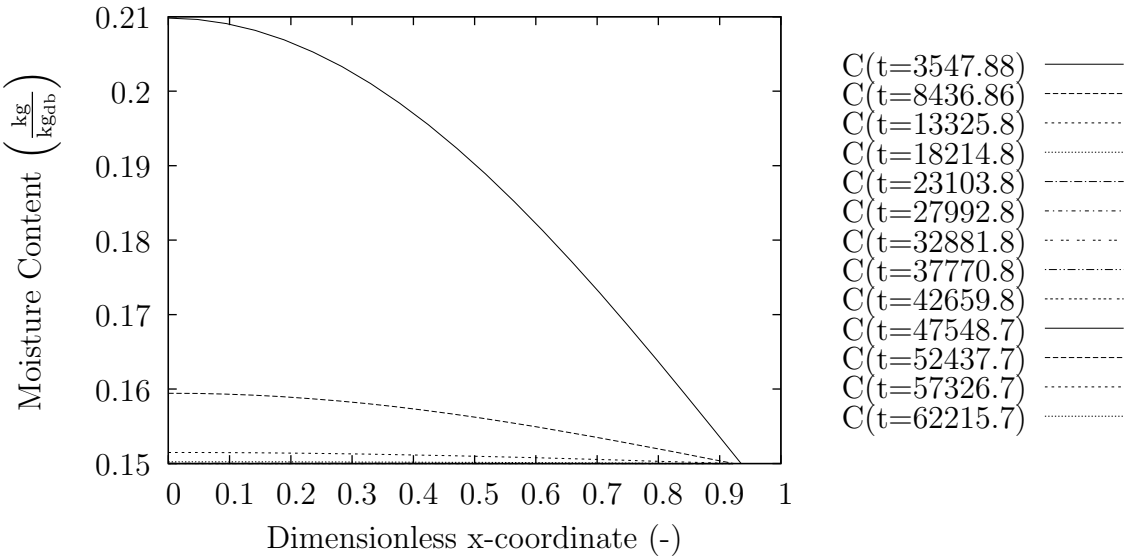

Fig. F.15. Moisture profiles. $X_e = 0.15$; T=353 K D_{eff}: Eq. 2.73

F.2 Shrinkage Curves

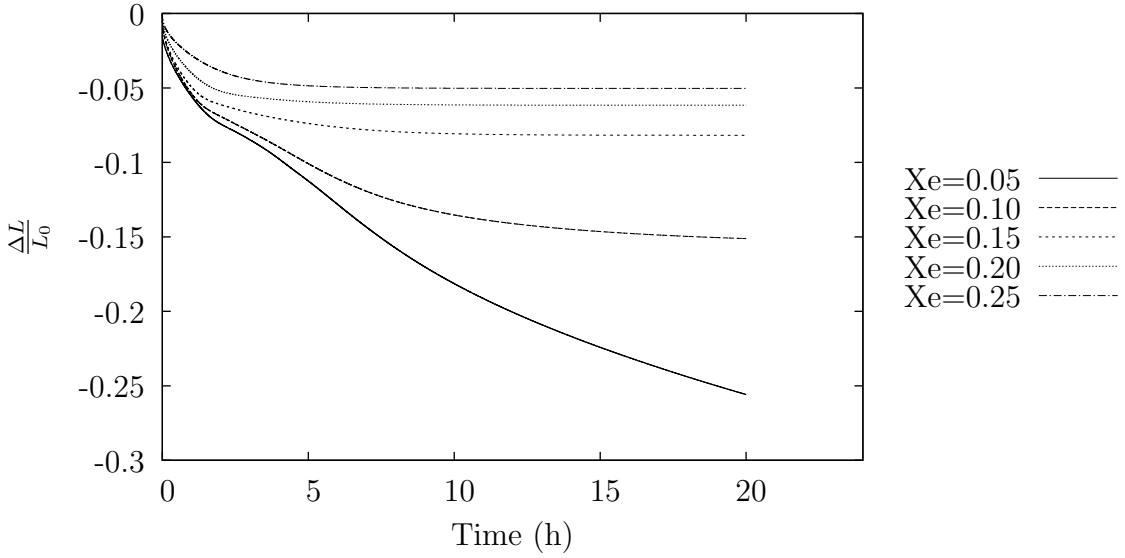

Fig. F.16. Shrinkage vs. Time. T=313 K D_{eff}: Eq. 2.71

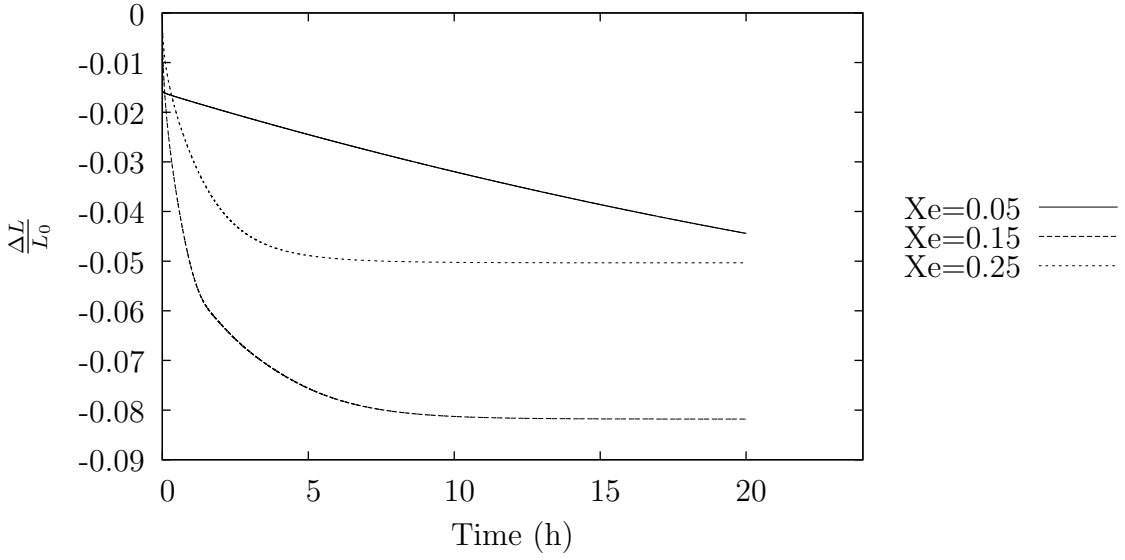

Fig. F.17. Shrinkage vs. Time. T=313 K D_{eff}: Eq. 2.73

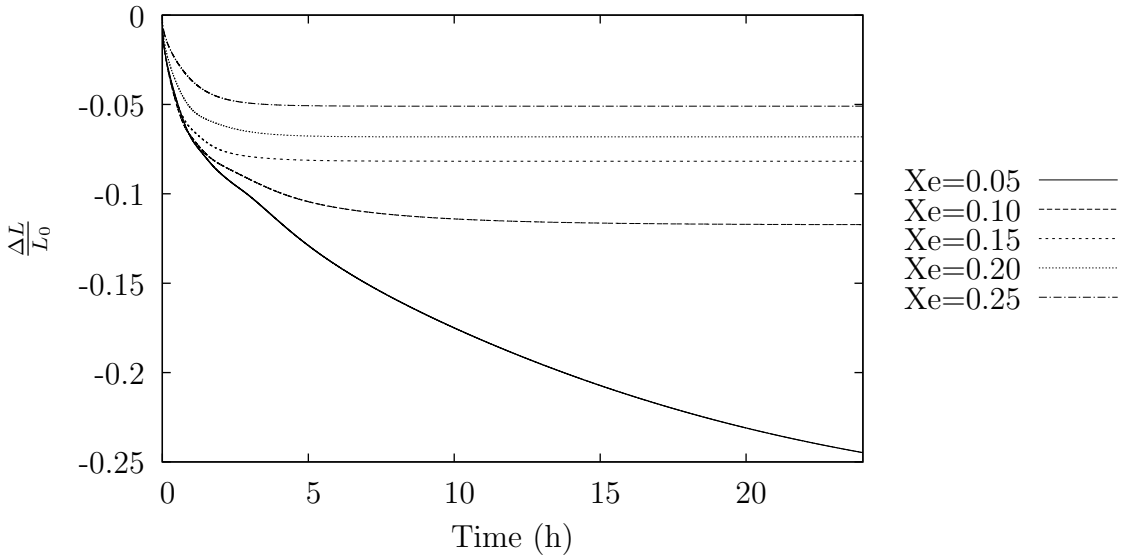

Fig. F.18. Shrinkage vs. Time. T=333 K D_{eff}: Eq. 2.71

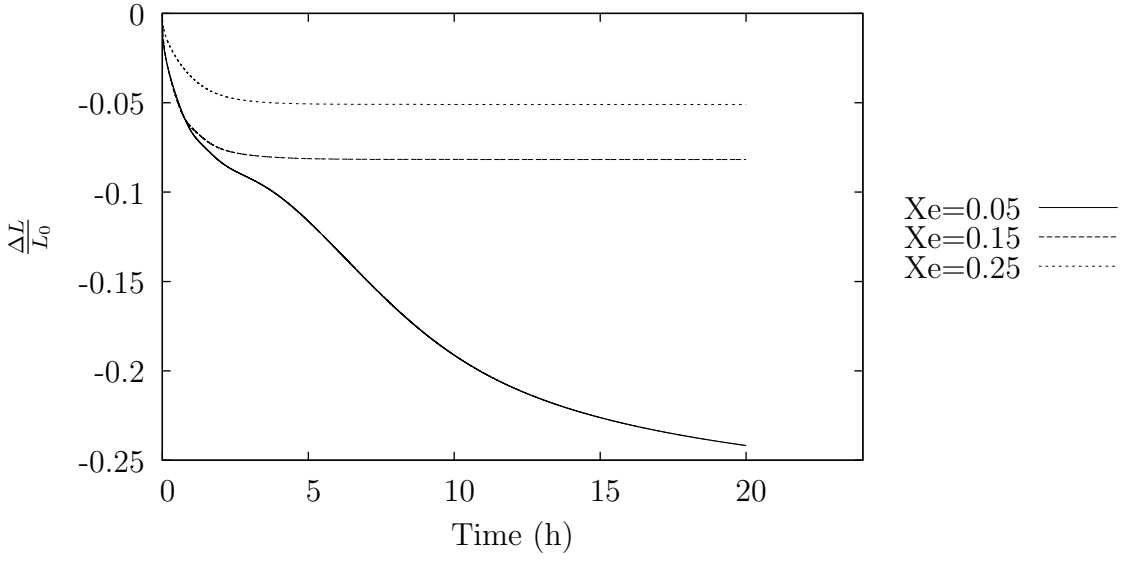

Fig. F.19. Shrinkage vs. Time. T=333 K D_{eff}: Eq. 2.73

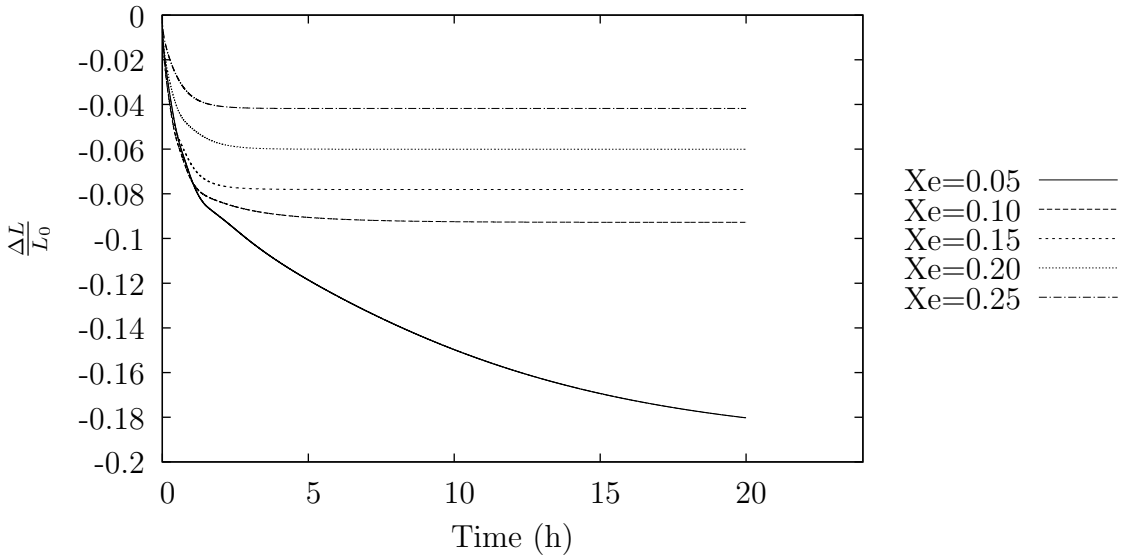

Fig. F.20. Shrinkage vs. Time. T=353 K D_{eff}: Eq. 2.71

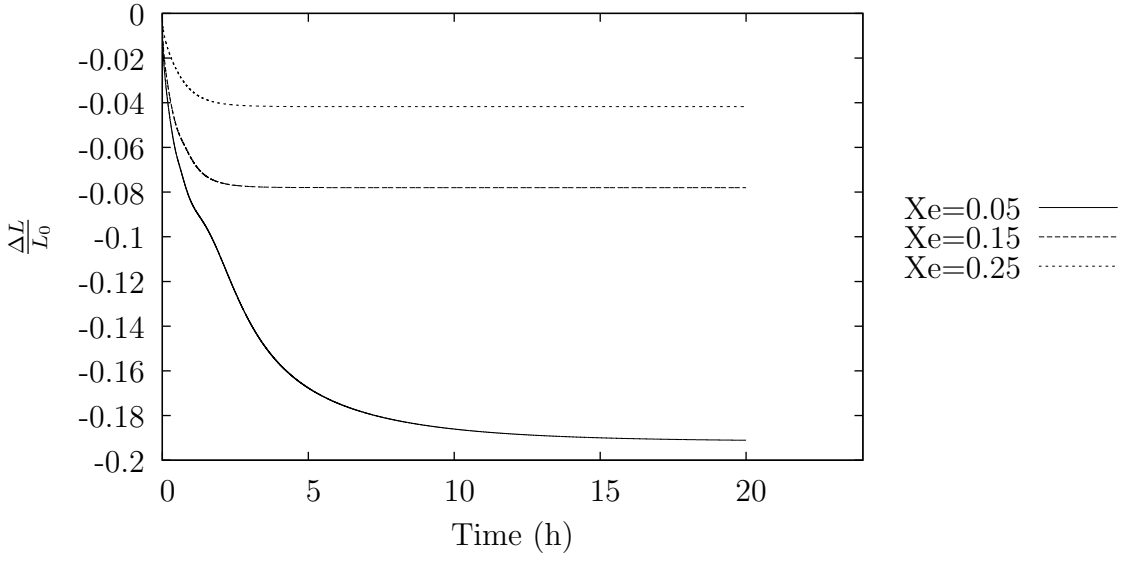

Fig. F.21. Shrinkage vs. Time. T=353 K D_{eff}: Eq. 2.73

F.3 Porosity

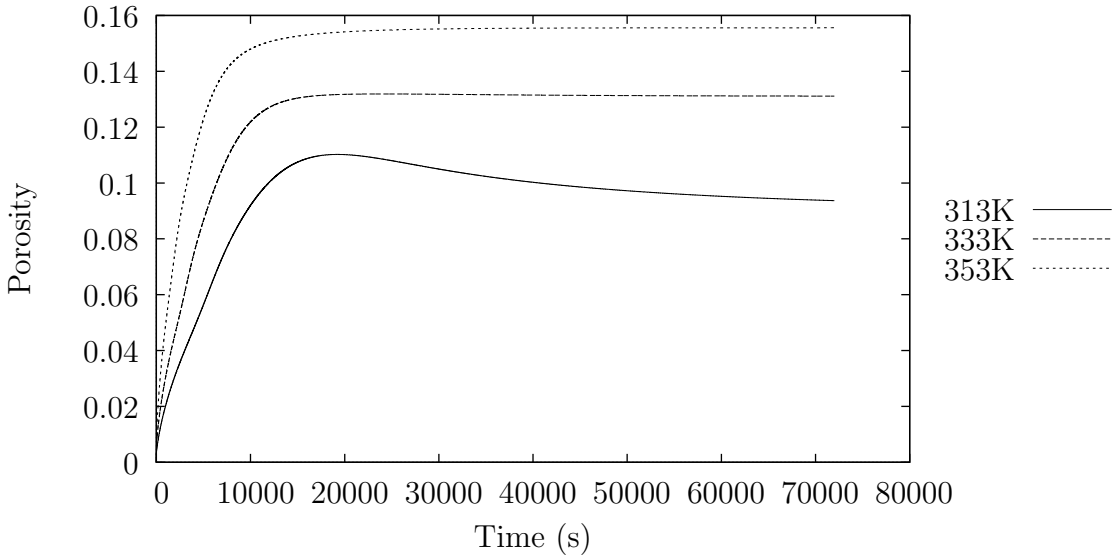

Fig. F.22. Porosity vs. Time at an equilibrium moisture content of $0.10\ \frac{\text{kg}}{\text{kg}_{\text{db}}}$.

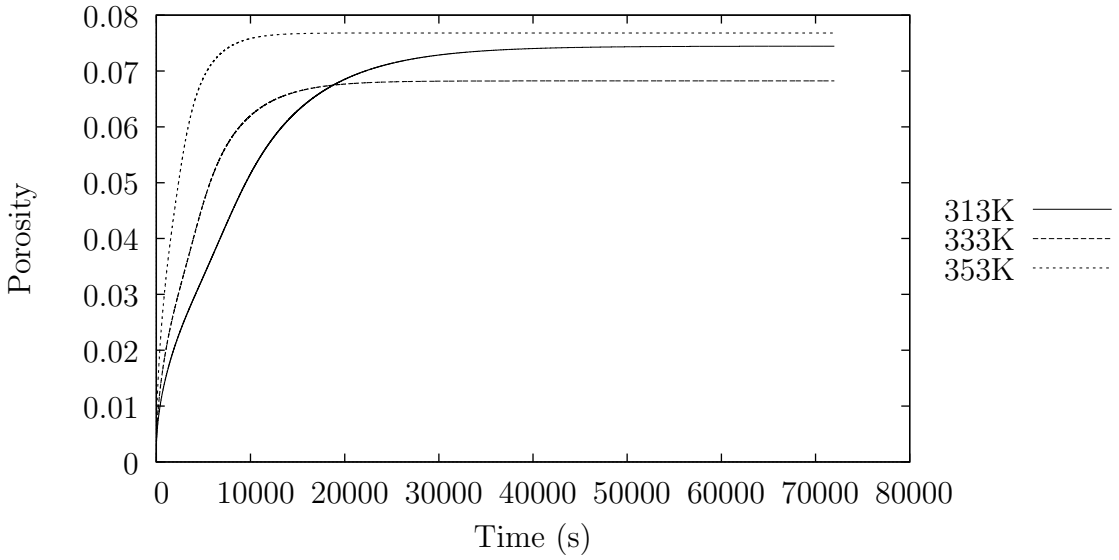

Fig. F.23. Porosity vs. Time at an equilibrium moisture content of $0.20\ \frac{\text{kg}}{\text{kg}_{\text{db}}}$.

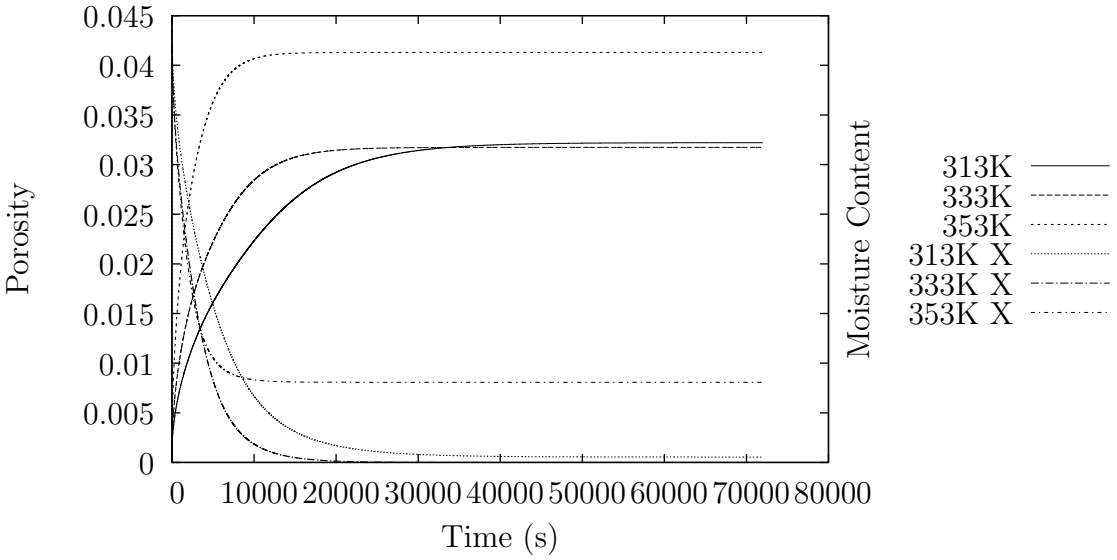

Fig. F.24. Porosity vs. Time at an equilibrium moisture content of 0.25 $\frac{\text{kg}}{\text{kg}_{\text{db}}}$.

G. DERIVATIONS

G.1 Weak Form Derivation

G.1.1 Variable Substitutions

$$c(x,t) = \sum_{i=1}^{N} c_i(t)\phi_i(x) \qquad \text{Concentration} \tag{G.1a}$$

$$\epsilon(x,t) = \sum_{i=1}^{N} \epsilon_i(t)\phi_i(x) \qquad \text{Strain} \tag{G.1b}$$

$$r^{(1)}(x,t) = \sum_{i=1}^{N} r_i^{(1)}(t)\phi_i(x) \qquad \text{Partial strain \#1} \tag{G.1c}$$

$$r^{(2)}(x,t) = \sum_{i=1}^{N} r_i^{(2)}(t)\phi_i(x) \qquad \text{Partial strain \#2} \tag{G.1d}$$

$$u(x,t) = \sum_{i=1}^{N} u_i(t)\phi_i(x) \qquad \text{Displacement} \tag{G.1e}$$

G.1.2 Mass Transfer

Eq. 5.5

$$\frac{\partial c}{\partial t} + \underline{v} \cdot \nabla c = \frac{1}{\rho}\nabla \cdot (\rho D \cdot \nabla c) \tag{G.2}$$

Convert to one-dimensional

$$\frac{\partial c}{\partial t} + v\frac{\partial c}{\partial x} = \frac{1}{\rho}\frac{\partial}{\partial x}\left(\rho D \frac{\partial c}{\partial x}\right) \tag{G.3}$$

Rewrite the velocity in terms of displacement

$$\frac{\partial c}{\partial t} + \frac{\partial u}{\partial t}\frac{\partial c}{\partial x} = \frac{1}{\rho}\frac{\partial}{\partial x}\left(\rho D \frac{\partial c}{\partial x}\right) \tag{G.4}$$

Substitute Eq. G.1

$$\frac{\partial c_i}{\partial t}\phi_i + \frac{\partial u_i}{\partial t}\phi_i c_i \frac{\partial \phi_i}{\partial x} = \frac{1}{\rho}\frac{\partial}{\partial x}\left(\rho D c_i \frac{\partial \phi_i}{\partial x}\right) \tag{G.5}$$

Expand derivative

$$\frac{\partial c_i}{\partial t}\phi_i + \frac{\partial u_i}{\partial t}\phi_i c_i \frac{\partial \phi_i}{\partial x} = \frac{1}{\rho}\frac{\partial \rho}{\partial x} D c_i \frac{\partial \phi_i}{\partial x} + \frac{\partial D}{\partial x} c_i \frac{\partial \phi_i}{\partial x} + D c_i \frac{\partial^2 \phi_i}{\partial x^2} \tag{G.6}$$

Multiply by ϕ_j and integrate to obtain the residual

$$R = \sum_i \int_0^L \left\{ \frac{1}{\rho}\frac{\partial \rho}{\partial x} D c_i \frac{\partial \phi_i}{\partial x} + \frac{\partial D}{\partial x} c_i \frac{\partial \phi_i}{\partial x} + D c_i \frac{\partial^2 \phi_i}{\partial x^2} - \frac{\partial c_i}{\partial t}\phi_i - \frac{\partial u_i}{\partial t}\phi_i c_i \frac{\partial \phi_i}{\partial x} \right\} \phi_j dx \tag{G.7}$$

Integration by parts

$$\begin{aligned} R = \sum_i \int_0^L \Bigg\{ & \frac{1}{\rho}\frac{\partial \rho}{\partial x} D c_i \frac{\partial \phi_i}{\partial x}\phi_j + \frac{\partial D}{\partial x} c_i \frac{\partial \phi_i}{\partial x}\phi_j - D c_i \frac{\partial \phi_i}{\partial x}\frac{\partial \phi_j}{\partial x} - \frac{\partial c_i}{\partial t}\phi_i \phi_j \\ & - \frac{\partial u_i}{\partial t}\phi_i c_i \frac{\partial \phi_i}{\partial x}\phi_j \Bigg\} dx + \left[D c_i \frac{\partial \phi_i}{\partial x}\phi_j \right]_0^L \end{aligned} \tag{G.8}$$

The values of ϕ_i and ϕ_j are equal to 1 on the nodes

$$\begin{aligned} R = \sum_i \int_0^L \Bigg\{ & \frac{1}{\rho}\frac{\partial \rho}{\partial x} D c_i \frac{\partial \phi_i}{\partial x}\phi_j + \frac{\partial D}{\partial x} c_i \frac{\partial \phi_i}{\partial x}\phi_j - D c_i \frac{\partial \phi_i}{\partial x}\frac{\partial \phi_j}{\partial x} - \frac{\partial c_i}{\partial t}\phi_i \phi_j \\ & - \frac{\partial u_i}{\partial t}\phi_i c_i \frac{\partial \phi_i}{\partial x}\phi_j \Bigg\} dx + \left[D \frac{\partial c}{\partial x} \right]_0^L \end{aligned} \tag{G.9}$$

To obtain the equations for use in Eq. 5.28, differentiate Eq. G.9 with respect to each dependent variable.

G.1.3 Viscoelasticity

Eq. 5.14a

$$\epsilon = J_0 \sigma + \sum_{m=1}^{M} J_m r^{(m)} \tag{G.10}$$

Substitute Eq. G.1

$$\epsilon_i \phi_i = J_0 \sigma + \sum_{m=1}^{M} J_m r_i^{(m)} \phi_i \tag{G.11}$$

Multiply by ϕ_j and integrate

$$R = \sum_i \int_0^L \left\{ J_0\sigma - \epsilon_i\phi_i + \sum_{m=1}^{M} J_m r_i^{(m)}\phi_i \right\} \phi_j dx \tag{G.12}$$

Eq. 5.14b

$$\sigma = \frac{\partial}{\partial t} r^{(m)} + \frac{1}{\tau_m} r^{(m)} \tag{G.13}$$

Substitute Eq. G.1

$$\sigma = \frac{\partial r_i^{(m)}}{\partial t}\phi_i + \frac{1}{\tau_m} r_i^{(m)}\phi_i \tag{G.14}$$

Multiply by ϕ_j and integrate

$$R = \sum_i \int_0^L \left\{ \frac{\partial r_i^{(m)}}{\partial t}\phi_i + \frac{1}{\tau_m} r_i^{(m)}\phi_i - \sigma \right\} \phi_j dx \tag{G.15}$$

G.1.4 Displacement

Eq. 5.16

$$\nabla \underline{u} = \underline{\underline{F}} - \underline{\underline{I}} \tag{G.16}$$

One dimensional case (Eq. 5.17)

$$\frac{\partial u}{\partial x} = \epsilon - 1 \tag{G.17}$$

Substitute Eq. G.1

$$u_i \frac{\partial \phi_i}{\partial x} = \epsilon_i\phi_i - 1 \tag{G.18}$$

Multiply by ϕ_j and integrate

$$R = \sum_i \int_0^L \left\{ u_i \frac{\partial \phi_i}{\partial x} - \epsilon_i\phi_i \right\} \phi_j dx \tag{G.19}$$

G.1.5 Isoparametric Mapping

To convert from global coordinates (x) to local, per-element, coordinates (ξ), apply the following substitutions:

$$\phi_i(x) = \phi_i(\xi(x)) \tag{G.20a}$$

$$\frac{d\phi_i}{dx} = \frac{d\phi_i}{d\xi}\frac{d\xi}{dx} \tag{G.20b}$$

$$dx = \frac{dx}{d\xi}d\xi \tag{G.20c}$$

For the case of linear elements, the value of $\frac{dx}{d\xi}$ is given by:

$$\frac{dx}{d\xi} = (x_2 - x_1) = h \tag{G.21}$$

where x_1 and x_2 are the coordinates for the nodes in that element, and h is the element width.

G.1.6 Modifications for Variable Porosity

Eq. G.22 should be added to Eqs. G.1, and substituted in for σ in Eqs. G.12 and G.15. Additionally, Eq. G.23 should be solved alongside the other differential equations. Here, ζ is equal to porosity, and is a function of moisture content, temperature and strain.

$$\sigma = \sum_{i=1}^{N} \sigma_i(t)\phi_i(x) \tag{G.22}$$

$$R = \int_0^L \left\{\zeta P_c - \sigma_i\phi_i\right\}\phi_j dx \tag{G.23}$$

G.2 Porosity

G.2.1 Assumptions

- Solid volume is constant.
- Density of bulk water equals the density of vicinal water. (See Etzler and Fagundus (1987))

- Volumes are additive.
- Pores are initially filled with water.
- Water exists only as a liquid.

G.2.2 Definitions

V_v	Volume of void
V_w	Volume of water
V_{w0}	Initial volume of water
V_s	Solid volume
$\epsilon = \frac{\Delta V}{V_0} = \frac{V - V_0}{V_0}$	Strain
$x_f = \frac{V - V_v}{V}$	Solid fraction
$\phi = \frac{V_v}{V}$	Porosity
$V = V_v + V_w + V_s$	Total volume
$V_0 = V_s + V_{w0}$	Initial volume
$X = \frac{V_{w0}}{V_s}\frac{\rho_s}{\rho_w}$	Moisture content

G.2.3 Porosity

General case

$$\phi = \frac{V_v}{V_v + V_w + V_s} \qquad \text{Porosity definition}$$

$$V_v = -\frac{\phi(V_s + V_w)}{\phi - 1} \qquad \text{Solve for } V_v$$

$$\epsilon = \frac{V_v + V_w + \cancel{V_s} - V_{w0} - \cancel{V_s}}{V_{w0} + V_s} \qquad \text{Strain definition}$$

$$\epsilon = \frac{-\frac{\phi(V_s+V_w)}{\phi-1} + V_w - V_{w0}}{V_{w0} + V_s} \qquad \text{Substitution}$$

$$\phi = \frac{V_{w0}(\epsilon+1) + V_s\epsilon - V_w}{V_{w0}(\epsilon+1) + V_s(\epsilon+1)} \qquad \text{Solve for } \phi$$

$$\phi = \frac{\frac{V_{w0}}{V_s}(\epsilon+1) + \epsilon - \frac{V_w}{V_s}}{\frac{V_{w0}}{V_s}(\epsilon+1) + \epsilon + 1} \qquad \text{Divide by } V_s$$

$$\phi = \frac{X_0\frac{\rho_w}{\rho_s}(\epsilon+1) + \epsilon - X\frac{\rho_w}{\rho_s}}{X_0\frac{\rho_w}{\rho_s}(\epsilon+1) + \epsilon + 1} \qquad \frac{V_{w0}}{V_s} = X_0\frac{\rho_w}{\rho_s}$$

Zero porosity

$$0 = X_0\frac{\rho_w}{\rho_s}(\epsilon+1) + \epsilon - X\frac{\rho_w}{\rho_s}$$

$$0 = X_0\frac{\rho_w}{\rho_s}\epsilon + X_0\frac{\rho_w}{\rho_s} + \epsilon - X\frac{\rho_w}{\rho_s}$$

$$0 = (X_0\frac{\rho_w}{\rho_s} + 1)\epsilon + \frac{\rho_w}{\rho_s}(X_0 - X)$$

$$\epsilon = \frac{\frac{\rho_w}{\rho_s}(X - X_0)}{X_0\frac{\rho_w}{\rho_s} + 1}$$

G.2.4 Solid Fraction

$$
\begin{aligned}
x_f &= \frac{V_s}{V} && \text{Definition of solid fraction} \\
V &= \frac{V_s}{x_f} \\
\epsilon &= \frac{\frac{V_s}{x_f} - V_0}{V_0} && \text{Substitute into strain equation} \\
\epsilon V_0 &= \frac{V_s}{x_f} - V_0 \\
(\epsilon + 1)V_0 &= \frac{V_s}{x_f} \\
(\epsilon + 1)(V_{w0} + V_s) &= \frac{V_s}{x_f} && V_0 = V_{w0} + V_s \\
(\epsilon + 1)\left(\frac{V_{w0}}{V_s} + 1\right) &= \frac{1}{x_f} && \text{Divide by } V_s \\
(\epsilon + 1)\left(X_0\frac{\rho_w}{\rho_s} + 1\right) &= \frac{1}{x_f} && \frac{V_{w0}}{V_s} = X_0\frac{\rho_w}{\rho_s} \\
x_f &= \frac{1}{(\epsilon + 1)\left(X_0\frac{\rho_w}{\rho_s} + 1\right)}
\end{aligned}
$$

G.3 Diffusivity

G.3.1 Assumptions

- No temperature gradient
- Gas phase is a saturated vapor
- Water concentration in the vapor phase is negligible
- Ideal gas

G.3.2 Gas-phase Concentration

$$
\begin{aligned}
PV &= nRT && \text{Ideal gas law} \\
PV &= \frac{m}{M}RT \\
c_V = \frac{m}{V} &= \frac{PM}{RT} \\
c_V &= \frac{a_w p_{vap} M}{RT} && P = a_w p_{vap} \\
X_{db,V} &= \frac{a_w p_{vap} M}{RT\rho_s}
\end{aligned}
$$

G.3.3 Effective Diffusivity

$$
\begin{aligned}
&\frac{\partial c}{\partial t} = \nabla \cdot j \\
&j = D\nabla c && \text{Total mass flux} \\
&j = j_L + j_V \\
&j = \frac{A_L}{A_T} D_L \nabla X_L + \frac{A_V}{A_T} D_V \nabla X_V \\
&\text{Let } \frac{A_L}{A_T} = (1-\phi) \\
&\frac{A_V}{A_T} = \phi \\
&j = (1-\phi) D_L \nabla X_L + \phi D_V \nabla X_V \\
&j = (1-\phi) D_L \nabla X_L + \phi D_V \nabla \left(\frac{a_w p_{vap} M}{RT\rho_s} \right) && \text{Substitution} \\
&j = (1-\phi) D_L \nabla X_L + \phi D_V \frac{p_{vap} M}{RT\rho_s} \nabla a_w && \text{Only } a_w \text{ depends on } X_L \\
&j = (1-\phi) D_L \nabla X_L + \phi D_V \frac{p_{vap} M}{RT\rho_s} \frac{\partial a_w}{\partial X_L} \nabla X_L && \text{Chain rule} \\
&j = \left\{ (1-\phi) D_L + \phi D_V \frac{p_{vap} M}{RT\rho_s} \frac{\partial a_w}{\partial X_L} \right\} \nabla X_L \\
&D = (1-\phi) D_L + \phi D_V \frac{p_{vap} M}{RT\rho_s} \frac{\partial a_w}{\partial X_L} && \text{By comparison}
\end{aligned}
$$

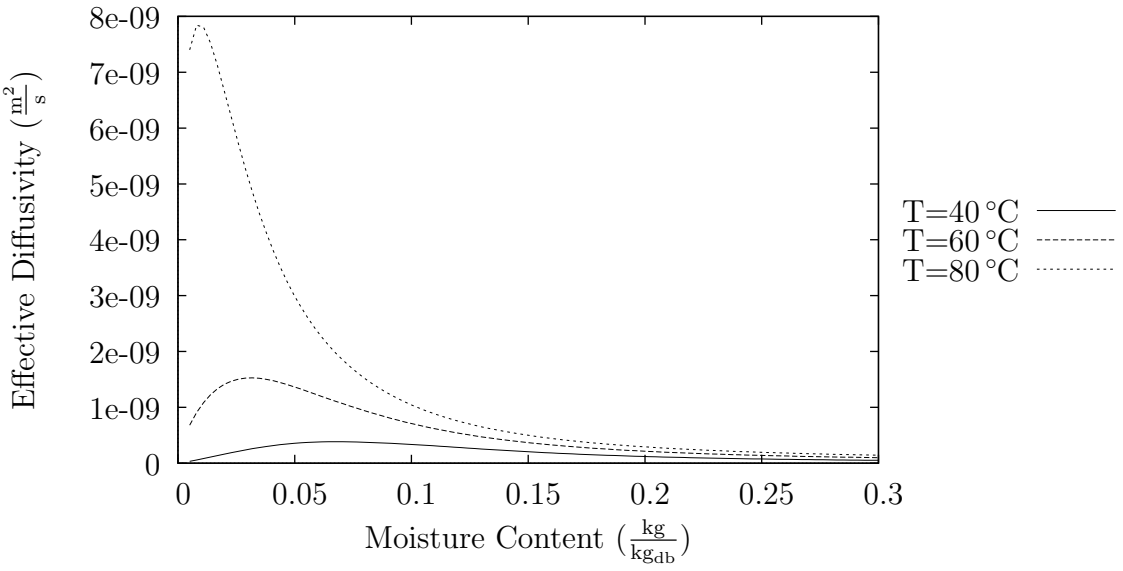

Fig. G.1. Effective diffusivity

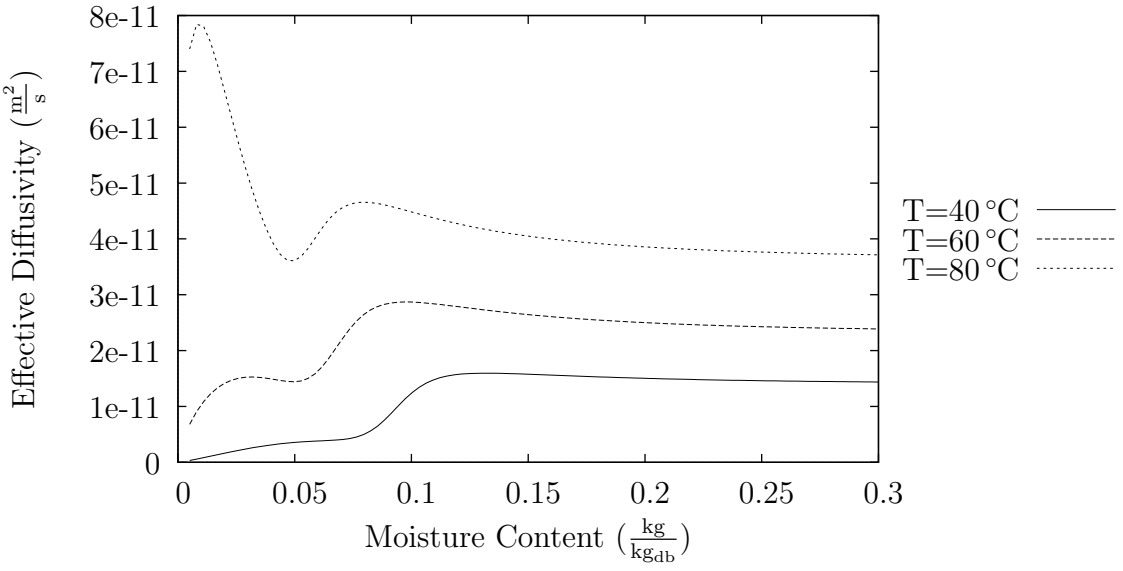

Fig. G.2. Effective diffusivity where vapor diffusivity is divided by a factor of 100.

H. ADDITIONAL LITERATURE DATA

Table H.1.: Data for volumetric and radial shrinkage from Cummings (1981)

Moisture Content		Temperature	Volume			
			Initial	Final	V/V0	Diameter
$(w.b.)$	$(d.b.)$	(°C)	(cm^3)	(cm^3)		
0.1303	0.1498	50	63.6553	51.8342	0.8143	0.1165
0.1392	0.1617	50	63.3864	52.8003	0.8330	0.1160
0.1711	0.2064	50	61.9500	54.2025	0.8749	0.1188
0.2027	0.2542	50	61.2638	58.0883	0.9482	0.1266
0.1315	0.1514	50	61.9974	50.6050	0.8162	0.1160
0.1405	0.1635	50	63.9427	53.4218	0.8355	0.1178
0.1600	0.1905	50	62.7558	53.9598	0.8598	0.1186
0.1860	0.2285	50	72.7095	67.5253	0.9287	0.1216
0.1290	0.1481	50	63.9951	51.3737	0.8028	0.1140
0.1345	0.1554	50	56.2245	47.0258	0.8364	0.1160
0.1530	0.1806	50	65.1051	56.7729	0.8720	0.1180
0.1900	0.2346	50	57.8561	53.5690	0.9259	0.1190
0.1378	0.1598	42	64.4120	52.0180	0.8076	0.1130
0.1460	0.1710	42	63.0101	51.9855	0.8250	0.1160
0.1645	0.1969	42	63.2613	55.2381	0.8732	0.1170
0.2170	0.2771	42	58.8149	55.7561	0.9480	0.1200
0.1340	0.1547	42	67.2870	55.4601	0.8242	0.1160
0.1420	0.1655	42	64.0593	55.0120	0.8588	0.1170
0.1570	0.1862	42	65.2239	59.6107	0.9139	0.1190

Moisture Content		Temperature	Volume		V/V0	Diameter
			Initial	Final		
0.2015	0.2523	42	64.6994	61.0098	0.9430	0.1210
0.1390	0.1614	42	65.6988	55.1834	0.8399	0.1160
0.1520	0.1792	42	67.3100	58.0157	0.8619	0.1170
0.1650	0.1976	42	65.1220	*	*	*
0.2650	0.3605	42	67.3525	*	*	*
0.1260	0.1442	58	60.6957	50.6909	0.8352	0.1180
0.1350	0.1561	58	57.3205	49.0314	0.8554	0.1180
0.1540	0.1820	58	57.5938	50.8048	0.8821	0.1210
0.1820	0.2225	58	57.7995	52.6930	0.9117	0.1220
0.1230	0.1403	58	66.9789	53.7257	0.8021	0.1170
0.1340	0.1547	58	66.8833	54.3883	0.8132	0.1180
0.1650	0.1976	58	64.7600	57.5645	0.8889	0.1190
0.1895	0.2338	58	67.1509	58.1129	0.8654	0.1220
0.1230	0.1403	58	59.5000	47.6298	0.8005	0.1170
0.1230	0.1403	58	62.3070	51.2970	0.8233	0.1180
0.1570	0.1862	58	58.1150	51.1120	0.8795	0.1200
0.1870	0.2300	58	58.4030	51.5172	0.8821	0.1220

* Not available due to mold growth.

Table H.2.
Puffed pasta diffusivity from Xiong (1989)

X_{db}	44 °C	55 °C	71 °C	105 °C
0.03				1.035×10^{-10}
0.04				1.284×10^{-10}
0.05		1.493×10^{-11}	4.59×10^{-11}	1.314×10^{-10}
0.06		2.75×10^{-11}	6.07×10^{-11}	1.404×10^{-10}
0.07	1.87×10^{-11}	3.83×10^{-11}	7.49×10^{-11}	1.592×10^{-10}
0.08	2.43×10^{-11}	5.11×10^{-11}	9.31×10^{-11}	1.804×10^{-10}
0.09	3.02×10^{-11}	6.86×10^{-11}	1.064×10^{-10}	
0.1	3.36×10^{-11}	8.11×10^{-11}	1.186×10^{-10}	
0.11	4.01×10^{-11}			
0.21	4.44×10^{-11}	8.88×10^{-11}	1.08×10^{-10}	1.898×10^{-10}

Table H.3.
Regular pasta diffusivity from Xiong (1989)

X_{db}	44 °C	55 °C	71 °C	105 °C
0.03				5.270×10^{-11}
0.04				5.600×10^{-11}
0.05			2.070×10^{-11}	
0.06			2.130×10^{-11}	7.090×10^{-11}
0.07			2.400×10^{-11}	7.940×10^{-11}
0.08		1.830×10^{-11}	2.670×10^{-11}	7.920×10^{-11}
0.09	7.350×10^{-12}	1.950×10^{-11}	2.920×10^{-11}	
0.1	8.400×10^{-12}	2.102×10^{-11}	3.120×10^{-11}	
0.11	9.220×10^{-12}	2.301×10^{-11}	3.410×10^{-11}	
0.12	1.045×10^{-11}	2.490×10^{-11}		
0.13	1.180×10^{-11}	2.612×10^{-11}		
0.14	1.320×10^{-11}			
0.15	1.460×10^{-11}			
0.21	1.660×10^{-11}	2.680×10^{-11}	3.580×10^{-11}	8.280×10^{-11}

Table H.4.
Diffusivity data from Litchfield

X_{db}	40 °C	55 °C	70 °C	85 °C
0.015				1.600×10^{-12}
0.021				2.850×10^{-12}
0.027				3.600×10^{-12}
0.037				3.960×10^{-12}
0.048				6.200×10^{-12}
0.052			3.500×10^{-12}	
0.057		1.610×10^{-12}		
0.058		1.660×10^{-12}		
0.06	1.550×10^{-12}			
0.066				6.260×10^{-12}
0.067		1.840×10^{-12}		
0.075				7.020×10^{-12}
0.079		2.070×10^{-12}		
0.088		2.330×10^{-12}		
0.089	4.280×10^{-12}			
0.095		2.600×10^{-12}		
0.105		8.750×10^{-12}		
0.108	5.830×10^{-12}			
0.12		1.850×10^{-11}		
0.125	9.380×10^{-12}			
0.238				4.840×10^{-11}
0.239			3.500×10^{-11}	
0.254		2.330×10^{-11}		
0.256	1.470×10^{-11}			

Table H.5.
Measured isotherm data from Bressani (2014)

Temperature	X_m	C_g	K
25 °C	0.0778	89.0833	0.8004
30 °C	0.083	35.5	0.727
35 °C	0.0629	38.4293	0.8716
40 °C	0.0663	30.8955	0.8202
50 °C	0.0527	30.1942	0.8631
60 °C	0.0519	8.0021	0.8694
70 °C	0.0609	4.0905	0.7294
75 °C	0.027	14.4761	0.91
80 °C	0.0334	12.4133	0.9575
85 °C	0.0467	13.012	0.5831
90 °C	0.0242	6.7393	0.9917

Table H.6.
Measured isotherm data from Erbas et al. (2005)

Temperature	X_m	C_g	K
20 °C	0.118	4.21	0.65
35 °C	0.0645	8.77	0.71
50 °C	0.0592	10.01	0.72
60 °C	0.0353	200.1	0.76

Table H.7.
Measured isotherm data from Andrieu et al. (1985). Data printed in Bressani (2014)

Temperature	X_m	C_g	K
40 °C	0.0636	35.5	0.858
50 °C	0.06	17.8	0.871
60 °C	0.0531	8.33	0.897
70 °C	0.0465	6.04	0.915

Table H.8.
Isotherm data from Xiong (1989)

Moisture % (dry basis)	35 °C	45 °C	50 °C
22.190	0.825	0.835	0.847
14.618	0.663	0.701	0.727
10.756	0.496	0.565	0.609
8.715	0.361	0.429	0.464
6.135	0.140	0.260	0.315